UNIVERSITY OF CALIFORNIA, SAN DIEGO
SAN DIEGO STATE UNIVERSITY

Loading Mode Optimization and Structure Tailoring in Spark Plasma Sintering of Monocarbide Powder-based Components for High Temperature Applications

A dissertation submitted in partial satisfaction of the
requirements for the degree Doctor of Philosophy

in

Engineering Sciences (Mechanical and Aerospace Engineering)

by

Xialu Wei

Committee in charge:

University of California, San Diego

Professor Marc A. Meyers, Co-Chair
Professor J. Enrique. Luco
Professor Vitali F. Nesterenko

San Diego State University

Professor Eugene A. Olevsky, Co-Chair
Professor Kaveh Akbari Hamed

2016

The Dissertation of Xialu Wei is approved, and it is acceptable in quality and form for publication on microfilm and electronically:

_____

_____

_____

_____
Co-Chair

_____
Co-Chair

University of California, San Diego

San Diego State University

2016

DEDICATION

Dedicated to My Grandmother

TABLE OF CONTENTS

LIST OF FIGURES

LIST OF TABLES

ACKNOWLEDGEMENTS

I would like to acknowledge Professors Eugene A. Olevsky and Marc A. Meyers for their invaluable guidance throughout my Ph.D studies. I would also like to acknowledge my committee members Professors Vitali F. Nesterenko, J. Enrique. Luco and Kaveh Akbari Hamed, as well as all colleagues in the Powder Technology Laboratory without whose suggestions and assistances I would not have been able to complete my research work on time.

Chapter 2, in full, is a reprint of the material as it appears in "X. Wei, C. Back, O. Izhvanov, O. L. Khasanov, C. D. Haines and E. A. Olevsky, Spark plasma sintering of commercial zirconium carbide powders: densification behavior and mechanical properties, *Materials*, 8, 2015", and in "X. Wei, C. Back, O. Izhvanov, C. D. Haines and E. A. Olevsky, Zirconium carbide produced by spark plasma sintering and hot pressing: densification kinetics, grain growth, and thermal properties, *Materials*, 9, 2016". The dissertation author was the primary investigator and author of these papers.

Chapter 3, in part, is a reprint of the material as it appears in "X. Wei, D. Giuntini, A. L. Maximenko, C. D. Haines and E. A. Olevsky, Experimental investigation of electric contact resistance in spark plasma sintering tooling setup, *J. Am. Ceram. Soc.*, 98, 2015", and may appear in "X. Wei, A. L. Maximenko, C. Back, O. Izhvanov, E. A. Olevsky, Effects of loading modes on densification efficiency of spark plasma sintering: sample study of ZrC consolidation, *Phil. Mag. Lett.*, 2016". The dissertation author was the primary investigator and author of these papers.

VITA

2005 Bachelor of Engineering, Wuhan University of Technology, China

2010 Master of Science, Southeastern Louisiana University

2016 Doctor of Philosophy, University of California, San Diego and San Diego State University

PUBLICATIONS

1. X. Wei, C. Back, O. Izhvanov, C. D. Haines, E. A. Olevsky. Zirconium carbide produced by spark plasma sintering and hot pressing: Densification kinetics, grain growth, and thermal properties. *Materials*. 2016; 9:577.
2. X. Wei, C. Back, O. Izhvanov, O. Khasanov, C. D. Haines and E. A. Olevsky. Spark plasma sintering of commercial zirconium carbide powder: Densification behaviors and mechanical properties. *Materials*. 2015; 8:6043-6061.
3. X. Wei, D. Giuntini, A. L. Maximenko, C. D. Haines, and E. A. Olevsky. Experimental investigation of electric contact resistance in spark plasma sintering tooling setup. *Journal of the American Ceramic Society*. 2015; 98:3553-3560.
4. G. Cui, X. Wei, E. A. Olevsky, R. M. German, J. Chen. The manufacturing of high porosity iron with an ultra-fine microstructure via free pressureless spark plasma sintering. *Materials*. 2016; 9: 495.

5. G. Cui, X. Wei, E. A. Olevsky, R. M. German, J. Chen. Preparation of high performance bulk Fe-N alloy by spark plasma sintering. *Materials & Design*. 2016; 90:115-121.

6. D. Giuntini, X. Wei, A. L. Maximenko, W. Li, A. M. Ilyina, and E. A. Olevsky. Initial stage of free pressureless spark-plasma sintering of vanadium carbide: Determination of surface diffusion parameters. *International Journal of Refractory Metals and Hard Materials*. 2013; 41:501-506.

7. W. Chai, R. M. German, E. A. Olevsky, X. Wei, R. Jiang, and G. Cui. Preparation and properties of high strength Fe-Ni-P ternary alloys. *Advanced Engineering Materials*. 2016; 18: 1889-1896.

8. X. Wei, A. L. Maximenko, C. Back, O. Izhvanov, E. A. Olevsky. Effects of loading modes on densification efficiency of spark plasma sintering: sample study of ZrC consolidation. *Philosophical Magazine Letters.* 2016, submitted.

9. Y. Shan, X. Wei, X. Sun, J. Xu, Q. Qin, E. A. Olevsky. Highly infrared transparent spark plasma sintered AlON ceramics. *Journal of Materials Research*. 2016, submitted.

FIELD OF STUDY

Major Field: Engineering Sciences (Mechanical and Aerospace Engineering)

Studies in Powder Material Processing

Professors Eugene A. Olevsky and Marc A. Meyers

ABSTRACT OF THE DISSERTATION

Loading Mode Optimization and Structure Tailoring in Spark Plasma Sintering of Monocarbide Powder-based Components for High Temperature Applications

by

Xialu Wei

Doctor of Philosophy in Engineering Sciences
(Mechanical and Aerospace Engineering)

University of California, San Diego, 2016
San Diego State University, 2016

Professor Eugene A. Olevsky, Co-Chair
Professor Marc A. Meyers, Co-Chair

In this study, the spark plasma sintering (SPS) is employed to consolidate poorly sinter-able ultra-high temperature ceramic (UHTC) powders due to the fact that the conjoint application of electric current and mechanical pressure during SPS can largely offset the required processing temperature. Zirconium carbide (ZrC) is selected as target material as it broadly represents properties of typical UHTCs. Investigations on SPS of ZrC are concurrently conducted in two correlated regimes: One regime is

used to optimize the SPS densification efficiency by manipulating the loading schematics. The other regime is used to produce complex shape carbide components for high temperature applications via SPS. Both theoretical and experimental studies are involved in the achievement of the formulated research objectives.

Consolidation of ZrC has been carried out to form a densification map with determining the optimal processing parameters. The densification of ZrC is studied through the continuum theory of sintering, in which the ZrC power-law creep parameters have been determined through the clarification of electrical and thermal aspects of the employed SPS system. Then the SPS-forging setup is proposed as it is theoretically and experimentally proven to be able to render more densification than the regular SPS. SPS-forging and regular SPS are eventually integrated into a hybrid loading mode SPS regime to combine the advantages of the individual setups to obtain the optimal densification kinetics.

Annular shape ZrC pellets have been fabricated using SPS. Finite element modeling framework is constructed to manifest the thermomechanical interactions during the SPS of annular shape ZrC specimens. The fabrication procedures are practically adapted to produce also annular shape carbide composites with excellent high temperature structural strength being used as alternative SPS tooling components. The applicability of annular shape fuel pellet to accommodate volume swelling under its service conditions is investigated. The irradiation-induced swelling phenomena are analyzed by analytical modeling and finite element simulations, in which the generated fission products are considered to be the sources of the fuel pellet swelling.

CHAPTER 1 INTRODUCTION

Although the practical utilization of sintering techniques dates back to thousands of years ago when humans produced bricks and porcelains, the scientific study of sintering processes started to emerge in the first half of the last century. Since the 1940s, the existence of surface tension has been considered as the driving force which renders the coalescence of particles in order to lower the overall surface energy of a system. It explained why free sintering occurs spontaneously as time goes by, for example as it happens with snow piles and mineral deposits. Based on this idea, the mechanisms of sintering at the microscopic level, e.g. the formation and growth of local contacts between particles, have been clarified to a large degree in early publications [1-5]. Obtained results embedded the kinetic aspects of free sintering, including surface diffusion, neck growth, structure morphologies and so on.

At the macroscopic level, as a densification process, sintering is always accompanied by volume shrinkage and substance strengthening. Microscopic level investigations were not sufficient to cover some inherent phenomena such as shape deformation, density variation and stress-strain evolution, during the densification of a porous body, especially when an external force is applied. To elaborate these problems, physicists and material scientists have put efforts into forming a scientific direction utilizing continuum mechanics in sintering studies through the second half of the last century [6-10]. From these ideas, sintering was described as an activated adhesion process under both thermal and mechanical effects based on the non-linear viscous deformation of porous bodies. Research developments not only emphasized the

properties of the particles themselves, like particle size, viscosity and surface tension but also paid attention to the environmental conditions in which these particles are processed, for example, furnace temperature, applied pressure and tooling configurations. Since then, power-law creep (PLC) has been considered to be the dominant mechanism to control the mass transport in pressure-assisted powder consolidation process. The shrinkage and strengthening of a porous body during high temperature deformation has been recognized as a result of concurrent processes of creep and densification [11-15].

The developments of sintering theories [16-18] triggered the interests in improving sintering efficiency. The temperature was recognized as a key factor. Effective sintering usually requires high processing temperature to be employed (e.g. 70% - 80% of the specimen's melting temperature). However, increasing processing temperature accelerates the grain growth in the specimen and large grains to some extent compromise the strength of the sintered product [19]. To lower the processing temperature and to keep the grains from growing too much, applications of compressive stresses have been widely accepted as an important mechanical method to effectively compensate the temperature requirements on the densification of a specimen. Under the applied stresses, sintering- as well as pressing-driven phenomena are occurring simultaneously within a porous media to jointly facilitate its densification kinetics. During such a mechanical treatment, a porous body is not only experiencing volume shrinkages but also undergoing shape distortions. This idea has inspired further interests in correlating the deformation with the densification during

the consolidation of porous materials to elucidate the influences of loading modes on densification kinetics [20, 21].

The loading mode – based investigation of consolidation process is especially attractive for spark plasma sintering (SPS). Indeed, one of the broadly claimed advantages of SPS is its capability of grain size retention due to the overall lower temperature level and shorter time of processing. The extremely applied stress schematics appears to be a natural tool for enhancing the densification efficiency by offsetting the impact of lower material deformability caused by lower temperatures of the processing. Below, we analyze the powder consolidation studies in which various modes of loading of powder materials have been utilized.

1.1 Loading Modes in Powder Consolidation Techniques: Literature Survey

1.1.1 Comparison of the effectiveness of different loading modes

When a porous body is subjected to mechanical stresses in a deformation process, its rate of volume change,$\dot{e}$, and its rate of shape change, $\dot{\gamma}$, can be expressed in the cylindrical coordinates, as [22],

$$\dot{e} = \dot{\varepsilon}_r + \dot{\varepsilon}_\theta + \dot{\varepsilon}_z \tag{1.1}$$

$$\dot{\gamma} = \sqrt{\frac{1}{3}\left[(\dot{\varepsilon}_r - \dot{\varepsilon}_\theta)^2 + (\dot{\varepsilon}_\theta - \dot{\varepsilon}_z)^2 + (\dot{\varepsilon}_z - \dot{\varepsilon}_r)^2 + 6(\dot{\varepsilon}_{r\theta}^2 + \dot{\varepsilon}_{\theta z}^2 + \dot{\varepsilon}_{rz}^2)\right]} \tag{1.2}$$

where $\dot{\varepsilon}_r, \dot{\varepsilon}_\theta$ and $\dot{\varepsilon}_z$ are strain rates along radial, tangential and axial directions, respectively. $\dot{\varepsilon}_{r\theta}$, $\dot{\varepsilon}_{\theta z}$ and $\dot{\varepsilon}_{rz}$ are strain rate components in shear directions. In this study, the ratio of the volume change rate, $\dot{e}$, to the shape change rate, $\dot{\gamma}$, in analogy to the stiffness of a fully dense article, is used to identify the deformation resistance of a porous body in response to the modes of loading. The shrinkage of a specimen during its consolidation process results in a negative volume change rate but the shape change rate is always positive (see Equation (1.2)), therefore the ratio between these two remains negative. The lower the ratio is, the more the specimen deforms.

The magnitude of this analogous “stiffness” is directly related to the level of applied stress and the selection of boundary conditions. For consolidation at low stress level, as the applied stress (usually less than 1 MPa) is comparable to the sintering stress introduced by the surface tension, the term "sintering" is used. At high stress level, since the sintering-imposed stress is nearly negligible compared to the applied stress, the process is termed "pressing" instead of "sintering". Taking into account the boundary conditions, free up-setting (pressing without lateral confinement), pressing in a rigid die (pressing with lateral confinement) and isostatic pressing (pressing with confinements in all directions) are the three most common loading modes that have been discussed in the literature [20, 21, 23].

1.1.1.1 Free up-setting loading mode

During free up-setting, as shown in Figure 1.1 a, the powder object does not enter into the cavity of a die, so there are no constraints along the lateral surface of the

object. When compressive stress is applied to the top platform, under ideal conditions (no friction at the contact surfaces), a reduction in porous body's height is accompanied by an unconstrained increase in its cross-section (see Figure 1.1 b).

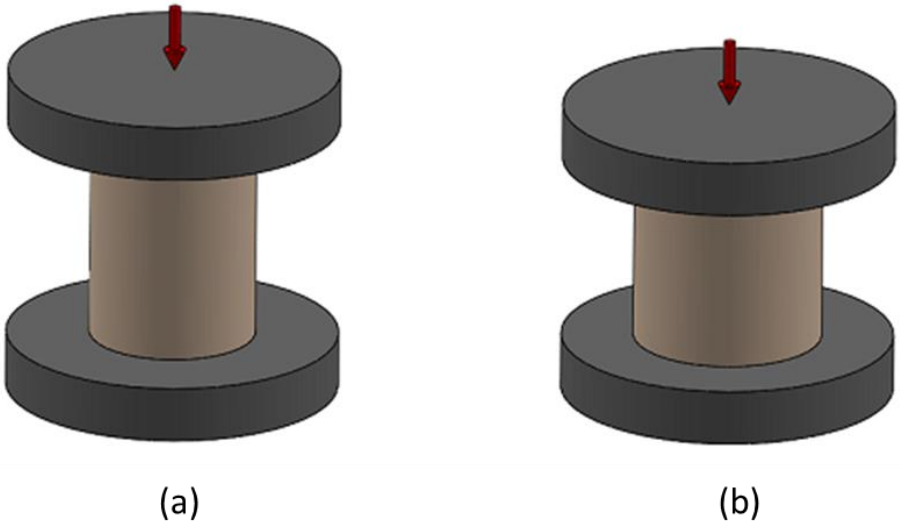

Figure 1.1 Deformation schematics of free up-setting loading mode without contact friction: (a) Before deformation; (b) After deformation.

If a cylindrical shape specimen has an axisymmetric geometry regarding the *z*-axis, its radial and tangential strain rates are equal ($\dot{\varepsilon}_r = \dot{\varepsilon}_\theta$). Additionally, there is no shear component because of the friction-free assumption. The "stiffness" of a porous body subjected to this idealized free up-setting setup can be expressed by using the principles of continuum mechanics,

$$\frac{\dot{e}}{\dot{\gamma}} = \frac{\dot{\varepsilon}_z + 2\dot{\varepsilon}_r}{\sqrt{\frac{2}{3}}|\dot{\varepsilon}_z - \dot{\varepsilon}_r|} \tag{1.3}$$

However, one needs to realize that the contact friction always exists in real-world applications and it causes the formation of shear components at the contact interface. In the case of an axisymmetric geometry, even though the shear terms $\dot{\varepsilon}_{r\theta}$ and $\dot{\varepsilon}_{\theta z}$ can cancel each other due to the geometrical properties, another shear term, $\dot{\varepsilon}_{rz}$, has to be taken into account. By adding this shear component to the denominator of Equation (1.3), we have Equation (1.4) to represent the "stiffness" of a porous body experiencing shape distortion under free up-setting. The deformation schematics are illustrated in Figure 1.2 and shape barreling is observed after deformation.

$$\frac{\dot{e}}{\dot{\gamma}} = \frac{\dot{\varepsilon}_z + 2\dot{\varepsilon}_r}{\sqrt{\frac{2}{3}[(\dot{\varepsilon}_z - \dot{\varepsilon}_r)^2 + 3\dot{\varepsilon}_{rz}^2]}} \tag{1.4}$$

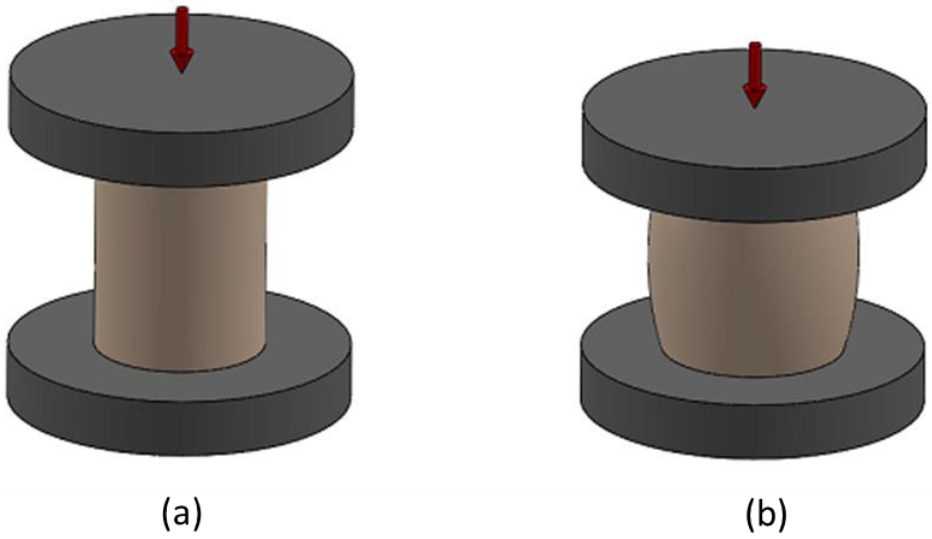

Figure 1.2 Deformation schematics of free up-setting loading mode under contact friction: (a) Before deformation; (b) After deformation.

The investigations on free up-setting of powdered compacts have been widely carried out under different versions of processing conditions. For example hot forging

[24-31], sintering forging [7, 32-35] and cold forging, all without imposing constraints along the lateral surface of the specimen [36, 37].

Density distribution in a porous compact during free up-setting was first studied by Dorofeev in 1975 [24]. Two characteristic zones were distinguished by the author to describe the non-uniform density induced by the frictional forces in the treated specimen: a central zone with high density and a peripheral zone with substantially lower density adjacent to the lateral surface. The author restated the density variations due to boundary constrictions in forming stepped shape powder compact using hot forging with free up-setting in another study [25]. A powder compact was inserted into a stepped die with an initial clearance to the die walls. The specimen was first subjected to a free up-setting and then deformed to a stepped shape final product after all clearances were filled out. This kind of setup can be recognized as an early attempt to produce net-shaped products through free up-setting technique.

Baglyuk considered the basic relationships of the macroscopic shape change during hot up-setting of the cylindrical specimens with different densities [26]. Axial and transverse deformations were correlated with the coefficient of barrel shape in this study. The author also analytically solved the shape change problem by considering the rigid-plastic behavior of a deformed porous medium in a later study [27]. The coefficient of contact friction was taken into account and was proven to be able to facilitate the densification at a given axial strain rate.

The densification of porous alloyed steel under hot forging was studied by Cho *et al*. [28]. Various initial densities, strain rates and temperatures were taken into

consideration, with the purpose of comparing to several yield functions from the literature. A new yield function was finally proposed to better predict the specimen's plastic response and densification behavior. A similar investigation was conducted by Han *et al.* [29] to analyze the elastoplastic problems in hot forging of porous metal using the finite element method. Dependences of the thermal and thermoelastic properties of porous metals on their relative densities were used in finite element calculations. Obtained results showed good agreement with experimental data. Other performed studies on hot forging, for example, Refs. [30] and [31] also looked at characterizing the deformation phenomena but more focused on specific materials.

Sinter forging is a specially designed technique with relatively low external load (comparable to the sintering stress) in order to observe the influences of sintering shrinkage and creep deformation. It was first practiced by De Jonghe and Rahaman [32] using the so-called loading dilatometer to examine how creep and densification affect one another when they occur at the same time. Then CdO powder compacts were subjected to stresses between 0 and 0.25 MPa to study the sintering behavior [7, 33]. The dependence of creep rate on the effective stress was determined. The sintering stress variation was correlated with densification rate and grain size to verify the grain boundary diffusion rate-controlling mechanism in sintering of CdO powders. Lately, Venkatachari and Raj [34] measured both axial and radial strains in sinter forging of cylindrical specimens. These experiments have provided a direct measurement of the intrinsic sintering pressure which was found to lie in the range of 0.4 to 0.8 MPa. It was also found that the processing defects can be virtually

eliminated by the shear strains during sinter forging and lead to an increase in the strength of the processed specimens [35].

Cold forging is usually performed around room temperature on fully and partially dense bodies to analyze their plastic behaviors and formability under stresses. Similar to hot forging, shape change, strain-stress relations and density variations were the most discussed topics in the past. Narayanasamy and Pandey [36] investigated the densification features in upset-forging of porous aluminum–alumina composites. The deformed density, strains, stresses and the radius of curvature of the barrel during the upsetting of powder compact were determined analytically. Shrizly *et al.*[37] estimated the effects of hydrostatic stresses on the material density evolutions in an open die forging model.

1.1.1.2 Pressing in a rigid die loading mode

Schematics of pressing in a rigid die process are illustrated in Figure 1.3 a. A powder-based sample is inserted into a die with its lateral surface being constrained by the die wall. This setup allows the specimen shrinking along the loading axis but prevents it from displacing in the direction perpendicular to the loading axis. Therefore, only a reduction in the specimen's height is observed after compaction (see Figure 1.3 b).

During pressing in a rigid die process, the sample's radial strain rate, $\dot{\varepsilon}_r$, is equal to zero as the it is constrained by the die wall along the radial direction. Hence the analogous "stiffness" of a porous body subjected to pressing in a rigid die setup,

also by assuming an axisymmetric continuum geometry in cylindrical coordinate system, gives a fixed ratio of one to another, according to,

$$\frac{\dot{e}}{\dot{\gamma}} = \frac{\dot{\varepsilon}_z}{\sqrt{\frac{2}{3}}|\dot{\varepsilon}_z|} = -\frac{\sqrt{6}}{2} \tag{1.5}$$

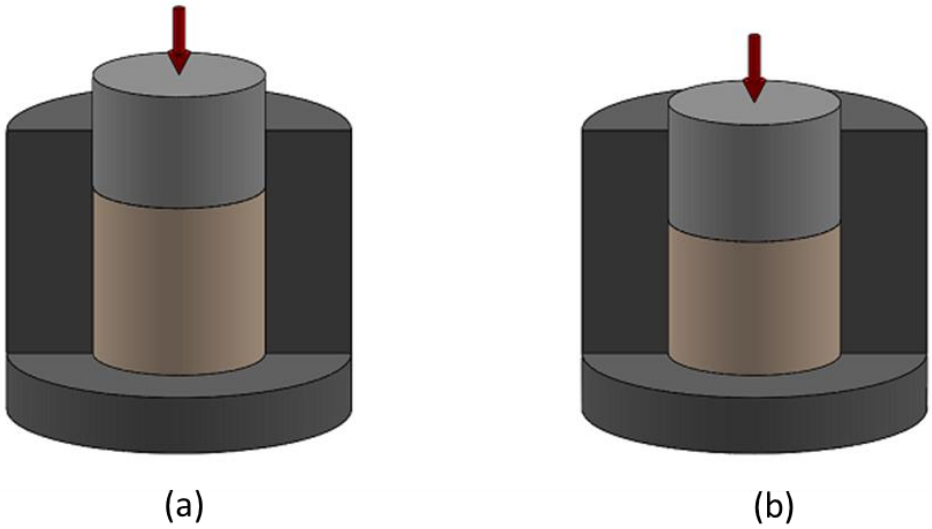

Figure 1.3 Deformation schematics of pressing in a rigid die loading mode: (a) Before deformation; (b) After deformation.

Pressing in a rigid die setup has been widely applied in powder metallurgy processes to produce the near net shape components. Cold die compaction, also known as uniaxial pressing, is a common powder pre-compaction technique to prepare green compacts for subsequent sintering processes. It is usually operated at low temperatures with high mechanical pressure being applied to the powders in a metal or ceramic die. During such a treatment, loose powders are compacted together and a large quantity of inter-particle holes are eliminated, which, in turn, results in a relatively high packing

density. The compaction process is quite important as the green density of the pressed sample influences the densification of the sample during the sintering process.

The volume change of ceramic powder beds in rigid die pressing process has attracted lots of research interest. Cooper and Eaton [38] examined four different ceramic powders with completely different hardness and derived to an expression for the fractional volume compaction at a given axial pressure, whose coefficients were determined by fitting the experimental data. This expression was adequate to describe the behavior of all investigated powders. Kawakita and Ludde [39] summarized their co-workers' work and promoted an equation to show the relation between the relative volume decrease and the axial pressure for soft fluffy powders subjected to cold compression through applying a certain range of pressures. The dependence of the axial pressure on the volume shrinkage was shown to be nearly linear. This equation was lately found to be best used for components with low pressures and high porosities from vibrational or tapping densification [40].

Other than aforementioned investigations which resulted in empirical expressions between powder volume and applied pressure, continuum mechanics was also hired to correlate the volume change and the stress state in cold die compaction. Plastic deformation of porous media has been considered to be the controlling mechanism. Fleck [41] developed constitutive models for cold compaction of powders under general level loading. Cohesive strength between particles and the inter-particle friction were both used to evaluate the shape change of the yield surface. The evolution of anisotropy under axial loading was also included in this study. Ariffin and

Gethin [42] carried out a combined mechanical and thermal analysis of cold uniaxial powder compaction. The analysis was coupled via friction and plastic work heating and the local density field. Numerical simulation of cold die compaction of mixtures of soft and hard powder was implemented by discrete element method [43]. Two mechanisms were considered to explain the effect of the hard particles on the compaction behavior. One is the inhomogeneous load distribution introduced by the hard particles and the other is the plastic deformation of the soft particles.

When performing die compaction at elevated temperatures, the term “hot pressing” is applied. It is an important fabrication process for materials used for high temperature applications. In the hot pressing process, pressure and heat are applied simultaneously to the powder based specimen embraced in a rigid die. Hot pressing usually gives faster densification than conventional sintering. The mechanistic aspects of densification and mass transportation in powder materials subjected to hot pressing have been frequently discussed in the literature.

To understand the mechanism which dominates the densification during hot pressing process, Spriggs and Dutta [44] outlined all possible effects, such as diffusion, particle rearrangement and plastic flow in their review paper. By analogy with the steady-state creep studies proposed by Nabarro and Herring [45, 46], the authors suggested the diffusion-controlled grain boundary sliding as the major mechanism of mass transportation. Wilkinson and Ashby [13] introduced the uniaxial power-law creep equations by considering a given set of microstructure and processing conditions, such as grain size, applied pressure and processing temperature. The densification

rates during initial, intermediate and final stages of hot pressing were well evaluated using only the power-law creep equations. Since then, power-law creep due to the diffusional mass transportation has been recognized as the most acceptable theoretical model for the porous body being subjected to hot consolidation process. These ideas have been implemented with respect to specific materials via both experimental and numerical approaches [47, 48]. Obtained results evidenced that such diffusional creep law can be applied to a wide range of powder materials to investigate their densification kinetics during hot pressing treatment.

The introduction of axial pressure largely compensates the need of processing temperatures in hot pressing (~ 20%) compared to those required in conventional free pressure-less sintering. Coble [49] investigated the pressure effects during hot pressing process with elaborating how applied pressure affects initial, intermediate and final stages of hot pressing. The author also correlated the effective stress with the applied stress and the relative density. Highly applied pressure was proven to be able to induce phase transformation of nano-structural titanium dioxide as it dramatically lowered the processing temperature [50]. The amount of the transferred phase was also proportional to the magnitude of the applied pressure. Moreover, pressure shortens the required processing time and limits the grain growth. Finer microstructure favors obtaining designable features from processed specimens, including optical, electrical and mechanical properties. These benefits can be implemented by carrying out hot pressing of selected materials, as what has been adequately addressed in the referred studies [51, 52].

1.1.1.3 Isostatic and quasi-isostatic pressing loading modes

In isostatic pressing, as presented in Figure 1.4 a, forces are applied equally onto the specimen from all the directions. During isostatic pressing, powders are first enclosed in a flexible, sealed container and then the powder loaded container is placed into a pressure vessel filled with a pressurizing medium in either liquid or gas form. For isotropic materials, shrinkage occurs uniformly along all directions and usually no shape distortion is present after isostatic pressing, as described in Figure 1.4 b. Such a compaction process does not require a direct contact between powders and tooling. The use of isostatic pressing ensures a uniform compacting pressure throughout the powder mass and a homogeneous density distribution in the final product.

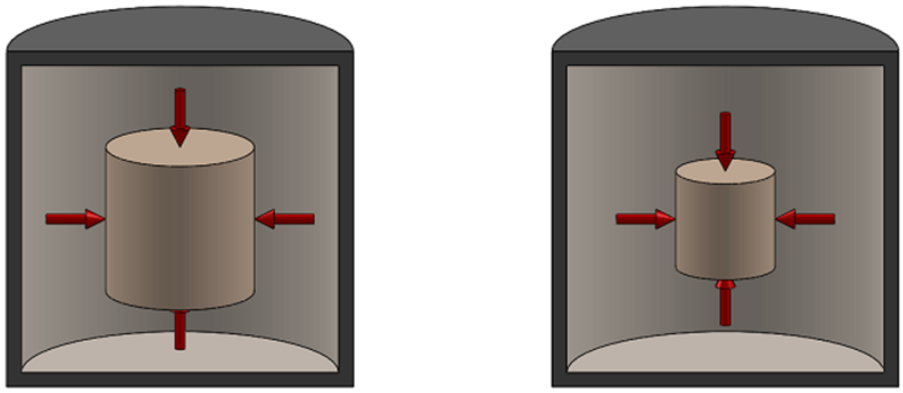

Figure 1.4 Deformation schematics of isostatic pressing loading mode: (a) Before deformation, (b) After deformation.

Since the shape distortion is negligible in isostatic pressing process, the analogous "stiffness" of powder specimen subjected to isostatic pressing setup goes to negative infinity, as expressed below,

$$\frac{\dot{e}}{\dot{\gamma}} = \frac{3\dot{\varepsilon}_r}{0} = -\infty \tag{1.6}$$

Depending upon whether consolidation occurs at either ambient or elevated temperature, the process is called either cold isostatic pressing (CIP) or hot isostatic pressing (HIP), respectively. Cold isostatic pressing is conducted from room temperature to about 100 ℃. The container is typically a rubber or other elastomeric materials and the pressurizing medium is a liquid such as water or hydraulic oil. However, for high temperature hot isostatic pressing, the container is made of metal or glass and the pressurizing medium is an inert gas (argon or helium). The combination of heat and pressure during HIP process avoids the need of a subsequent firing of the specimen and provides a one-step production of articles with high density level.

The rigid-plastic behavior of porous media under conditions of cold mechanical treatment has been recognized as the major controlling mechanisms for densification of powder compacts under CIP. Fleck *et al*. [53] developed a macroscopic constitutive law for plastic yielding of powder compacts at low relative densities ranging from 0.64 to 0.9, in which the contact yield surface appeared to be sensitive to pressures as well as deviatoric stresses. This contact - yielding criterion was soon applied by Govindarajan and Aravas [54] to describe the plastic behaviors of metal powders during CIP, in which the constitutive equations were implemented by

finite element method to analyze the CIP of titanium powder and a good agreement between modeling and experimentation was obtained.

Power low creep, as discussed in the last section, is a dominant mechanism that has been considered in studying the constitutive behavior of porous bodies during the hot consolidation process. A number of investigations have been conducted to analyze the constitutive law governing the HIP of powder specimens. Among these studies, Ashby and co-workers should be first noted, who have contributed to sufficiently elaborated diagrams [55, 56], clarified mechanisms [57], and models [58, 59] describing HIP of various materials. In Ref. [59], the author used a statistical method to assume the sintering of uniform spherical powders in order to determine the number of contact neighbors, effective stress and densification rate. Olevsky *et al*.[60] correlated the HIP conditions of metal matrix composites with the continuum theory of sintering when analyzing the distribution of micro-stress and deformation around fibers. Duva and Crow [61], Besson and Abouaf [62] contributed also to formulate the creep law of powders exposed to CIP treatment, in which the dependence of specimen's macroscopic properties such as bulk and shear moduli on the porosity was adequately analyzed.

Although pressing in a rigid die and isostatic pressing setups have the same deformation mechanisms, the later owns a much better loading regime which increases the possibility of obtaining more deformation at the same heating level compared to the former. Besides traditional isotactic pressing processes, quasi-isostatic pressing (QIP) has been attracting attention as it is less costly and more manageable compared

to isostatic pressing. The deformation schematics of QIP are illustrated in Figure 1.5. Instead of using liquid or gaseous pressurizing medium in the traditional isostatic pressing process, the green specimen is inserted into a solid granular pressure-transmitting medium (PTM), which is itself inserted in a rigid die. Upon the application of uniaxial load, the PTM redistributes the stresses onto the embedded specimen. The generated stress state is called quasi-isostatic, in order to differentiate from the traditional isostatic pressing mode.

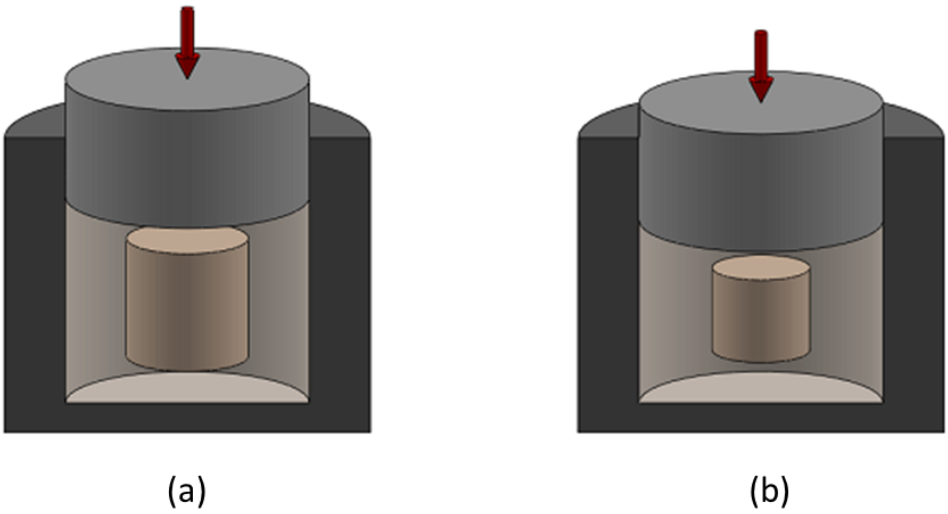

Figure 1.5 Deformation schematics of quasi-isostatic pressing loading mode: (a) Before deformation, (b) After deformation.

Even though quasi-isostatic pressing has been utilized in the manufacturing industry, particularly in combination with self-propagating high-temperature synthesis [63, 64], few theoretical studies were conducted to look at the constitutive behaviors related to this loading mode. Olevsky *et al*. [21] studied the deformation behavior of the PTM as well as of the powder specimen subjected to QIP using the constitutive

law of sintering. The authors found that the axial/radial strain rate ratio of the specimen to a large degree depends on the initial porosity of the PTM. The obtained loading mode that the specimen actually experiences can swing among free up-setting, pressing in a rigid die and isostatic pressing when different initial porosity is assigned to the PTM. The ideas obtained from this study were then applied to produce TiC-Ni-Ti composites, in which elemental Ni, Ti and C powders were surrounded in graphite / alumina particles and densified by quasi-isostatic pressing [65].

1.1.2 Loading control for optimizing properties of consolidated final products

It has been generally accepted that application of mechanical load, no matter what loading mode is used, significantly influences the densification kinetics of powder compacts as well as the physical properties of final products. Theoretically, the applied pressure, on the one hand, removes large pores from powder compacts via plastic flow. On the other hand, it provides an extra driving force to promote the coalescence of particles. Practically, maximum processing temperature and isothermal dwelling time in pressure-assisted sintering processes are significantly decreased due to the applied pressure, resulting in obtaining properties which are not attainable via conventional pressureless sintering techniques.

Typically, load or pressure is kept constant during cold or hot processing of powder materials. Residual porosity is usually eliminated by increasing the applied pressure if the device's maximum heating capacity is reached. This approach sometimes appears to be less applicable as the magnitude of the applied pressure is usually determined by the capacity of the loading unit and the strength of the tooling

material. Therefore manipulations of load or pressure have been attempted to improve the compaction / consolidation process of powder materials. Conducted practices spread into cold and hot processing regimes, the obtained results were compared to these from carrying out control runs with constant load or pressure.

Huang and Daehn [66] applied cyclic pressure to densify composite powder at room temperature. Various lead-alumina mixed powders were subjected to a large number of loading cycles where the uniaxial pressure varied from 0 to a constant peak value. The compacted density was found to increase with increasing the pressure amplitude and the number of cycles, but not related to the changes in frequency. When compared to composites produced by static compaction, those fabricated with cyclic pressure showed a significant increase in hardness and rupture strength. The authors also conducted an extensive study of the same composite in a later publication, in which the compressibility difference between two elemental powders was considered [67]. A criterion was proposed based on the ratio of the linear elastic mismatch strain to the matrix yield strain, in order to evaluate the effectiveness of pressure cycling on the level of densification.

The uniformity of aluminum-alumina matrix composites from cyclic pressing was examined by Fu *et al*. [68]. Results showed that the spatial density of uniformity was improved and the distribution of ceramic phase was more uniform after cyclic compaction compared to monotonic compaction. It was also found that the influence of pressure cycling on the density distribution increases as the aspect ratio of powder specimen increases. The authors attributed those benefits to the adhesion improvement

of the bonding process during pressure cycling. Zavaliangos and Laptev [69] studied the effects of different volume fractions of reinforced particles in the cyclic pressing of lead-alumina composites. The density and strength of specimens from cyclic pressing were tested to be higher than their counterparts obtained from static pressing and to be enhanced with increasing the presence of alumina. The influence of cyclic pressing on the idealized densification was investigated by Jiang *et al*. [70] using finite element simulation. Besides pressure amplitude, the authors showed that the inter-particle friction was able to facilitate cyclic compaction but hinder static pressing.

Shaik and Milligan [71] used rapid powder forging technique to limit grain growth when consolidating nanostructured Fe-10Cu powders at elevated temperatures. The loading rate was varying between 35 and 525 MPa/s and specimen's creep behaviors were then examined. Obtained specimens exhibited relatively small grain sizes and good properties during hardness and compression tests. Also, power-law creep was observed during the process which indicated that creep was the dominant densification mechanism in rapid forging. A similar idea was hired by Zhan *et al*. [72] to demonstrate ultra-low temperature superplasticity from nanoceramic composites. Pre-sintered porous specimens were superplastically deformed by spark plasma sintering at low temperatures. High loading rate was applied after the desired temperature was achieved. Both rapid strain rate and large total compressive strain were observed in the specimens without cracking. The final products showed nano-sized grains and exhibited excellent optical properties.

Chaim and Shen [73] claimed that the grain size can be controlled by pressure application regime during spark plasma sintering of nano-powders. Application of pressure at moderate temperature resulted in homogeneous compaction of powders with narrow size distribution while application at high temperature might cause significant coarsening of powder and bimodal distribution in turn. Olevsky *et al*. [74] discussed the pressure application influences on the formation of inter-particle bonds in different materials. The application of pressure at the initial stage was proven to facilitate deformation of metal powders but impede rearrangement of ceramic powders.

Two-step pressure sintering was applied to produce transparent lutetium oxide in spark plasma sintering furnace [75]. By rapidly increasing pressure from 10 to 100 MPa under a constant heating rate, the grain growth in the specimens was prevented and highly transparent final products were obtained. A newly developed multi-step pressure dilatometry was used by Li *et al.* [76] to examine the densification mechanisms in sparking plasma sintering of copper powders. By assuming the microstructure is invariant near the vicinity of instantaneous pressure rise, the instantaneous strain rates under different pressure levels were used to evaluate the stress exponent of the power-law creep equation.

While the above-mentioned examples of studies involved various material systems including metal and ceramic powders, the present work is focused on the consolidation of ultra-high temperature ceramics. Below, the results of the respective literature survey are presented.

1.2 Consolidation of Ultra-high Temperature Ceramics: Literature Survey

1.2.1 Various UHTC consolidation techniques

Ultra-high temperature ceramics (UHTCs) are a class of compounds that offer excellent combinations of physical and mechanical properties, including extremely high melting temperatures (> 3000 °C), high strength and good chemical resistance at high temperatures. Typical UHTCs are the carbides, nitrides and borides of transition metals. Usually, the group IV-V compounds such as titanium, zirconium, hafnium, and tantalum are generally considered as the main research interest, particularly in the investigation of the preparation and characterization of bulk materials made out of powder-based UHTCs [77].

The above mentioned unique properties of UHTC, especially the high melting point and high-covalent bonding, actually provide challenges to the consolidation of UHTC powders. Achieving a fair level of consolidation usually requires high temperature exposure. For example, zirconium diboride (ZrB_2) powders were sintered by Chamberlain *et al*. [78] without applying external pressure. After holding for 540 minutes at 2150 ℃, a relative density of 98% was reached. The four point bend strength was measured to be comparable to the hot-pressed ZrB_2, while the Vickers' hardness was significantly lower compared to its hot-pressed counterpart. The effects of particle size and sintering additives on pressureless sintering of ZrB_2 were examined by Fahrenholtz *et al*. [79], in which the average particle size was milled down to 0.5 μm and nearly full density was retrieved at 1850 ℃. The reduction of

particle size enhanced the sinter-ability of the powders, but also increased the oxygen-based impurities content in the powders which would act as obstacles during sintering.

Pressure assisted sintering was utilized to consolidate UHTCs, both uniaxial and isostatic pressing were employed. Without sintering additives, Zhang *et al*. [80] reported that the temperature required for achieving 96% relative density in the hot pressing of tantalum carbide (TaC) was around 2400 ℃. Although the introduction of sintering additives lowered the peak temperature by approximately 200 ℃, rapid grain growth was observed. Sanders and Grisaffe [81] determined the effects of the hot-pressing variables on the densification kinetics of micro-sized hafnium carbide (HfC) powder. Various temperatures and pressures were applied and HfC bodies with 98% relative density were produced after holding 15 minutes at 2300 ℃ with a hydraulic pressure of 25 MPa. Further literature survey also suggested that hot pressing appears to be the most widely used technique to consolidate high temperature borides, such as ZrB_2 [82] and hafnium boride (HfB_2) [83, 84]. All reported maximum processing temperature were over 2000 ℃ when sintering aids were not present.

It is worth mentioning that ultra-high pressure (~7.7 GPa) was successfully applied by Lahiri *et al*. [85] to produce fully dense TaC specimens using a composite tooling setup in a hot pressing device. Under an extremely high hydraulic pressure, the peak processing temperature was reduced to 1830 ℃. The authors also pressed the TaC powders at ambient temperature with keeping the sample pressure level, the specimen was compacted to a bulk structure with 90% relative density. However, the deformation mechanisms operating at room temperature and high temperature were

found to be significantly different. The elastic modulus and hardness of specimens produced by high-temperature consolidation were largely increased.

Few studies were dedicated to HIP of UHTCs. Besson *et al*. [86] applied HIP to the production of near-net-shape fully dense titanium diboride (TiB_2) parts. The rheological behavior was studied and a constitutive finite element model was built to analyze the density and stress evolution with predicting the final shape. Transverse strength, hardness and toughness of the densified TiB_2 products were examined to be equivalent or better than the data published in the past, which evidences the efficiency of the employed consolidation technique on the processing of UHTCs. A series of TaC and HfC powder mixtures were brought to hot isostatic pressing with the purpose of investigating the effects of the HfC content on the TaC microstructure and the obtained properties [87]. It was shown that with increasing HfC content, the TaC grain size decreased and the microhardness increased in turn. Also, the addition of HfC was able to improve the oxidation resistance of the sintered specimens.

Consolidation of UHTCs at moderate temperatures via reactive sintering has attracted research interests due to its ability to obtain a chemically stable phase composition as well as physically clear microstructures in the produced materials. Reactive hot pressing was investigated as a promising approach to produce dense monolithic ZrB_2 from elemental Zr and B powders [88]. Milled powders were first held at various low temperatures for a few hours in a hot pressing die to allow the reaction between Zr and B to proceed. The pressure was applied at peak processing temperature of 2100 ℃ and released during the cooling stage. Specimens were

measured to possess relative densities around 99% and their mechanical properties were comparable to those retrieved from conventional sintering processes.

Self-propagating high-temperature synthesis (SHS) of TiB_2 based ceramics matrix composites were conducted using elemental powders of Ti, B and C through exothermic reactions [89]. The effect of the fraction of TiB_2 on the initiation of self-propagation was investigated and an intended molar ratio was suggested. The reaction completeness was proved to be able to affect the microstructural homogeneity and hardness. Note that the main difference between SHS and reactive sintering is whether the reaction can be controlled or not. Once the self-propagation is ignited at the heating point, the exothermic reaction will sweep through the remaining reactants. This process is hard to control and often results in an incomplete reaction. Whereas the reactive sintering relied on a controlled reaction in which the products are formed relatively slow and the completeness of reactants are then ensured.

Above-mentioned studies were conducted using conventional devices, in which the specimens were heated up slowly by the resistive heating elements. In these cases, usually up to several hours of holding was required to obtain highly dense products due to slow densification kinetic. Fast consolidation can be reached by applying rapid heating techniques such as high frequency induction heating. Kim *et al*. [90] produced bulk TaC specimens with a relative density of up to 96% in an induction furnace. Nano-sized TaC powders were pressurized in a graphite die with itself being wrapped by an induction coil. The target processing temperature was

reached within 3 minutes and the densification kinetics was significantly intensified with the assistance of the applied pressure.

Spark plasma sintering (SPS), also known as field-assisted sintering or current-assisted sintering technique, is currently one of the most attractive rapid sintering techniques. This state-of-the-arts technique is capable of coupling Joule heating and mechanical pressing in the densification / consolidation process of powder materials. The Joule heating effect brings high heating rates as well as high temperatures into the volume of the sample which largely shortens the processing time [91]. At the same time, the applied pressure appears to be able to significantly influence the densification by enhancing the mass transportation mechanism [16]. Therefore, SPS has been recognized as an excellent solution to sufficiently consolidate UHTCs [92].

Bellosi *et al*. [93] investigated the suitability and efficiency of applying SPS to produce UHTCs such as HfB_2 and ZrB_2. Compared to hot-pressing, SPS exhibited lots of advantages including successfully consolidate these poorly sinterable powders in a shorter period of time without adding sintering activators. Comparisons between SPS and conventional techniques were also reported in other studies [94, 95]. For example, Mizuguchi *et al*. [94] used transmission electron microscope and energy dispersive X-ray to exam the content of impurities in SPS-processed and hot-pressed ZrB_2. It turned out that SPS has a so-called cleaning effect on the powder surface due to the electrical discharges generated between particles. In another study, Khaleghi *et al*. [96] consolidated TaC powders with the purpose of characterizing various properties of the final products prepared under different SPS processing conditions. It was shown that

high densification was accompanied by substantial grain growth in pure TaC but the addition of carbon nanotubes was able to mitigate grain growth to a certain extent.

The applied aspects of the present study are focused on the optimization of the fabrication of ZrC powder components. Below a literature survey of the earlier studies on the consolidation of ZrC powders is presented.

1.2.2 Hot consolidation of zirconium carbide

Zirconium carbide (ZrC), as a typical UHTC, owns good thermo-mechanical properties, high electrical and thermal conductivity, high melting temperature and strong chemical resistance. It has been recently considered as a promising candidate for furnace elements, arc plasma electrodes and future nuclear reactors [97-99]. The possession of high melting temperature (~ 3500 °C), plus the inherent nature of the covalent Zr – C bonding, leads the effective sintering of ZrC powders at relatively low temperatures into a fairly unattainable situation. Therefore hot powder consolidating techniques have had to be commonly utilized to prepare bulk ZrC products, most of the time under the assistance of external pressure.

Free pressureless sintering of ZrC powders was performed by Bulychev *et al*. [100], in which the nearly fully dense ZrC pellets were obtained between 2600 °C and 2800 °C in protected atmospheres. The effects of porosity and average grain size on the rupture strength of sintered ZrC were discussed separately and empirical expressions were generated to describe these dependences. It was shown that porosity influences the rupture strength linearly while grain size is nonlinearly related to the

rupture strength. Zhao *et al*. [101] enhanced the sinterability of ZrC powder through high-energy ball milling and consolidated the milled powder composite into a 98% relative density at 2100 ℃ via the free pressureless sintering process.

Compared to free pressureless sintering, hot pressing seems to be a more efficient technique for the consolidation of transition metal carbides. In Ref. [102], ZrC specimen with 94% - 96% relative density were obtained from carrying out hot pressing of ZrC powders at 2200 ℃-2600 ℃ under a pressure of 20 MPa. Barnier *et al*. [103] reported that a 98% relative density was reached by hot pressing ZrC powder at 2300 ℃, in which a 40 MPa pressure was applied upon the arrival of the maximum processing temperature. The poor sinter-ability of ZrC has seen from these two studies: a large increase in the pressure magnitude was not able to bring in a substantial increase in the densification level. Densification mechanisms of ZrC powders under hot pressing were also investigated in these works and a diffusional creep mechanism was verified by both morphological and non-Newtonian models.

Sintering additives were used to improve the sinter-ability of ZrC powder in hot-pressing. Minhaga *et al*. [104] showed that the densification kinetics of ZrC was enhanced by adding yttria-stabilized-zirconia. The powder beds were sintered to the nearly theoretical density at 2000 ℃. Wang *et al*. [105] mixed ZrC powder and Zr additives in a certain ratio and hot-pressed them at 1900 ℃ -2000 ℃. The doped powder was consolidated to higher final relative density (>98.4%) than the additive free ZrC. The rapid grain growth was observed in the doped final specimens, whereas

the proper introduction of graphite powder was found to be able to refine the microstructures and maintain a similar level of densification.

Reactive hot pressing was applied to obtain monoclinic ZrC pellets from Zr and C powders [106]. Various molar ratios between Zr and C were considered. Two elemental powders were first heated up to 1200 ℃ – 1400 ℃ to let them partially reacting with each other and then subsequently subjected to hot-pressing at 1800 ℃ to achieve full density. The optimal ratio between Zr and C for improving densification was determined to be 1.5. Since hot pressing usually accompanies with long term holding at the maximum processing temperature to achieve the desired densification level, the grain growth in the hot-pressed specimens seems to be inevitable. As mentioned before, large grains are harmful to the strength of materials. In order to prevent grain growth, advanced rapid sintering techniques were considered.

SPS has been widely accepted as the most attractive technique to work with UHTCs. Various benefits of applying SPS on consolidation of refractory materials, such as high heating rate, high pressure and grain size retention have been highlighted in recent review papers [16, 91, 107, 108]. SPS has been applied to consolidate ZrC powders since 2006. Ryu *et al.* [97] first reported the 63% relative density ZrC specimens were obtained at 1500 ℃ under 30 MPa, while the addition of Dy_2O_3 promoted the increase of the relative density level by 5%. Micron-sized ZrC powders were SPS-processed by Sciti *et al.* [109], up to 98% relative density was achieved at 2100 ℃ under 65 MPa within 3 minutes holding. $MoSi_2$ was used as sintering aids

and it was able to lower the maximum processing temperature without augmenting the grain size of the final specimens.

Submicron-sized zirconium oxy-carbide (ZrC_xO_y) powders were synthesized and consolidated around 2000 ℃ by Gendre *et al.* [110] using SPS, while the oxygen sites and vacancies introduced by the carboreduction synthesis of such powder were considered to be the factors to facilitate densification in a later study [111]. The oxy-carbide stoichiometry appeared to have significant effects on mechanical properties of SPS-processed specimens. High energy ball milling was employed to bring the crystalline size of as-purchased micron sized ZrC powder down to nano range [112]. SPS of these milled powders exhibited a large enhancement in densification kinetics and obtained finer microstructures in final products. Nano ZrC powders were also prepared from a novel sol-gel method by Xie *et al*.[113]. Up to 99% relative density was achieved and limited grain growth was observed as well after processing the obtained nano ZrC powders via SPS at 1750 ℃.

The mechanisms of rapid densification during SPS process also drew lots of attentions. Research interests include, but not limit to, the electric field / current effects [17, 114-116], high heating rates [117] and diffusional effects [118, 119]. Although these features have provided SPS with excellent abilities to effectively consolidate poorly sinterable powders, few studies are dedicated to its net-shaping capabilities on hard and refractory materials. Producing complex shaped components from SPS was studied by Tokita [120, 121], who introduced using tunnel-type SPS manufacturing system to fabricate tapered and square shaped hard alloy components

for industrial applications. Olevsky *et al*. [122], analyzed the net-shaping capabilities of SPS both theoretically and experimentally. Cylindrical and prismatic shapes alumina specimens were produced to study the impacts of shape factors on their properties. However, none of the conducted studies were specifically focused on any type pf UHTCs.

1.3 Research Incentives and Objectives

1.3.1 Research incentives

The conclusions of the literature survey in above sections can be summarized as follows, and the research incentives are formulated accordingly:

Three major loading modes, free up-setting, pressing in a rigid die and isostatic / quasi-isostatic pressing have been adequately applied to process porous materials in both cold and hot processing regimes. The deformation schematics of a porous body subjected to various loading modes were illustrated with respect to the preset boundary conditions (See Figure 1.1 Figure 1.5). The effectiveness of each loading mode, or in other words, how intensively the body deforms when subjected to a certain loading mode, was represented by the ratio between the volume change rate, $\dot{e}$, and the shape change rate, $\dot{\gamma}$, as formulated in Equations (1.3) - (1.6). All the obtained expressions, namely the analogy of "stiffness" are qualitatively plotted together on orthogonal axes, as shown in Figure 1.6 with the arrows indicating the deformation path for an individual loading mode.

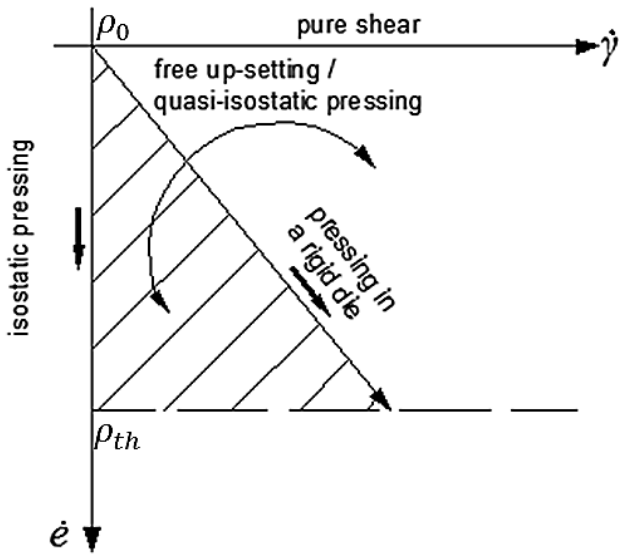

Figure 1.6 Combined plots for the "stiffness" analogy and indications of the deformation paths for the discussed loading modes.

As one can see, pressing in a rigid die and isostatic pressing appear as straight lines. All deformation paths are bounded by the pure shear, the isostatic pressing and the theoretical density (ρ_{th}) lines. Pressing in a rigid die line crosses the bounded region with a fixed slope ($-\sqrt{6}/2$), while paths for free up-setting can lie above (the blank division) or below (the hatched division) the pressing in a rigid die line depending on the actual stress-strain states. Also, it is necessary to restate that the quasi-isostatic pressing, as elaborated by Olevsky *et al*. [21], can switch among these three loading modes depending on the initial porosity of the pressure transmitting medium. It seems that the deformation paths of pressing in a rigid die and isostatic pressing are pretty much pre-described no matter how they are carried out. However, free up-setting and quasi-isostatic loading modes own the possibilities to manipulate

the deformation and influence the densification of a porous body during its consolidation process.

Thereby, the benefits of loading control in the pressure-assisted consolidation of powder-based components have been revisited. Compared to applying load consistently, changing load intentionally during the pressing process not only facilitates the consolidation but also improves the properties of final products in many aspects. Cyclic pressing was proven to be able to homogenize the density uniformity and obtain better mechanical properties in the cold compaction of metal-ceramic composites. Varying loading rates at different hot pressing stages could help limiting grain growth and retrieving desired product properties. Ceramic specimens displayed super-plasticity without cracking when subjected to rapid loading rate SPS. The occasion of pressure application during SPS process was of importance for grain size retention and inter-particle neck formation. Two-step and multistep pressure regimes were also implemented in SPS process, which could be considered as more advanced investigations of loading control. Therefore, in the pressure-assisted sintering process, a loading control profile, such as magnitude, rate and duration, can be added on top of a loading mode to optimize the densification efficiently of porous material.

Effective consolidations of UHTC powders have had to be performed at elevated temperature regimes. Conventional hot consolidation techniques usually required either extremely high temperatures (free pressureless sintering) or externally high pressures (hot and isostatic pressing) to be applied and long term dwelling stage at the maximum temperature. Reaction sintering and self-propagating synthesis were

hired to produce bulk UHTCs from their elemental powders. Due to the nature of the exothermic reaction, nearly fully dense specimens could be obtained at relatively lower processing temperatures using both techniques. Rapid heating techniques have been utilized to consolidate UHTCs, especially the SPS process, in which the coupled Joule heating and field effects largely facilitate the densification kinetics of poorly sinterable UHTC powders.

Hot consolidation of ZrC powders has been particularly emphasized in the conducted literature survey. The conventional pressureless or pressure-assisted sintering techniques appeared to be able to sufficiently process ZrC powders only at extremely high temperature regimes which indicated the poor sinter-ability of ZrC. This situation could be improved to some degree by milling or doping the starting powders. Reactive hot pressing was employed to produce fully dense ZrC specimens from ultrafine Zr and C powders at relatively lower temperatures. Since conventional consolidation techniques could cause significant grain growth and reactive sintering might encounter reaction completeness issue, a rapid sintering technique - SPS has been recently utilized to fabricate ZrC specimens with high densities. Conducted SPS treatments of ZrC were mainly focused on improving densification kinetics either by reducing initial particle size down to submicron or even nano range via various approaches. Limited grain growth and enhanced mechanical properties were observed in the SPS-processed ZrC specimens.

Among the aforementioned different loading modes, isostatic pressing has been shown to own the highest potential for the production of high density articles.

Regarding the applications, isostatic pressing devices are costly especially at high temperature regimes and this technique is currently not compatible with SPS operational requirements. Pressing in a rigid die appears to be adaptable to all types of modern SPS machines and provides substantial densification for most materials. However, when it comes to hard-to-deform materials such as UHTC, it appears that pressing in a rigid die enables no specific effects enhancing densification at later SPS stages [123, 124]. In addition, traditional SPS process always proceeds with fixed loading schematics making the optimization of the SPS efficiency less feasible. Manipulation of loading modes should be attempted to manage the densification as well as to control the structure in SPS processing of UHTC powders such as ZrC.

1.3.2 Research Objectives

By putting together the conclusions drawn from the conducted literature survey, the research objectives of the present study can be extracted as the follows:

a. Investigation of the influences of the loading modes on the densification efficiency of spark plasma sintering. This objective is aimed at manipulating the pressure application schematics in order to elucidate the loading mode-based densification kinetics as well as to optimize the densification efficiency in the spark plasma sintering process.

b. Fabrication of high density carbide components with tailored structures and high temperature applications via spark plasma sintering technique. This

objective is targeted at exploring the capabilities of net-shaping in spark plasma sintering of UHTC powders.

1.3.3 Research Tasks

Three main research tasks are composed with the purpose of achieving the above-formulated research objectives in an organized way as the follows:

a. Characterizing densification kinetics and correlated behaviors of ZrC powders subjected to traditional SPS process.

This task includes, first of all, carrying out the SPS consolidation of ZrC powder to investigate its densification kinetics under different heating and loading regimes. Various experiments are conducted to map the densification level with respect to processing conditions. Then the influences of processing parameters on the evolution of microstructures have been also elucidated. The relative densities and average grain size of the obtained ZrC specimens are used to identify the measured mechanical and thermal properties. To theoretically study the densification kinetics of ZrC under SPS conditions, the continuum theory of sintering is employed to derive an analytical densification equation based on the boundary conditions imposed by the SPS setup. The determination of the unknowns in the constitutive densification equation provides necessary supporting data to the research objectives a) and b). However, it requires further clarification of electrical and thermal aspects regarding the currently employed SPS tooling system.

b. Optimizing loading schematics for enhancing the densification efficiency in SPS of porous ZrC via experimental and theoretical approaches.

The contact resistances in the SPS tooling setup are experimentally evaluated with respect to the applied pressure and the processing temperature. These obtained resistances' values are employed in the investigation of the temperature distribution in SPS of ZrC through finite element simulations. The densification equation derived in task a) is then solved numerically with revealing the creep coefficients of ZrC under SPS conditions. Free up-setting mode is then implemented in SPS process (SPS-forging setup) to consolidate porous ZrC bodies. The densification kinetics obtained from SPS-forging is compared to the one retrieved from regular SPS under the same processing conditions. The continuum theory of sintering is employed again to theoretically interpret the loading mode-induced densification behaviors. The advantages of SPS-forging and regular SPS are combined to form a hybrid loading mode SPS regime to give the optimal loading mode, in which loading control also imposed to ensure the densification level. This task fulfills the research objective a).

c. Fabricating annular shape carbide components for using SPS and investigating the potential applications of this complex geometry.

This task logically extrapolates the experimental - theoretical optimization of the SPS process into the particular interests of achieving net-shaped SPS products. Annular shape ZrC pellets are fabricated using specially designed

SPS tooling to meet the geometrical requirements for potential applications. Finite element simulation is employed to analyze the dynamic interaction between the complex shape powder bed and the vulnerable tooling components during the SPS process. The utilized processing procedures are subsequently scaled up to produce annular shape carbide composites, whose performances at high temperature are demonstrated to be promising for being potentially used as an alternative SPS tooling material. Also, the developed modeling framework is extrapolated to investigate the behaviors of annular shape nuclear fuel pellets during high temperature services, to which the continued radiation and sintering conditions are simultaneously encountered. This task addresses the research objective b).

Above-mentioned research tasks are lined up with the corresponding research objectives in the flowchart shown in Figure 1.7. Also, subtasks are formulated at the bottom of the flowchart to provide the details of each major task. Again, all tasks are dedicated to the implementation of the research objectives of the present work.

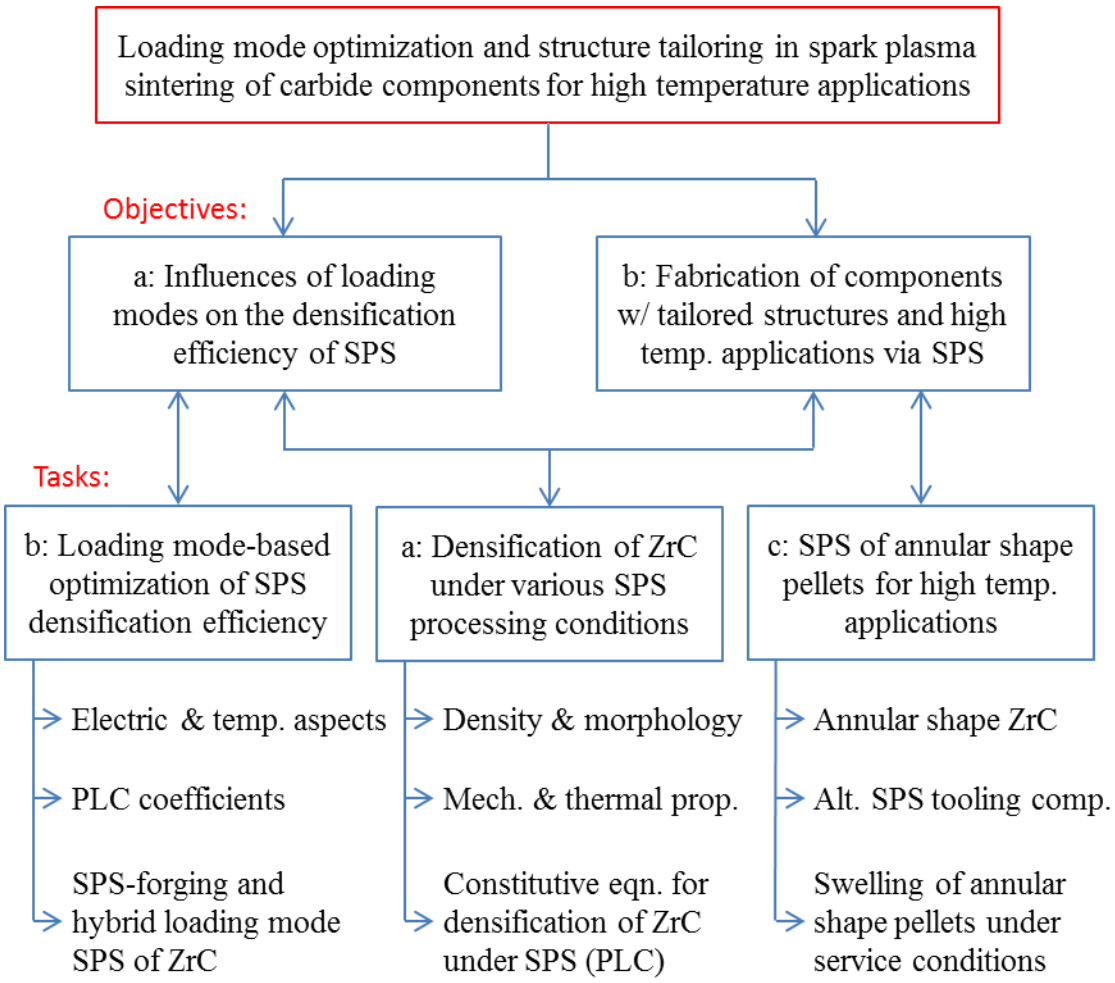

Figure 1.7 Flowchart of formulated research objectives and tasks.

CHAPTER 2 SPARK PLASMA SINTERING OF ZIRCONIUM CARBIDE POWDER

In this chapter, spark plasma sintering (SPS) technique utilized to consolidate micron sized zirconium carbide (ZrC) powders is described. To construct an SPS densification map of the selected powder, SPS runs were carried out under various processing parameters. Besides regular SPS runs, double-die SPS and conventional hot pressing of same powder were comparatively conducted. The influences of applied pressure and electric current on the densification kinetics of ZrC subjected to SPS conditions were shown accordingly. Microstructures of SPS-processed specimens were compared to reveal the effects of current, pressure and temperature on the final specimen's micromorphologies. The mechanical properties of the SPS-processed ZrC specimens were measured to be functions of their relative densities and average grain sizes. The porosity evolution in regular SPS of ZrC was investigated utilizing the continuum theory of sintering [125], where the power-law creep equations were incorporated with taking into account the porosity dependence. The obtained analytical equation is supposed to be solved and regressed with the experimental data to determine the creep coefficients of the employed ZrC.

2.1 Densification Kinetics of ZrC Processed by Spark Plasma Sintering

2.1.1 Characterizations of starting ZrC powders

Commercial zirconium (IV) carbide powder (ZrC, 99% metal basis, Sigma-Aldrich Co., St. Louis, MO, USA) was chosen as a tested material in the conducted

experiments. The as-received powder was first subjected to ultra-sonication (2510 ultra-sonic cleaner, Branson Corp., Danbury, CT, USA) for de-agglomeration. The raw powder was then analyzed by scanning electron microscopy (SEM, Quanta 450, FEI Co., Hillsboro, OR, USA) to examine its morphology. As shown in Figure 2.1 a, the raw powder is a combination of small flakes and large kernels with an average particle size of 10 μm. A single particle (Figure 2.1 b) exhibits a polycrystalline structure and, when examining under high magnifications, inter- and intra-granular pores are present as well. Figure 2.1 b also indicates that the average grain size of the raw powder is around 1 μm

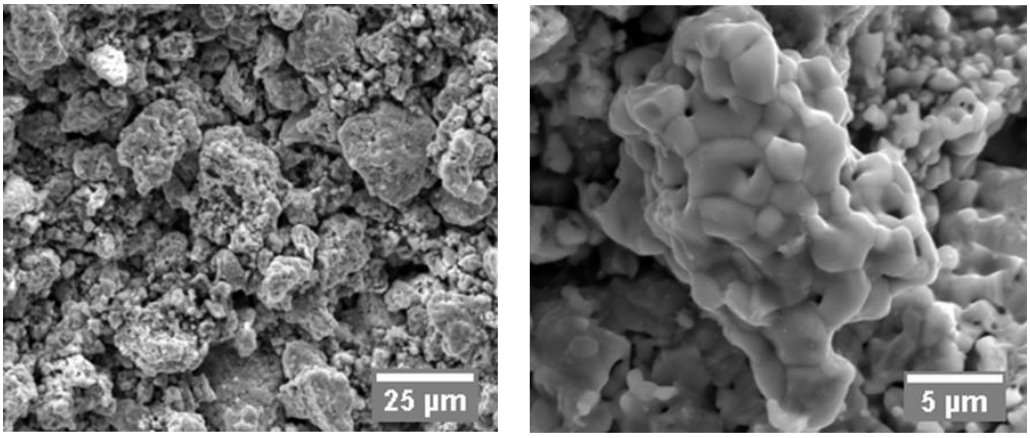

Figure 2.1 SEM images of as received ZrC powder: (a) 1000x, (b) 5000x.

The pycnometric density of the initial particles was measured to be 6.605 g/cm^3, by Helium pycnometer (AccuPyc 1330, Micromeritics Corp, Norcross, GA, USA). Due to the existence of internal particle porosity, the absolute density is slightly lower than the computed theoretical density of ZrC based on the crystallographic

properties (6.70 g/cm^3[101]). X-ray diffraction (XRD, X'pert Pro, PANalytical B.V., Almelo, the Netherlands) of the raw powder was performed using copper as a target, diffracted patterns (solid line) are compared to reference peaks (ring markers) along each diffracted plane in Figure 2.2. Additionally, the lattice parameter of the starting powder was estimated at every diffracted plane to give an average value of 4.698 Å. Since it only showed a negligible difference in comparison to the theoretical value (4.699 Å, [126]), the XRD analysis has identified that the raw powder was very close to the stoichiometry of ZrC. Energy dispersive X-ray spectroscopy (EDS, X-Max-50 detector, Oxford Instruments, Concord, MA, USA) determined the atomic ratio (at.%) between zirconium and carbon as close to 1**.** Above-discussed powder properties are listed in Table 2.1.

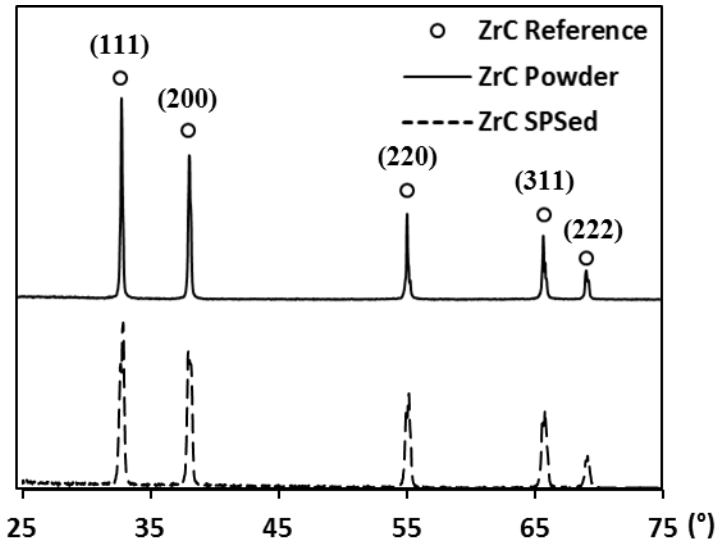

Figure 2.2 XRD patterns of raw powder (solid line), SPS-processed specimen (dash line) and reference peaks (ring markers), respectively.

Table 2.1 Properties and compositions of as received ZrC powder

Powder Supplier	Abs. Density	Ave. Particle Size	Ave. Grain Size	Zr (at.%)	C (at.%)	O (at.%)
Sigma-Aldrich	6.605 g/cm^3	10 μm	< 1 μm	44.74	52.91	2.35

2.1.2 Experimental procedures

All SPS runs were carried out using Dr. Sinter SPSS-515 furnace (Fuji Electronic Industrial Co., Ltd., Kawasaki, Japan). This apparatus is equipped with a maximum uniaxial loading capacity of 50 kN and an output DC current up to 1500 A. The employed SPS tooling setups are illustrated in Figure 2.3. When conducting SPS runs with regular single-die setup (Figure 2.3 a), weighted ZrC powders were placed into a 15.3 mm graphite die with the supports from two 15 mm graphite punches (I-85 graphite, Electrodes Inc., Santa Fe Springs, CA, USA). The internal surface of the 15.3 mm die was properly pre-lined by inserting well-cut 0.15 mm graphite foil (Fuji Electronic Industrial Co., Ltd., Kawasaki, Japan) to improve the contact quality between tooling components and smooth the ejection of the specimen after processing. The loaded powder was pre-compacted in the SPS furnace chamber at room temperature under a load of 3 kN for 3 minutes. The geometrical dimensions of the green specimen at this point were then used to calculate its initial density.

Due to the strength of the graphite material itself, if high axial pressure was applied to the powder bed, especially at high temperatures, the single-walled graphite die could become vulnerable to the internal stress caused by the deformation of the specimen. The application of high axial pressure during the SPS process was

implemented by utilizing a recently developed double-die setup [127]. As illustrated in Figure 2.3 b, a small graphite die with 7.3 mm inner diameter and 15 mm outer diameter was sitting at the center of a large 15.3 mm graphite die to form a double-walled die configuration. Two small 7 mm by 7mm SiC punches (Morgan Advanced Materials, Hudson, NH, USA) were inserted into the small graphite die to hold the powder specimen in place. Two 15 mm large punches were subsequently aligned with the small punches to transmit the external force from the loading unit to the specimen. Since the cross-sectional area of the small punch is approximately 4 times less than that of the large one, by applying the same level of force, the axial pressure generated by the double-die setup at the specimen region can be 4 times larger compared to that constructed by the single-die setup. This double-die setup increases the effective thickness of the die wall, therefore it can survive from the high stress impact.

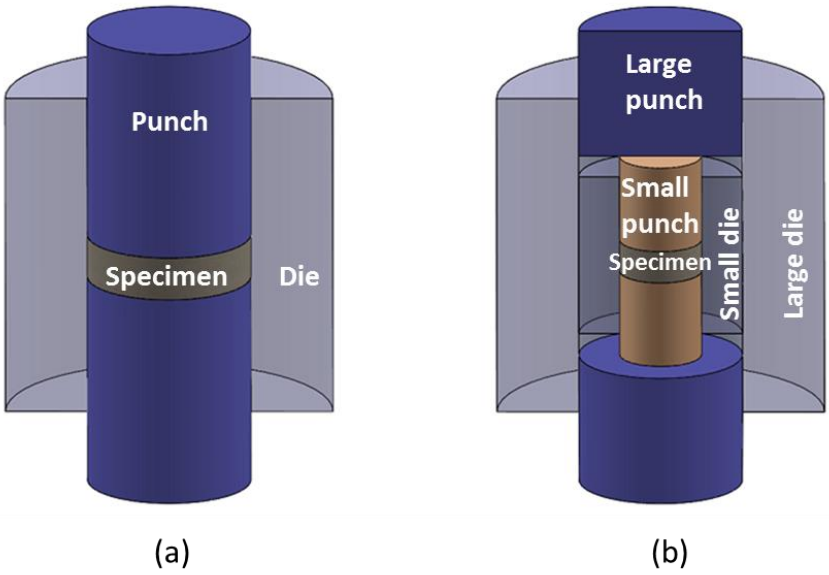

Figure 2.3 Schematics of employed SPS setups: (a) Singe-die; (b) Double-die.

A pulsed current with pulse duration of 3.3 ms and on/off pulse interval of 12:2 was chosen for all SPS experiments. SPS runs were conducted with maximum processing temperature ranging from 1600 ℃ to 1800 ℃. The following heating profile had been used: (i) 6 minutes from room temperature to 580 ℃, 1 minute from 580 ℃ to 600 ℃ and stabilize at 600 ℃ for another 1 minute (3 minutes for double-die SPS due to geometric complexity); (ii) 100 ℃/min to 1600 ℃ and 50 ℃/min to target temperature (if it is higher than 1600 ℃); (iii) dwelling at peak temperature; (iv) cooling down to 1000 ℃ and powering off the machine. Temperature evolution was monitored by pointing a digital radiation thermometer at the outer surface of the graphite die. The hydraulic uniaxial pressure was consistently applied from the beginning to the end of the consolidation process. The real-time processing parameters, such as temperature, applied force and axial displacement were automatically logged by the SPS device.

Besides the electric current assisted SPS runs, conventional hot pressing of ZrC powder was also carried out using a 50 ton hot press furnace (Oxy-Gon Industries, Epsom, NH, USA). The uniaxial pressure in the hot pressing of ZrC was set to 55 MPa. The heating rate was 13 ℃/min to 1800 ℃ and then 2 ℃/min to 1900 ℃. Isothermal holding at 1900 ℃ was 60 minutes. In order to make a comparison, "control" SPS runs with similar external pressure, heating rate and holding time were also implemented. By considering the existence of the temperature gradient between the specimen and the outer die surface during SPS [128], the peak processing temperature in the "control" SPS runs was adjusted to 1600 ℃. Such an adjustment

aimed at making the actual temperature which the specimen experienced during SPS to be comparable to the one that used in hot pressing (see also Section 3.2) Therefore, the hot pressing and the SPS of ZrC were conducted under similar heating and loading profiles.

Argon atmosphere was utilized in all SPS and hot pressing experiments in order to prevent the furnace chamber and the heating elements from being overheated. Graphite tooling was wrapped by carbon felt to reduce heat loss through thermal radiation in SPS runs. For every selected processing profile, an additional blank run was conducted with the absence of powder. The obtained axial readings from this idle run were considered to be the thermal expansion of the graphite tooling under such processing route. The true axial displacement of the specimen during consolidation was therefore able to be evaluated correctly.

2.1.3 Densification of ZrC powder under various conditions

All obtained specimens were ground and polished with abrasive silicon carbide papers as well as colloidal diamond suspension to get them well prepared for characterizations (density, microstructure, mechanical properties, *etc.*). The samples were first analyzed by XRD (X'Pert Pro, PANalytical B.V., Almelo, the Netherlands) to retrieve their phase compositions after high temperature consolidation. The X-ray diffracted pattern of the SPS-processed specimen is compared to that of the raw powder as well as to the reference peaks in Figure 2.2. The lattice parameter of the SPS-processed specimens was calculated to be ~0.2% larger than that of the raw powder. Such an augmentation might be caused by the free carbon in the raw powder

reacting with ZrC during SPS. Since the extent of lattice parameter change could only influence the stoichiometry and lower the theoretical density negligibly, it was considered as minor in the calculation of relative density.

A specimen's density was first calculated using a geometrical method. If the ratio of the geometrical density of a specimen to the theoretical density of ZrC (see also section 2.1.1), namely, the relative density, was more than 90%, the Archimedes method was also applied to reexamine the reliability of geometrical relative density. The true axial shrinkage was employed to evaluate the densification kinetics of a specimen with respect to the processing time by assigning a constant radius to the specimen during the SPS treatment.

ZrC pellets with high relative densities were produced by various SPS processes. All retrieved relative final densities are mapped with the processing parameters in Figure 2.4. The relative densities of specimens prepared at 1700 ℃ have been rescaled to be more visible. Such a temperature is also considered as the optimal processing temperature for the selected material as it always secures the achievement of more than 90% relative density. Relative densities from the comparative study between hot pressing (round marker) and control SPS (triangle marker) are also present, in which the hot pressing is shown to give much lower density level than SPS even though they were subjected to similar heating and loading profiles. The highest relative density was obtained from carrying out double-die SPS of ZrC at 1600 ℃ under a pressure of 180 MPa (square marker). The influence of the pressure on the densification level is therefore indicated.

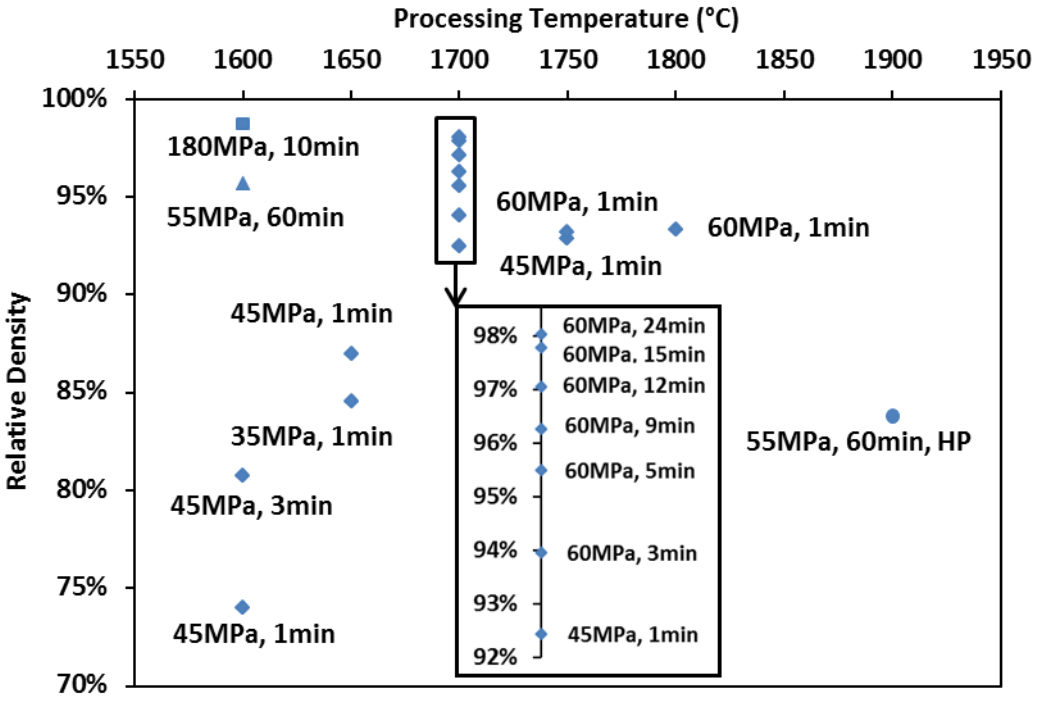

Figure 2.4 Map of relative densities for ZrC specimens prepared under various processing conditions.

Table 2.2 selectively listed the processing details and results from the conducted experimental runs. One can see that the final densities measured by the geometrical method are comparable to those evaluated by the Archimedes method, evidencing the reliability of the obtained data. SPS runs were successfully conducted to consolidate porous ZrC into high density levels and any enhancement in any of the processing parameters could lead to an increase in the product's final density. The influences of SPS processing temperature on the final density can be seen by taking Experiments 1 - 4 into consideration. An increase of peak processing temperature directly resulted in a rise of final relative density when same pressure and holding time were given. Experiments 5 and 6 were correlated to the pressure effects, the double-

die SPS retrieved higher final relative density even despite the fact that it was conducted at lower processing temperature with shorter holding time compared to the regular single-die SPS. The control SPS results are also included in Table 2.2 in comparison to the hot pressing ones (Experiments 7 and 8). A nearly 12% drop of relative density was seen in the hot-pressed specimen due to the lack of electric current assistance.

Table 2.2 Relative densities of sintered specimens

Exp. #	**Tooling Setup**	**Temperature (℃)**	**Pressure (*MPa*)**	**Holding (*Min*)**	**Relative Density**	
					Archimedes	**Geometry**
1	Single	1650	45	1	N.A	86.89%
2	Single	1700	45	1	92.56%	92.43%
3	Single	1750	45	1	93.04%	92.79%
4	Single	1800	60	1	93.47%	93.53%
5	Single	1700	60	24	97.91%	98.02%
6	Double	1600	180	10	98.77%	98.72%
7	Control SPS	1600	55	60	95.99%	95.71%
8	Hot pressing	1900	55	60	N.A	83.81%

Densification kinetics of ZrC processed at 1700 ℃ under SPS conditions is plotted in Figure 2.5 with temperature presenting as the secondary axis. A constant pressure of 60 MPa was applied from the very beginning. One can see that the fast densification started as processing temperature went over 1500 ℃. Beyond this point, the specimen's densification consistently intensified as temperature ramped up to the target level. During the isothermal dwelling at 1700 ℃, the densification slowed down

and evolved into a plateau around the middle of the holding stage, which indicates the importance of holding time for the densification intensity has been saturated at the selected temperature level.

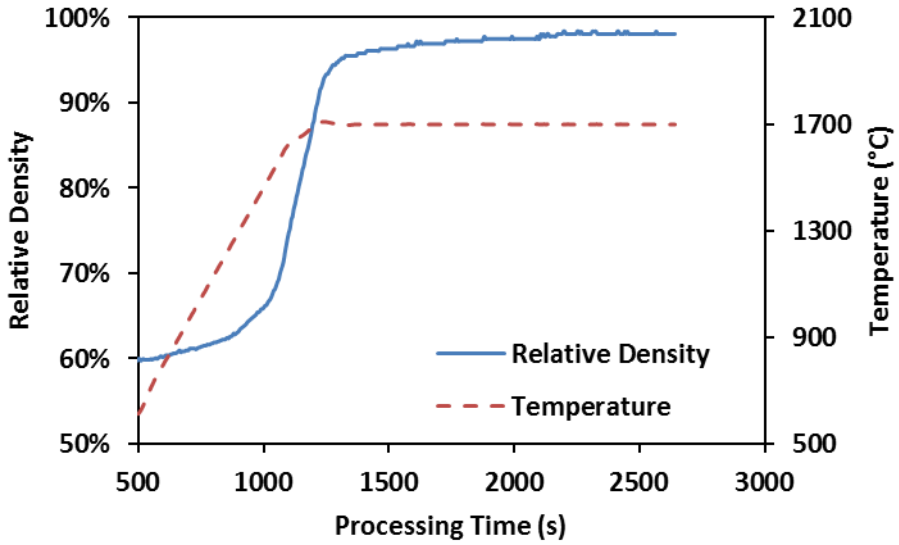

Figure 2.5 Relative density and temperature evolutions *vs.* processing time: single-die SPS of ZrC at 1700 ℃ under 60 MPa.

Densification kinetics of double-die SPS of ZrC is given in Figure 2.6 with applied pressure presenting as the secondary axis. The pressure profile utilized in double-die SPS differs from the one employed in regular single-die SPS. It was first kept at the minimum level (~80 MPa) and then rapidly increased to 180 MPa in about 2 minutes before the start of isothermal dwelling at 1600 ℃. Compared to the densification of ZrC under single-die SPS process (see also Figure 2.5), double-die SPS also introduced fast densification as a result of pressure intensification. However, the magnitude of the applied pressure appeared to influence the densification behavior in the later sintering stages. One can see that the relative density of double-die SPS-

processed specimen keeps increasing during the holding and the plateau stage only can be observed near the very end of the densification curve.

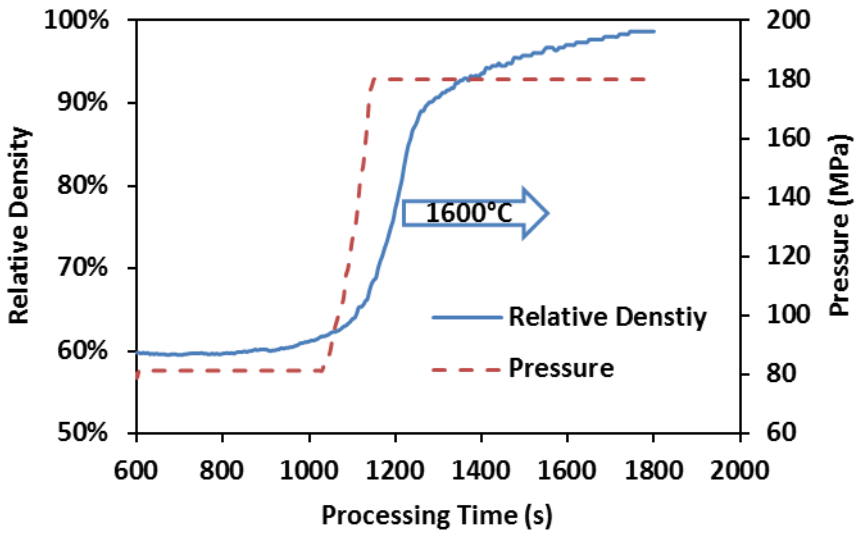

Figure 2.6 Relative density and pressure evolutions *vs.* processing time: Double-die SPS of ZrC at 1600 ℃ under 180 MPa.

Densification kinetics of ZrC under control SPS and hot pressing conditions are compared in Figure 2.7 with the arrows indicating the onset of the isothermal dwelling. The densification curve of the control SPS appears to be shorter than that of hot pressing, which can be attributed to actual processing time: i) the SPS run was conducted with a heating rate by analogy to the one used in hot pressing but to a lower peak temperature (1600 ℃) than utilized hot pressing (1900 ℃); ii) the heating rate from 1800 ℃ to 1900 ℃ was set to 2 ℃/min in the hot pressing run. In the control SPS runs, fast densification has already started before the maximum processing temperature has arrived. While in the hot pressing, it is hard to identify fast densification period even till the end of the entire process. In terms of the sintering

stages, the hot pressing of ZrC ended up with an 84% relative density corresponding to the intermediate sintering stage, while the control SPS of ZrC has evolved into the final sintering stage with 95% relative density being achieved.

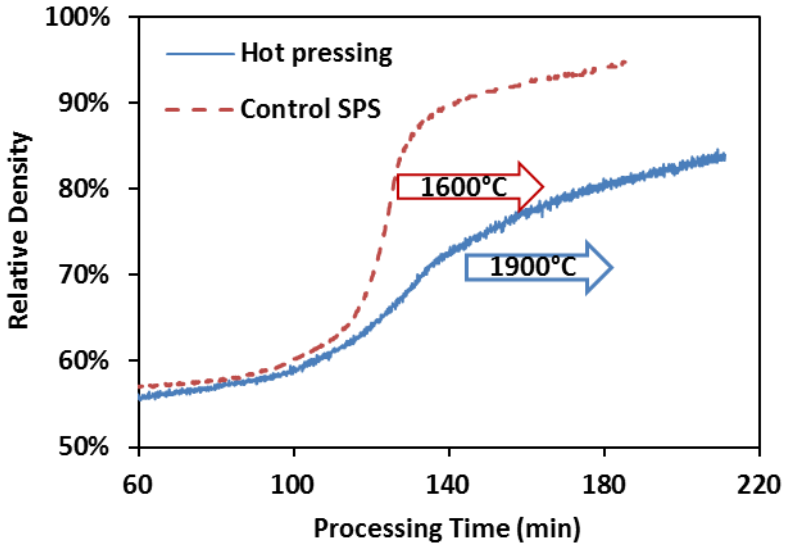

Figure 2.7 Hot pressing *vs.* control SPS of ZrC: densification kinetics under 55 MPa.

2.2 Microstructures of SPS-processed ZrC Specimens

At least two specimens were produced for every individual set of processing parameters. One specimen was prepared for characterizing the microstructural properties while the other one was used to test the mechanical properties.

For microstructural analyses, a specimen was evenly cut through the center by a high precision diamond saw (IsoMet 1000, Buehler, Lake Bluff, IL, USA). The two halves of a specimen were hot mounted together in Bakelite powder with their cross-sectional surfaces facing out to allow them being polished simultaneously on an automatic grinding machine (Tegrapol-11, Struers Inc., Cleveland, OH, USA).

Diamond polishing suspension (DPS-3, Struers Inc., Cleveland, OH, USA) was used in the final step of polishing to refine the surface metallography.

After cleaning and drying, the well-polished samples were etched for 3 min using HF:HNO_3:H_2O solution in a volumetric ratio of 1:1:3 in order to have a better relief of their grain geometries. The microstructures of the cross-sections were examined under SEM and the obtained micrographs were analyzed by an image software (ImageJ 1.50g, NIH Image, Bethesda, Maryland, USA) to calculate specimen's average grain size based on the mean linear intercept method with a correction factor of 1.5 [19].

The role of electric current in the hot consolidation of ZrC powders was studied by comparing the microstructures of ZrC specimens obtained from hot pressing to those retrieved from the control SPS. As shown in Figure 2.8, the hot-pressed specimen (Figure 2.8 a) possesses a porous structure with visible inter-particle contacts and insignificant grain coarsening phenomena due to the lack of electric current. However, under the same magnification, the specimen processed with the assistance of electric current (the control SPS) shows quite different microstructures. A much more consolidated morphology is present with clearly exhibiting large grains and distinctly displaying isolated individual pores in the matrix (Figure 2.8 b). The contrast between grains indicates the grain orientations.

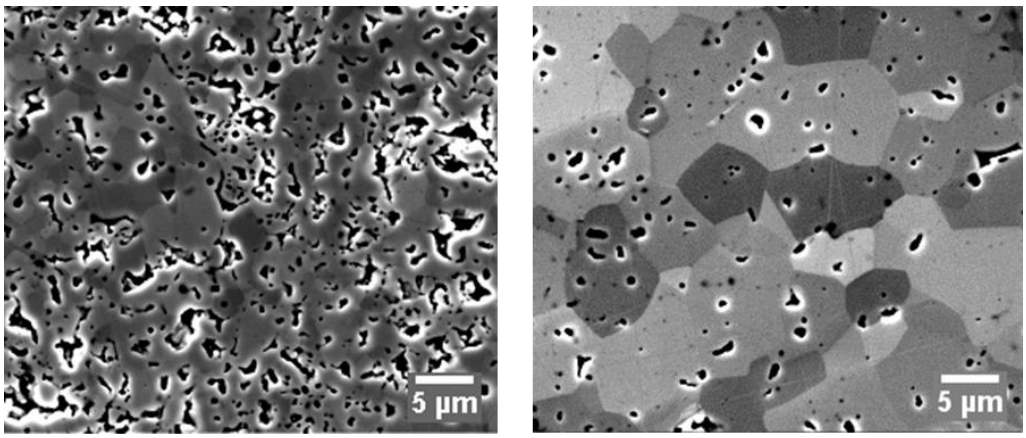

Figure 2.8 Microstructures of ZrC processed by (a) Hot pressing at 1900 ℃; (b) Control SPS at 1600 ℃; under 55 MPa and 60 min holding.

SEM images of specimens prepared at SPS temperatures of 1700 ℃ and 1800 ℃ are shown in Figure 2.9. Even despite the similar final relative density level (see also Table 2.2), it is easy to see that the grain size has been significantly augmented as a result of increasing SPS temperature. It shows that the increase of processing temperature affects grain growth more intensively than densification in the high relative density regime (> 90%). In addition, the pore morphology also evolves with the high temperature introduced grain growth. Most of the pores in the specimen processed at 1800 ℃ appear to be the spherical shape (Figure 2.9 b) while the one prepared at 1700 ℃ possesses lots of irregular shape pores (Figure 2.9 a).

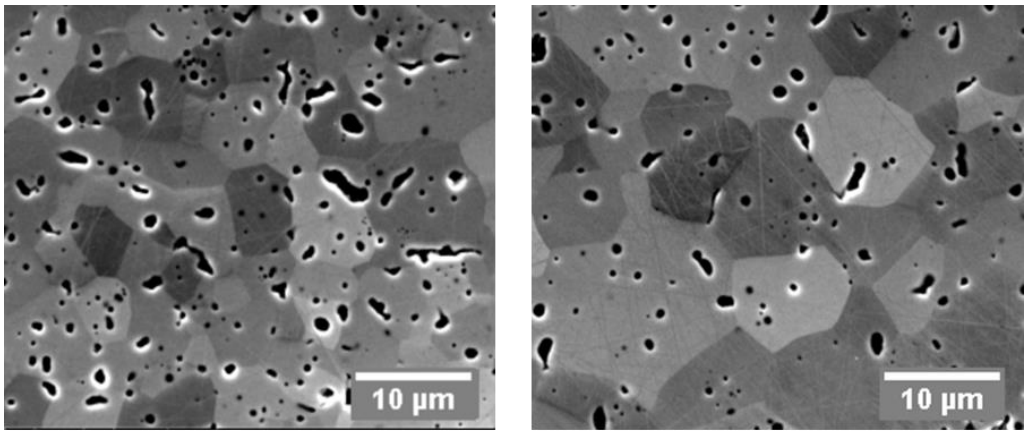

Figure 2.9 Microstructures of ZrC processed by SPS: (a) 1700 ℃, 45 MPa and 1 min holding; (b) 1800 ℃, 60 MPa and 1 min holding.

The microstructure of ZrC specimen produced by double-die SPS setup is present in Figure 2.10 a. The grains in the double-die SPS-processed specimen appear to be comparable or even larger than those in the single-die SPS-treated one (Figure 2.10 b), though the double-die SPS was conducted at a lower processing temperature (see also Table 2.2). This abnormal grain growth can be attributed to the extra thermal non-uniformity induced by the double-die setup. In such a system, on the one hand, reduced contact area between large and small punches can cause the occurrence of local overheating, as what has been reported in the past [128]. On the other hand, the insert of small die and punches can introduce extra contact resistance to the entire system where additional temperature gradient could be developed [129]. A detailed clarification on this fact will be conducted in CHAPTER 3.

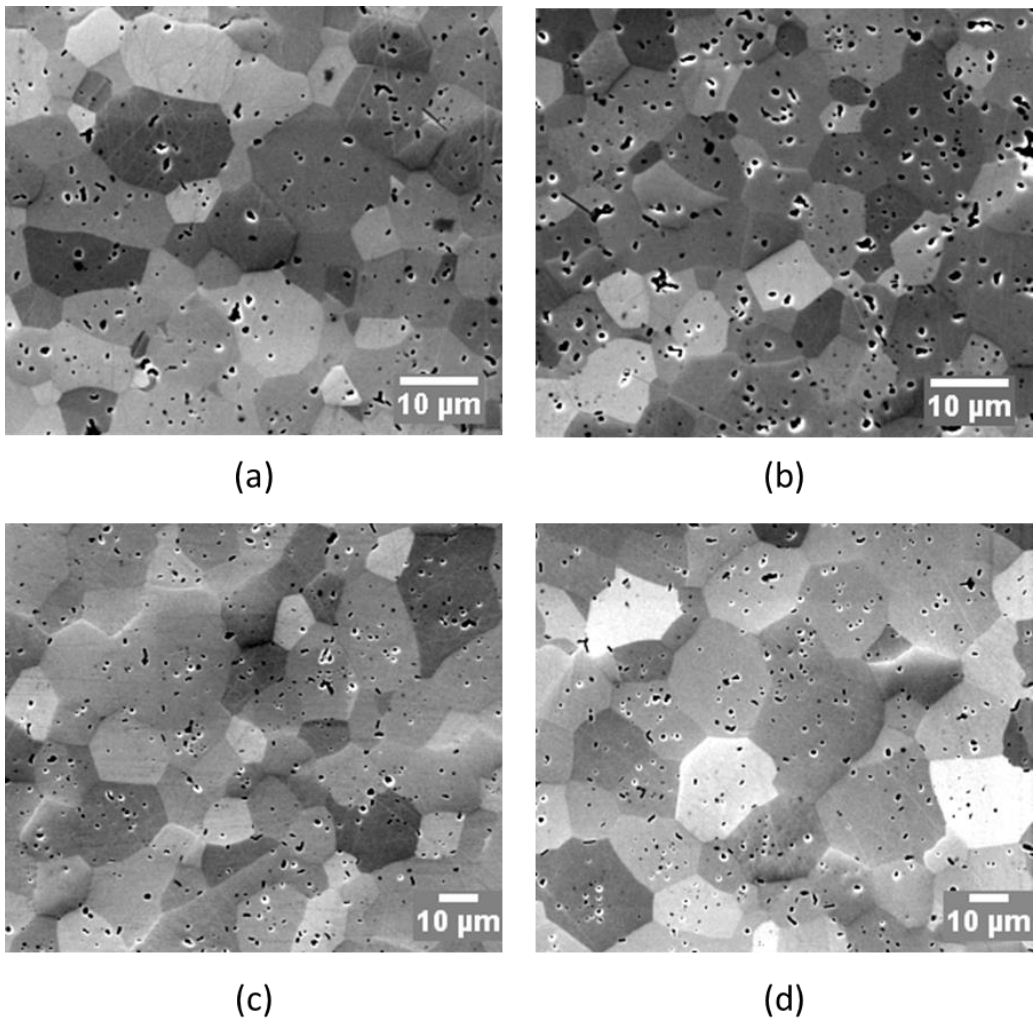

Figure 2.10 SEM images of SPS-processed specimens: (a) Double-die SPS at 1600 ℃; 180 MPa and10 min holding (b) – (d) Single-die SPS at 1700 ℃ under 60 MPa with holding time of 9, 15 and 24 min, respectively.

Figure 2.10 b – d demonstrate the microstructures of specimens SPS-processed at 1700 ℃ with holding time of 9, 15 and 24 mins, from where a direct impression of how grains interact with inter-granular pores at the triple junctions can be obtained: the grain growth gradually contributes to the process of pore closure. It appears that the densification can benefit from the grain growth to a certain degree in the final

stage. However, this phenomenological observation could be complemented by nano- or atomic- scale analyses to reveal the actual mass transfer mechanism (motions of grains or dislocations). The existence of a small quantity of intra-granular pores in the microstructures of all specimens is possibly due to: i) internal pores from initial powder (see also Figure 2.1); ii) high temperature pore formation mechanisms proposed by Kelly and Graeve [130]. Note that different scales are used in these images to properly represent the microstructures. The contrast difference between grains seems becoming significant with increasing holding time suggesting that the grain growth was associated with the grain movements.

Average grain sizes and relative densities obtained from specimens produced by SPS process at 1700 ℃ are represented in Figure 2.11with holding time up to 1440 s (24 min). One can see that the increase of the relative densities is accompanied by the augmentation of the grain sizes. Nevertheless, the grain growth appears to be more significant compared to the density evolution. As shown in Figure 2.11, the specimens' relative densities range (from 92.3% to 98.1%) indicates the sintering of ZrC has evolved into the final stage when isothermal dwelling started at 1700 ℃. During this stage, when the saturation of temperature level on densification is shown, the processing temperatures still substantially facilitated the grain growth as holding time proceeds [131].

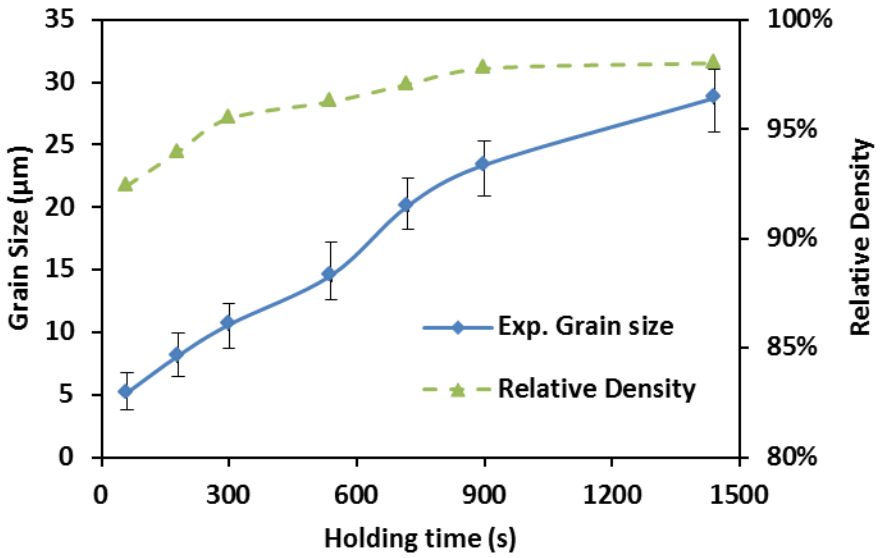

Figure 2.11 Grain size vs. relative density: SPS of ZrC at 1700 ℃ under 60 MPa.

2.3 Mechanical and Thermal Properties of SPS-processed ZrC Specimens

2.3.1 Transverse rupture strength and microhardness of the processed ZrC specimens

A particular transverse rupture strength test (TRS) procedure was previously designed for specimens with a cylindrical shape [96]. By gradually increasing the applied force through a tungsten carbide ball-shaped indenter onto a disk-shaped specimen, the rupture strength of the tested specimen is calculated as [132],

$$\sigma_{TRS} = \frac{F}{h^2}\left[(1+\nu)\left(0.485log\frac{a}{h}+0.52\right)+0.48\right]\ [MPa] \qquad (2.1)$$

where F is the applied force upon the occurrence of rupture (N), h the specimen thickness (mm), ν the Poisson's ratio, and a the effective specimen radius (mm). The loading rate was set as 0.001 in/sec (equivalent to 0.0254 mm/sec). During the rupture test, the applied force, F, was recorded by the material testing machine (Instron 5982,

Instron Inc., Norwood, MA, USA). The Poisson's ratio of partially dense ZrC specimen is relevant to its porosity, θ, as [133],

$$\nu = 2\nu_0\left(\frac{2-3\theta}{4-3\theta}\right) \tag{2.2}$$

where ν_0 is the theoretical Poisson's ratio of bulk ZrC from literature [123]. After the rupture test, large representative piece of a broken specimen was examined under SEM to obtain the microstructures of its fractural surface.

Transverse rupture test represents a specimen's mechanical properties at a macro level. Representative test results are summarized in Table 2.3 together with respective average grain sizes. Double die SPS specimens were not subjected to TRS test as they were too small to be mounted on the testing fixture.

Table 2.3 Transverse rupture strength and microhardness of sintered specimens

Tooling Setup	**Temperature (℃)**	**Pressure (*MPa*)**	**Holding (*Min*)**	**Relative Density**	**Ave. Grain Size (μm)**	**TRS (MPa)**	**H_V (GPa)**
Single	1700	60	24	98.02%	28.74	355.8	23.36
Single	1700	60	9	96.25%	14.57	302.2	22.35
Single	1700	60	5	95.49%	13.63	285.4	21.26
Single	1700	45	1	92.43%	7.93	234.6	17.54
Single	1650	35	1	84.47%	4.96	174.8	12.38
Single	1600	45	3	80.70%	2.58	150.4	8.91
Double	1800	180	10	98.72%	16.68	N.A	24.28

Maximum rupture strength is found to be around 370 MPa for the highest density specimens prepared at the maximum temperature of 1700 ℃. This value

corresponds to the same level of results using three-point bending tests [109] and four-point bending tests [104] on rectangular shape ZrC specimens, which evidences the reliability of this simplified testing method for cylindrical shape specimens.

These test results are plotted with respect to the relative densities in Figure 2.12 a. The rupture strength largely depends on the relative density. Higher strength is associated with higher density. The sharp increase of rupture strength is observed when the relative density goes over 95%, indicating the relative density played an important role in the TRS of sintered specimens.

SEM images of the fractural surface (Figure 2.12 b – g) illustrate how the cross-sectional morphology changes with increasing relative density. It is not able to identify grain structures in Figure 2.12 b – d due to low densities. The consolidated structures with visible grain geometries started emerging in Figure 2.12 e – g, which correspond to the specimens SPS-processed at 1700 ℃ with holding time spanning from 9 to 24 min. Both the processing temperature and the relative density level contribute to the grain growth. The images of the fractured surfaces also suggest the fracture mechanism belongs to the category of inter-granular fracture.

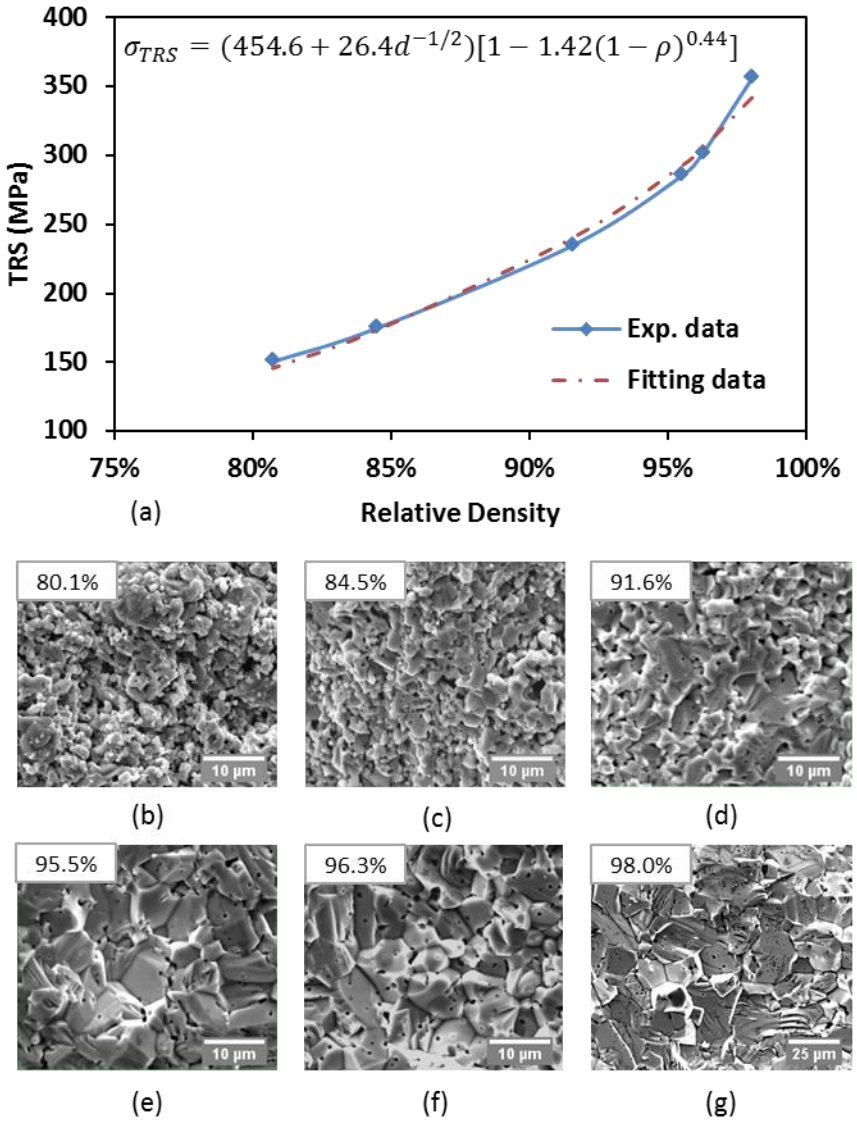

Figure 2.12 TRS test results and SEM images of fractural surfaces: (a) TRS *vs.* relative density, fitting equation with optimized coefficients is presented also; (b – g) SEM images of fractural surfaces of specimens with different relative densities.

Besides the relative density, average grain size was considered as another factor to the rupture strength. The yield stress of a specimen can be related to its average grain size using Hall-Petch relationship. After combining Hall-Petch

relationship and the strength - porosity dependence of a porous body [134], an expression for transverse rupture strength (MPa), σ_{TRS}, can be obtained taking into account the influence of the average grain size (μm), d, and relative density, ρ, as,

$$\sigma_{TRS} = \left(k_1 + k_2 d^{-\frac{1}{2}}\right)[1 - k_3(1-\rho)^a]\ [MPa] \tag{2.3}$$

where k_1, k_2, k_3 and a are parameters used to fit the experimental data. By substituting the average grain size and relative density from Table 2.3 into Equation (2.3), these fitting parameters are optimized to make a good reproduction of the experimental data, as illustrated in the top of Figure 2.12 a.

After the SEM examination, the hot mounted cross-sections were placed on the microhardness tester (M-400-H1, Leco Corp., St. Joseph, MI, USA) to test their Vickers hardness (H_v). Every polished surface was indented by a standard diamond indenter at the center, at the midpoint and at the edge, all under a pre-set force of 0.5 kgf.

Microhardness test indicates the specimen's mechanical properties at the microscale. The average Vickers hardness value at three examining points (center, middle and edge) of each tested specimen are also presented in Table 2.3 and plotted with respect to relative density in Figure 2.13. Results from double die SPS is included as a reference. Maximum hardness is found to be 24 GPa for the specimens prepared at the maximum processing temperature of 1600 ℃ using the double-die setup. The microhardness decreases as the relative density goes down. Although regular SPS at the maximum temperature of 1700 ℃ with 24 mins holding time gives a slightly

lower hardness value of 23 GPa, this value is still higher than the results from other studies conducted at the maximum SPS temperature of 2100 ℃ [109] and 1850 ℃ [135].

Analogous to the analysis of transverse rupture strength, the co-effect of average grain size and the relative density on the microhardness evolution are necessary to be correctly elucidated. A literature review revealed that Hall-Petch relationship was used to approximate grain size from microhardness of fully dense specimens prepare at different temperatures [136]. Also, porosity was related to the microhardness of ceramics sintered at the same temperature by assuming an exponential equation [137, 138]. Two separate aspects are combined in this study to form a possible presentation of microhardness (GPa), H_v, dependence on average size (μm), d, and relative density, ρ, as shown below,

$$H_V = \left(k_4 + k_5 d^{-\frac{1}{2}}\right) exp[b(1-\rho)]\,[GPa] \tag{2.4}$$

where k_4, k_5, and b are coefficients used to fit the experimental data. The optimization of these coefficients' values is conducted in the same way as in the rupture strength case. A parameterized Equation (2.4) is then obtained, as presented in Figure 2.13, providing a good agreement with the experimental results. The relative density seems to be a dominant factor for the microhardness evolution (not linear, but exponential) as the obtained coefficient of the grain size ($k_5 = 0.03$) is insignificant for this specific material.

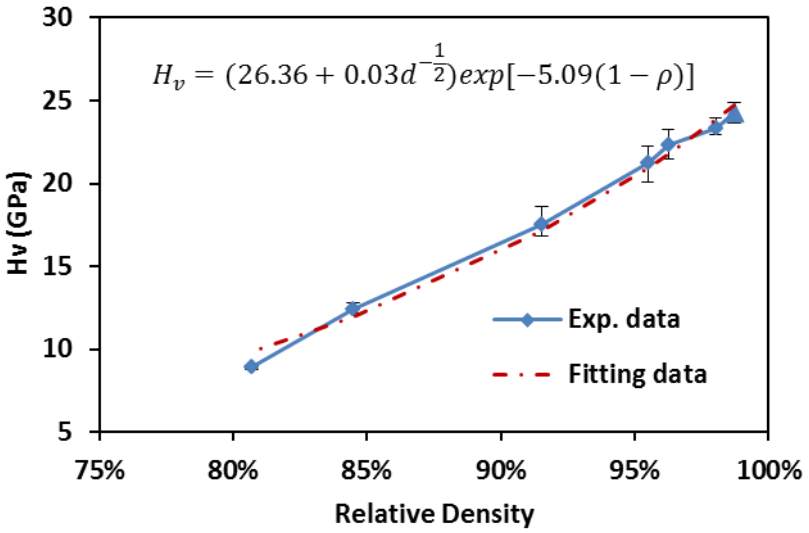

Figure 2.13 Microhardness *vs.* relative density. Fitting equation with coefficients is present too.

Taylor series expansion can be used to explain why the dependence of the microhardness on the relative density behaviors is exponential but appears to be linear. The exponential part of Equation (2.4) is expanded at $\rho = 1$, as follow,

$$exp[-5.09(1-\rho)] = 1 + 5.09(\rho - 1) + 12.95(\rho - 1)^2 + O((\rho - 1)^3)] \quad (2.5)$$

where the series term $(\rho - 1)$ ranges from -0.2 to 0 according to relative density values in Table 2.3, which makes the high order terms (power > 1) on the right-hand side almost negligible. Therefore the microhardness – relative density plot seems to be nearly linear but actually indicates an exponential relation.

2.3.2 Heat capacity and thermal conductivity of the processed ZrC specimens

A series of SPS processed specimens with relative densities ranging from 73.9% – 93.3% were further ground to 6 mm diameter by 1 mm thickness disks for thermal property tests. The heat capacity measurements were conducted under constant pressure using the differential scanning calorimeter (DSC 404 F1 Pegasus, Netzsch Co., Selb, Germany) along with the corresponding laser flash apparatus (LFA 427, Netzsch Co., Selb, Germany). The thermal diffusivity was determined by measuring the temperature change on the upper surface of the sample caused by a pulsed laser flash acting on its lower surface. Then, the thermal conductivity was considered to be the product of the sample's heat capacity, density, and its thermal diffusivity calculated by the laser flash apparatus [139]. All tests were performed at every 100 ℃ interval from room temperature to 1100 ℃ in an argon atmosphere.

The heat capacity of the specimens processed under various SPS conditions increases with elevating temperature as well as with raising the relative density (see Figure 2.14). Heat capacity first rises rapidly from room temperature to 300 ℃, and then it grows slowly until 1100 ℃. According to Ref. [140], the Debye temperature of stoichiometric ZrC is between 500 and 600 K (200 ~ 300 ℃), suggesting that the observation from the present study is in accordance with the reported data, as the heat capacity of carbide at low temperatures depends on its Debye temperature. Additionally, for a given volume, a specimen with higher relative density possesses more thermal mass. Therefore, more heat is required for a degree of temperature rise. Heat capacities of fully-dense ZrC were extrapolated from the measurements of

partially-dense specimens and compared with those calculated by Turchanin *et al*. using both Debye and Einstein equations [141] in the same graph. It shows that the highest heat capacity obtained from this study is very close to the one reported in the past while the extrapolation is more accurate as the temperature goes over 200 ℃.

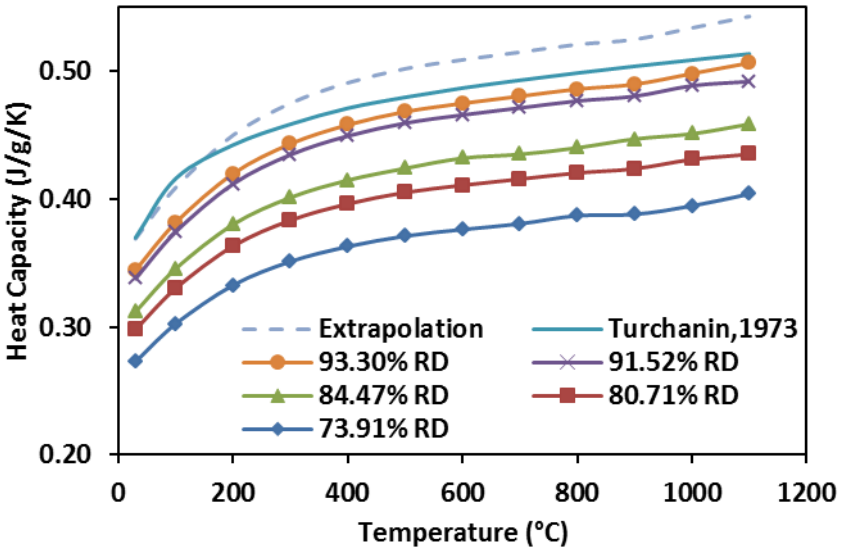

Figure 2.14 Heat capacities of SPS-processed specimens as a function of temperature.

As shown in Figure 2.15, the thermal conductivities of SPS-processed specimens rise with increasing temperature in the tested temperature range. This observation indicates quite unique ZrC properties compared to many other ceramic materials and it has been primarily attributed to the contributions of conduction electron bands and high phonon conductivity in ceramics materials [99]. Additionally, the thermal conductivity is shown to increase with enhancing the relative density because higher relative density is associated with the presence of fewer pores, hence more thermal pathways are present in the processed specimen. Thermal conductivities of the hot-pressed ZrC with very similar relative density (~93.3%) obtained by Taylor

were considered to be the highest results that have been reported in the past [142]. These data have been included for comparison in Figure 2.15 (scatter diamond markers, no data reported for temperature below 600 ℃). It appears that the measured thermal conductivities from the SPS-processed specimens are higher than those from the hot-pressed ones. Although the method of characterization between the present study and Ref. [142] is very different, the obtained evolutions of thermal conductivities are consistent and the flash method appears to be able to retrieve them at lower temperatures in a shorter time.

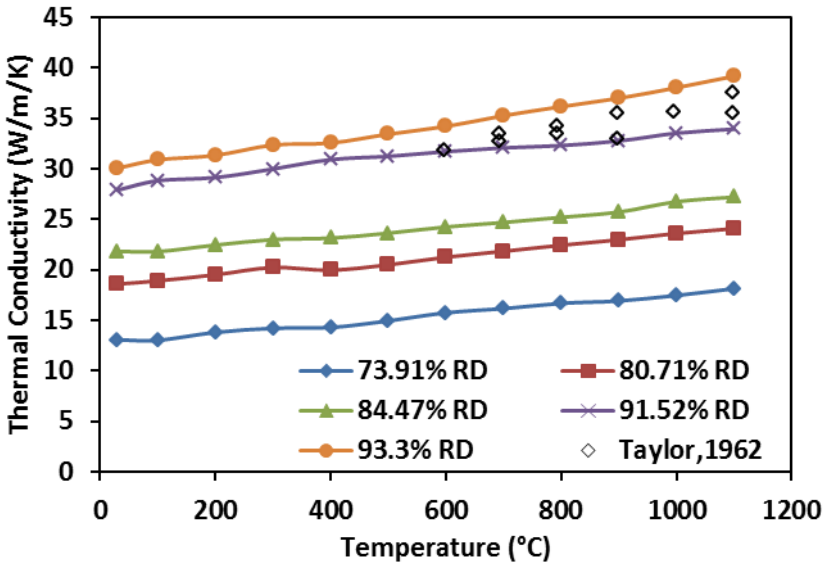

Figure 2.15 Thermal conductivities of SPS-processed specimens as a function of temperature.

SPS-processed specimens exhibited excellent heat capacities and thermal conductivities compared to those reported in the past. The improvements of the thermal properties are most likely due to the reduction of impurities during the SPS process. Impurities are easy to be introduced into powders during manufacturing

processes since powders have large surface area and high surface energy. The impurities or secondary atoms usually occupy lattice vacancies or present as interstitials which act as strong scattering centers for phonons and electrons. These impurities are hard to remove during conventional sintering processes. Therefore, both thermal and electrical properties of the sintered product can be negatively influenced. The SPS process provides high electric current enabling the generation of micro-discharges along powder surfaces to remove impurities [17, 143] and, in turn, to improve the above-mentioned properties of the final products.

2.4 Densification in Spark Plasma Sintering of ZrC

The conducted literature survey has shown that the power-law creep had been considered to be the dominant mechanism controlling the mass transport in crystalline materials under thermal and mechanical effects. A generally accepted model that represents the creep rate, $\dot{\varepsilon}\,(1/s)$, induced by an applied pressure, $\sigma\,(Pa)$, at a temperature, $T(K)$, can be expressed as the follows [144, 145],

$$\dot{\varepsilon} = \frac{D_0 \mu b_0}{kT}\ exp\left(-\frac{Q}{RT}\right)\left(\frac{\sigma}{\mu}\right)^n \tag{2.6}$$

where D_0 is the diffusivity, (cm^2/s), μ the shear modulus of elasticity, (Pa), b_0 the Burgers vector, Q the activation energy (kJ/mol) , n the stress exponent of the selected material. k is the Boltzmann's constant $(1.381 \times 10^{-23} J/K)$ and R is the gas constant $(8.314\ J/mol/K)$.

The major mechanisms of creep or mass transport, are defined by specifying the value of the stress exponent, *n*, in the following categories,

a. Diffusional creep, $n = 1$, models were developed by Herring [45] and Nabarro [46], also known as Nabarro-Herring Creep. The transport of matter is by diffusion through the grain lattice.

b. Grain boundary sliding, $n = 2$, suggested by Gifkins in 1976 [146]. Activation energy in this case is either equal to the activation energy for lattice diffusion or to the activation energy for grain boundary diffusion.

c. Dislocation glide-controlled creep, $n = 3$, proposed by Weertman in the explanation of prismatic glide creep under low stress [147], where the motion of dislocations is mainly impeded by the solute atoms.

d. Dislocation climb-controlled creep, $n = 4 - 5$, also reported by Weertman in early publications [148, 149]. The deformation is controlled by the climb of dislocations over physical obstacles in the glide/climb mechanism.

However, Equation (2.6) appears to be not able to sufficiently elucidate the creep of a powder bed subjected to thermal and mechanical treatments as both deformation and densification phenomena are involved in such a process. It is necessary to take into consideration the porosity dependence in describing the creep of porous materials. Particularly, the mechanisms which correspond to the mass transport driving densification of power materials during SPS process have attracted lots of

attentions recently. Different models have been developed to calculate the value of the stress exponent in order to determine the creep mechanism.

Gendre *et al.* [110] employed Ashby's model [56] to evaluate the stress exponent, *n*, and the apparent activation energy, *Q*, of synthesized zirconium oxynitride powder during SPS. The densification mechanism was proved to be largely dependent on the magnitude of applied pressure. Li *et al.* [76] developed a so-called multi-step pressure dilatometry (MSPD) approach to investigate the strain rate sensitivity exponent of copper powder under SPS conditions. This novel approach bypasses the influence of microstructure evolution by suddenly increasing the applied pressure to obtain short term stress-strain relationship. These two approaches, one takes into account the long-term effect, while the other considers instantaneous behavior. Both of them are efficient ways to retrieve the densification mechanisms.

By considering a porous body subjected to applied pressure at elevated temperature, Olevsky and co-workers [8, 9, 125, 150] have extended the idea in Equation (2.6) to an explicit constitutive equation for describing the stress-strain relationship in sintering of porous material, as,

$$\sigma_{ij} = A_{cr} W^{m-1} \left[\varphi \dot{\varepsilon}_{ij} + (\psi - \frac{1}{3}\varphi) \dot{e} \delta_{ij} \right] + P_L \delta_{ij} \tag{2.7}$$

where A_{cr} is creep coefficient with the following expression [151],

$$A_{cr} = A^{-m} T^{m} exp\left(\frac{mQ}{RT}\right) \tag{2.8}$$

where A is a reduced material parameter ($K/Pa^{\frac{1}{m}}/s$) in analogous to the combination of material's constants (D, μ, b and k) in Equation (2.6). m is the strain rate sensitivity exponent, $m = 1/n$. W is the equivalent strain rate,

$$W = \frac{1}{\sqrt{1-\theta}}\sqrt{\varphi\dot{\gamma}^2 + \psi\dot{e}^2} \tag{2.9}$$

with $\dot{\gamma}$ corresponding to the shape change rate, $\dot{e}$ represents the volume change rate. Since powder specimen in conventional SPS process is actually subjected to a pressing in a rigid die loading mode, $\dot{\gamma}$ and $\dot{e}$ are the same as those in Equation (1.5). φ and ψ are the normalized shear and bulk modulus, respectively. Both of them can be written in terms of porosity or void fraction of the porous body, θ, as [152],

$$\varphi = (1-\theta)^2 \tag{2.10}$$

$$\psi = \frac{2}{3}\frac{(1-\theta)^3}{\theta} \tag{2.11}$$

P_L is the effective sintering stress in Equation (2.7). In the case of pressure assisted sintering (e.g. SPS and hot pressing), it's negligible as it's of order of magnitude lower than the external pressure. δ_{ij} corresponds to Kronecker's delta ($\delta_{ij} = 0$ if $i = j, \delta_{ij} = 0$ if $i \neq j$).

According to mass conservation, the volume change rate can be also calculated through the evolution of the specimen's porosity as shown below:

$$\frac{\dot{\theta}}{1-\theta} = \dot{e} \tag{2.12}$$

After rewriting and Equation (2.7) in the cylindrical coordinate system, the applied pressure along the axial direction, σ_z , can be expressed as below [124],

$$\sigma_z = A_{cr} W^{m-1} \left[\varphi \dot{\varepsilon}_z + (\psi - \frac{1}{3}\varphi)\dot{e} \right] \tag{2.13}$$

and Equations (2.8) - (2.12) then can be substituted into the formulated Equation (2.13) to obtain below expression [153],

$$\dot{\theta} = \frac{d\theta}{dt} = -\frac{A}{T} exp\left(-\frac{Q}{RT}\right) (\sigma_z)^{\frac{1}{m}} \left(\frac{3\theta}{2}\right)^{\frac{m+1}{2m}} (1-\theta)^{\frac{m-3}{2m}} \tag{2.14}$$

this analytical equation describes how specimen's porosity changes with time at given sintering temperatures and pressures. It was utilized in this study to reveal the densification mechanism under SPS conditions through the determination of the creep strain rate sensitivity, *m*.

Equation (2.14) can be solved numerically with assigning proper coefficients (A, Q and m). Its reliability can be validated by comparing the numerical solution to the experimental data. With the elucidation of the strain rate sensitivity, *m*, or stress exponent, *n*, it is able to determine the densification mechanism of selected material under the SPS conditions. Nevertheless, in this equation, the absolute temperature, *T*, is correlated to the specimen's temperature but not the processing temperature. The SPS machine usually records the temperature at the outer die surface which is not an accurate reflection of specimen's real temperature as temperature gradients always

exist between the die and the specimen along the radial direction [154]. Therefore the machine logged temperature cannot be directly used in solving the analytical equation.

The thermal aspects in the SPS process need to be clarified in order to provide necessary data for analyzing the densification mechanism. Also, the thermal and electrical properties of tooling and specimen materials are of importance for study the temperature distribution in the employed SPS system during a coupled electro-thermal-mechanical process. Therefore detailed investigations are required for further process optimizations.

2.5 Chapter Conclusions

Commercial zirconium carbide powder has been successfully consolidated into high density specimens using different SPS setups. Relative densities of obtained specimens were mapped with processing temperature, applied pressure and holding time to elucidate the effects of these processing parameters on the densification level. The double-die SPS rendered a slightly higher final relative at relatively lower processing temperature but also showed larger grain growth compared to regular single-die SPS due to the localized high temperature and high pressure. Hot pressing of ZrC powder was not able to provide substantial shrinkage to the specimens due to the lack of electric current assistance.

Microstructural examination of the processed ZrC specimens indicated that the factors such as electric current, processing temperature and applied pressure significantly influenced the grain sizes and the pore morphologies of the obtained

specimens. The manipulation of temperature and pressure regimes have been proven to be able to control the densification and the grain growth in SPS of ZrC.

Transverse rupture strengths of the processed ZrC specimens were tested using a recently developed technique. Its reliability has been verified by comparing to the results from previously conducted studies. The rupture strength evolution is described as a co-effect of the average grain size and the relative density of the specimen. These two factors are also included in the evaluation of specimens' microhardness. The dependence of rupture strength, as well as that of microhardness on average grain size and relative density, have been quantified by approximating the proposed equations with the experimental curves.

Heat capacity and thermal conductivity of the SPS-processed ZrC were measured from room temperature to 1100 ℃ using DSC along with LFA. Specimen's thermal properties were found to increase either with increasing relative density or with raising temperature. The thermal properties obtained from the SPS-processed specimens were higher than the reported data retrieved from the hot-pressed ones at the similar relative density level, thereby indicating the impurity cleaning effect during the SPS process.

Major mechanisms of the mass transport in crystalline materials were discussed in terms of the value of the stress exponent in the power-law creep equation. The continuum theory of sintering was employed to derive the constitutive densification equation for powder-based material subjected regular SPS process. A differential equation describes how porosity changing with time was obtained. Solving

this equation can provide a way to determine the necessary densification parameters of the selected ZrC powder. However, the electric and thermal aspects regarding the utilized SPS system need to be clarified in advance. The SPS of ZrC is able to be optimized but more details are required from carrying out further investigations in the following chapters.

Chapter 2, in full, is a reprint of the material as it appears in "X. Wei, C. Back, O. Izhvanov, O. L. Khasanov, C. D. Haines and E. A. Olevsky, Spark plasma sintering of commercial zirconium carbide powders: densification behavior and mechanical properties, *Materials*, 8, 2015", and in "X. Wei, C. Back, O. Izhvanov, C. D. Haines and E. A. Olevsky, Zirconium carbide produced by spark plasma sintering and hot pressing: densification kinetics, grain growth, and thermal properties, *Materials*, 9, 2016". The dissertation author was the primary investigator and author of these papers.

CHAPTER 3 OPTIMIZATION OF THE SPARK PLASMA SINTERING: DENSIFICATION EFFICIENCY

Applying pressure during SPS process can directly facilitate the densification kinetics. In fact, the pressure also indirectly affects the densification behavior through varying the electric and thermal aspects in the SPS system. Therefore a quantitative investigation of these factors is necessary to be carried out prior to the loading mode-based optimization of the SPS densification efficiency. From this perspective, the pressure introduced contact resistance of an SPS system is first investigated with respect to the SPS temperature. Then the experimental results are utilized in finite element simulation to map the temperature distribution in the employed SPS system, where the electric current and the heat transfer phenomena are fully coupled. The obtained specimen temperature is substituted into Equation (2.14) to retrieve the creep coefficients of ZrC under SPS conditions. Upon the determination of material constants, the densification behavior of a porous body subjected to free up-setting loading mode is theoretically studied. Compared to pressing in a rigid die, free up-setting appears to achieve higher final relative density. Based on the modeling predictions, SPS-forging and hybrid SPS setups are implemented by manipulating loading modes in SPS of porous ZrC specimens.

3.1 Experimental Investigation of Contact Resistance in SPS Tooling Setup

The contact resistance of an SPS system is considered assisting the buildup of temperature non-uniformities besides the contribution from the inherent material

properties of tooling and specimen. The contact resistance, either thermal or electric, indeed, can be separated into two categories, the horizontal resistance and the vertical resistance. The former is due to the interfaces encountered in the axial direction between graphite disks (including punches and spacers), the latter counts for the radial clearances between punches and die. Contact resistance has been widely discussed in previous studies. Experimental as well as numerical approaches were performed to describe temperature gradient, current distribution and voltage variation phenomena during SPS process.

The issue of contact resistance has been taken into consideration in finite element simulation with coupling several physics phenomena. Zavaliangos *et al*. [155] evidenced how the contact resistance affecting the temperature difference between the specimen and the die surface through finite element modeling. Both electric and thermal contact resistances were inserted between tooling components in the horizontal and vertical directions. The authors stated that the existence of contact resistance leads to an unreliable reading of the effective specimen temperature from the pyrometer as it is referred to the die surface. An analogous approach has been followed by Wang *et al*. [156] and Olevsky *et al*. [151] when investigating temperature distribution in SPS setup.

Anselmi-Tamburini *et al*. [157] pointed out that the contact resistance can be safely neglected if the axial pressure is over 50 MPa in the experiment. The author also showed that at low temperatures (600 ℃) the temperature difference between outer surface and specimen introduced by contact resistance is negligible, while it

becomes significant at higher temperatures. Related simulation works conducted by Maizza *et al*. [158, 159] included contact resistance changes due to punch sliding and thermal expansion phenomena in the SPS, in which the contact area, temperature and densification level of the powder were all considered. In those studies, pressure was considered as a constant parameter.

Several more specific investigations have been attempted, mainly focused on the role of pressure in contact resistance evolution. Grasso *et al*. [160, 161] clarified how the influences of contact resistance decreased via increasing the pressure, which leads to the observation of a sample/outer die surface temperature difference decrease as the pressure is augmented. The observed phenomenon was attributed to the change of contact resistance due to the decrease of punch-die clearance, caused by the well-known Poisson deformation. The effect of punch-die clearance and the corresponding consequences in terms of temperature and voltage versus time profiles have been elaborated in the literature. The initial fit tightness appeared to affect the temperature gradients significantly in the tooling [162] and the behavior of contact resistance as a function of temperature and applied pressure was studied [163].

Specifically, the electric contact resistance was not quantitatively explained in the above-mentioned publications. It was either derived as a constant by fitting simulation results to the respective experimental ones or measured at room temperature without considering the temperature effects. Although one study provided the respective temperature dependence, the pressure factor was not included. A growing interest in understanding not only the specimen evolution during the SPS

processes, but the whole tooling setup conditions has led to analysis and experiments in absence of powder [164]. This is the approach we followed in this section in order to obtain results independent of the specific powder material, or in general focusing on the role of the tooling material in the densification mechanisms [165].

3.1.1 Experiment procedures

The Dr. Sinter SPSS-515 sintering apparatus (Fuji Electronic Industrial Co., Ltd., Kawasaki, Japan) was employed to conduct all experiments. The machine was operated under the manual temperature control mode (TCM), which is the most commonly utilized mode in regular SPS runs. A pulsed square wave direct current with on/off interval of 39.6 ms (12 on cycles) / 6.6 ms (2 off cycles) was generated by the selected working mode.

Graphite components used in the experiment (I-85 graphite, Electrodes Inc., Santa Fe Springs, CA) have an apparent density of 1.85g/cm^3. The flexural strength, the electric resistivity and the microhardness of the graphite are 97 MPa, 2.047 Ω/cm and 6.5 GPa, respectively. All these properties are measured at room temperature by the manufacturer. The outer and inner diameters of the die are 30 mm and 15.3 mm, respectively. The punch diameter is 15 mm with the purpose of creating a 0.15 mm punch-die clearance around the die wall. This clearance is supposed to be lined up by well-cut graphite paper (Fuji Electronic Industrial Co., Ltd., Kawasaki, Japan) before inserting the punches. Detailed dimensions of graphite components that used in this study are listed in Table 3.1.

Table 3.1 Dimensions of graphite components used in experiment

#	Name	Inner Dia. (*mm*)	Outer Dia. (*mm*)	Length (*mm*)
1	Punch	N.A	15	20
2	Punch	N.A	15	40
3	Die	15.3	30	30
4	Spacer	N.A	30	20
5	Dummy Die	15 (the ends)	30	40

To determine the horizontal contact resistance, two tooling configurations were put into consideration. One consists of two #1 punches with graphite paper being inserted in between, while the other employs a single #2 punch. The rest of graphite components are identical in order to eliminate possible discrepancies. The schematics of these two configurations are illustrated in Figure 3.1. The horizontal contact resistances involved in this setup are indicated as well.

The quantification of vertical contact resistance also hired two different configurations. As shown in Figure 3.2, #2 punch and #3 die represent the major part of the first configuration (Figure 3.2 a). Particularly, a bulky dummy graphite die (# 6) was used in the second one (Figure 3.2 b). To obtain local temperature readings at the punch-die interface, a 5 mm diameter borehole was drilled across the die wall and down to the punch-die interface. Also, a hole with the same size was drilled on the dummy die with a depth of 7.5 mm (where the actual punch-die interface locates).

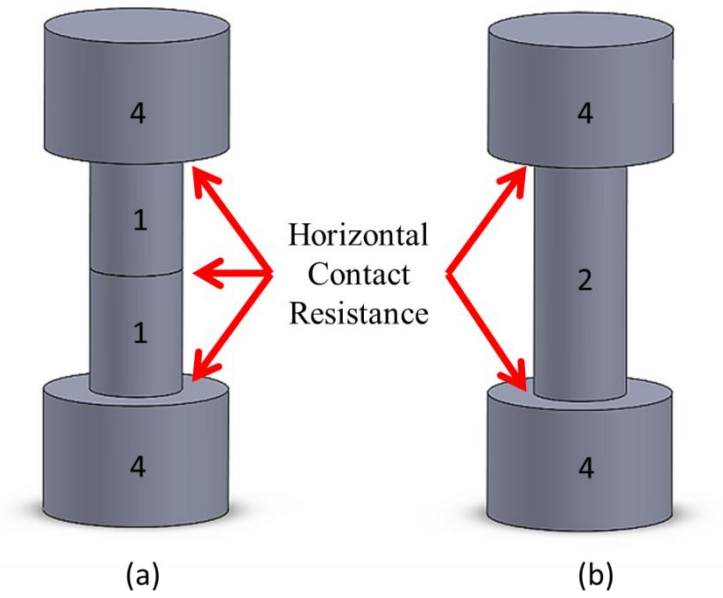

Figure 3.1 Schematics of tooling setup to analysis horizontal contact resistance: (a) Two-punch configuration; (b) Single punch configuration.

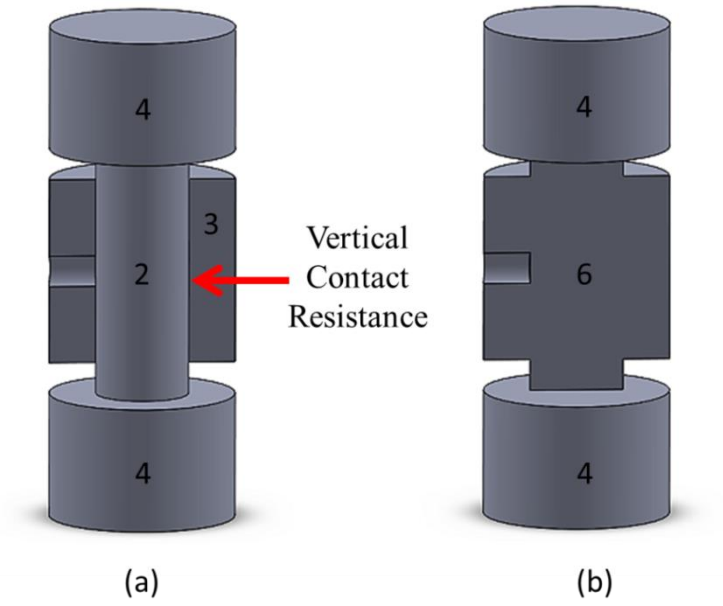

Figure 3.2 Schematics of tooling setup to analysis vertical contact resistance: (a) punch-die configuration; (b) Dummy die configuration.

Under the temperature control mode, the electric potential was applied at the ends of the spacers, providing a present temperature-time profile via Joule heating. The maximum processing temperature was set to 1600 ℃. The temperature was primarily monitored using an optical radiation pyrometer (IR-AHS2, CHINO Corp., Tokyo, Japan). During each SPS run, the pyrometer was always focusing on the middle point of the punch-die interface to record local temperature data. The pre-drilled 5 mm borehole on the die and dummy die ensures reliable temperature measurements. To minimize radiation heat loss, graphite felt was used to warp the tooling. Since the pyrometer is not able to detect a temperature which is lower than 580 ℃, experiments were performed with same graphite components but at 825 ℃. A K-type platinum thermal couple (NCF600, CHINO Corp., Tokyo, Japan) was then used to provide temperature readings as a supplement of those from pyrometer.

The uniaxial pressure was applied from the bottom side via the hydraulic loading unit of the machine. Four different pressures, 20, 30, 40 and 60 MPa were used in the experiments and they were applied at the beginning of the SPS process. All experiments were carried out under a vacuum of ~10 Pa. The heating rate was set at 100 ℃ /min. The holding time after reaching each temperature measuring point was set to 1 min. Every single experiment was repeated at least twice to ensure the reproducibility.

3.1.2 Evolution of electric contact resistance

3.1.2.1 Horizontal contact resistance

The overall electric resistance of the system can be calculated from the automatically logged voltage and current readings via Ohm's law. Figure 3.3 shows the system electric resistances of the two tooling configurations in Figure 3.1 under various applied pressures as processing temperature goes up to 1600 ℃. As one can see, despite the pressure differences, the overall resistance first displayed a rapid drop in the low processing temperature range (< 1000 ℃). Then the decreasing trend slowed down and evolved into a near plateau stage which indicates the temperature-induced resistance change of the interfacial contacts has reached an equilibrium with that of the graphite components.

Since the tooling configuration in Figure 3.1 a is exactly the same as that in Figure 3.1 b except the former has one more horizontal contact than the later, the resistance of this horizontal contact was calculated from the resistance difference between these two configurations. The obtained result, namely the horizontal contact resistance, was normalized with respect to the apparent horizontal contact area. The apparent contact area is used here because it was hard to identify the true contact area.

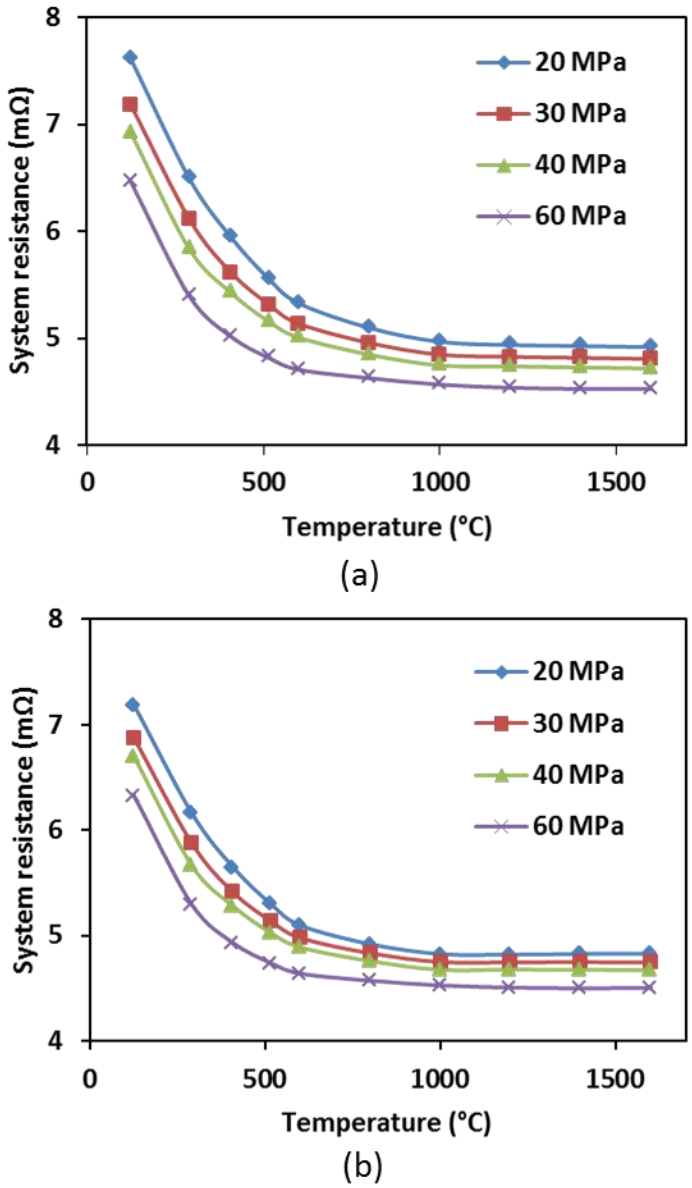

Figure 3.3 System electric resistance *vs.* temperature under 20, 30, 40 and 60 MPa: (a) Tooling configuration in Figure 3.1 a; (b) Tooling configuration in Figure 3.1 b.

All calculated horizontal contact results are presented in Figure 3.4, which shows how, even if the system resistance evolves into a plateau as temperature rises, if we subtract one set from another, minor discrepancies in the resulting horizontal

contact resistance values are distinguishable. Note that the selected y-axis range is different from the one employed in Figure 3.3.

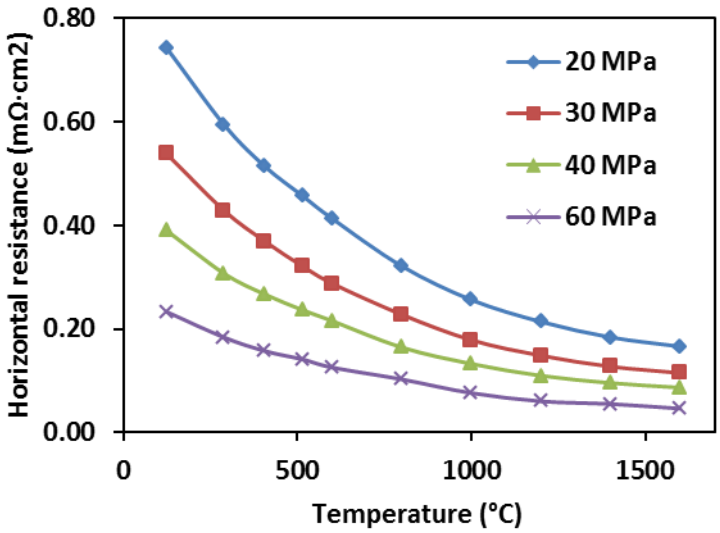

Figure 3.4 Horizontal contact resistance *vs.* temperature under 20, 30, 40, and 60 MPa.

The horizontal contact resistance, on the one hand, under the same pressure, decreases as the temperature goes up; on the other hand, at the same temperature, it reduces by increasing the pressure. This phenomenon can be explained by the non-linear creep of the graphite punches at the contact induced by thermal and mechanical effects. An imperfect contact interface forms when putting two punches end to end. At the beginning, two punch surfaces are poorly contacted because of geometrical irregularities and surface deposits, as described in Figure 3.5 a. In this case, less electric current can flow through this interface which results in a higher resistance. As gradually raising the temperature, the graphite starts creeping under the applied pressure so that the two surfaces begin interacting with each other as illustrated in Figure 3.5 b. The interface quality, even it is still imperfect, is being significantly

improved to let more current pass through, which represents a relatively lower contact resistance. The magnitude of applied pressure also contributes to the formation of high quality contact interface through either elastic or plastic deformation: higher pressure, better contact and lower resistance in turn.

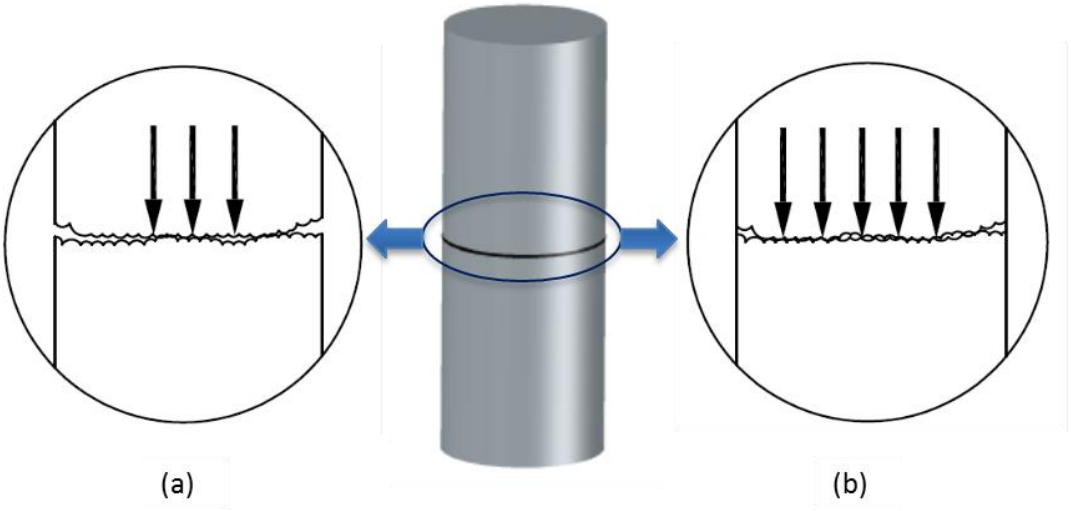

Figure 3.5 Schematic of imperfect horizontal contact interface between two punches: (a) Poor contact; (b) Good contact. Arrows indicate the direction and the amount of current pass through the interface.

The temperature and pressure co-effect on the contact quality is similar to the mechanism of diffusion bonding between materials [166]. Nevertheless, it is not able to completely eliminate surface asperities and create a perfect contact. The horizontal contact resistance always exists and its influence can only be attenuated with increasing temperature or pressure. Therefore the evolution curves of horizontal resistance are approaching each other, as shown in Figure 3.4, at higher temperatures.

To quantify this horizontal resistance, regression analysis of experimental data was applied. Both temperature and pressure factors were considered. By comparing the contact resistance under 20, 30, 40, and 60 MPa, the pressure factors were determined by calculating the average ratio between resistances with respect to two different applied pressures, as summarized in Table 3.2. Higher pressure appears to cause less significant changes in the horizontal contact resistance. This indicates that surface asperities can be offset by localized plastic deformation or creep, in accordance with the trends being described in the last paragraph. The pressure factors are then approximated by non-linear regression. By considering the resistance-temperature dependence via the same approach, the horizontal contact resistance, R_h, can be expressed by Equation (3.1), as,

Table 3.2 Pressure factors for horizontal contact resistance

Ratio	**20 MPa/ 20 MPa**	**30 MPa/ 20 MPa**	**40 MPa/ 20 MPa**	**60 MPa/ 20 MPa**
Factor	1	0.704	0.516	0.301

$$R_h(T,P) = (-0.24 \cdot \ln T + 1.94) \cdot (27.61 \cdot P^{-1.09})\ [m\Omega \cdot cm^2] \qquad (3.1)$$

where T is the processing temperature (℃) at the contact, P is the applied pressure (MPa). The first part of Equation (3.1) stands for the temperature dependence, while the second part includes the role of pressure. The regression is in good agreement with previously reported results by Zavaliangos *et al*. [155], and Vanmeensel *et al*. [163]. However, as mentioned before, coupled temperature and pressure dependence was not included in their works.

3.1.2.2 Vertical contact resistance

Even though the inserted graphite paper improves the conductance of the punch-die gap to a certain extent, the vertical contact resistance still exists because of the imperfect contacts. The resistance difference between the tooling configurations in Figure 3.2 a and b was considered as the contribution of the vertical contact resistance to the overall system resistance. Figure 3.6 presents the overall resistance of configurations in Figure 3.2 with respect to temperature under different applied pressures.

It is easy to see that the obtained overall system resistance decreases as temperature increases. The decreasing trend decelerates at higher temperatures. No plateau stage is observed in Figure 3.6 a, whereas Figure 3.6 b shows such a flat stage near the very end. The resistance of the graphite used in this study raises when the temperature goes up, as reported previously [128]. So the resistance of the punch-die contact is supposed to compensate the resistance increase of graphite components in order to make the decrease of the overall resistance.

The resistance differences between Figure 3.6 a and b, namely the vertical contact resistance are calculated and plotted in Figure 3.7. To make them consistent with horizontal ones in terms of the unit, all obtained results were multiplied by the apparent vertical contact area. The vertical contact resistance, like the horizontal one, is inversely proportional to temperature and pressure. In this case, such dependence appears to be linear to temperature, as Figure 3.7 illustrates.

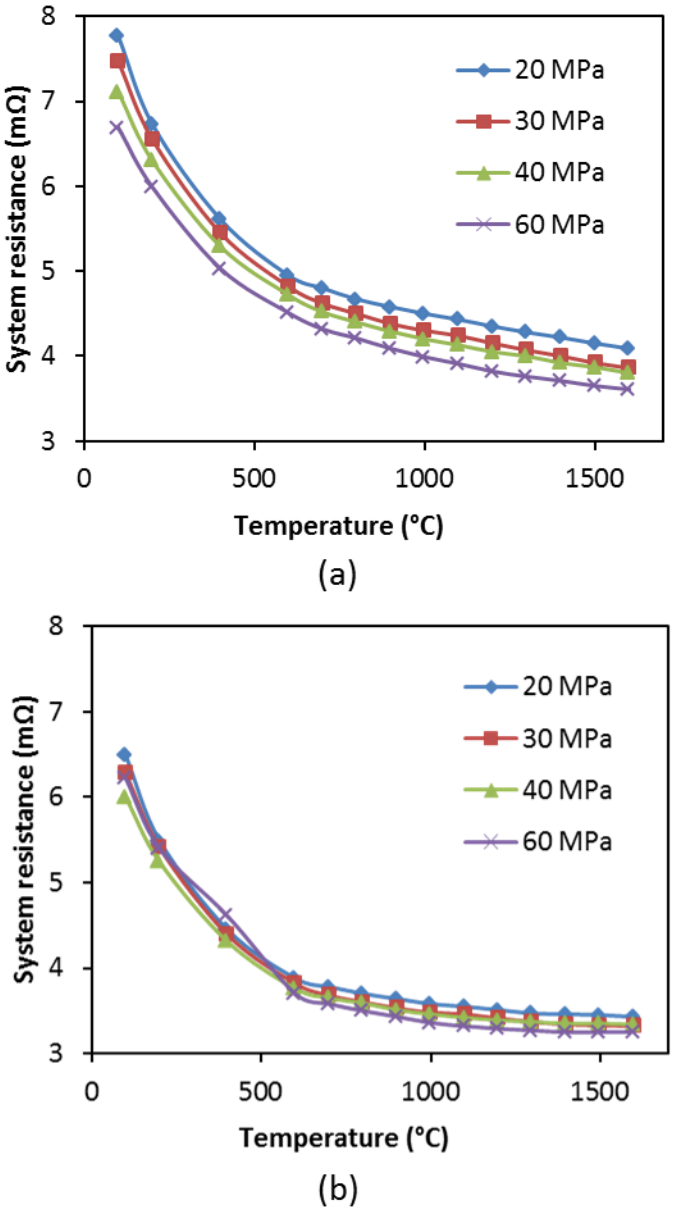

Figure 3.6 System electric resistance *vs.* temperature under 20, 30, 40 and 60 MPa: (a) Tooling configuration in Figure 3.2 a; (b) Tooling configuration in Figure 3.2 b.

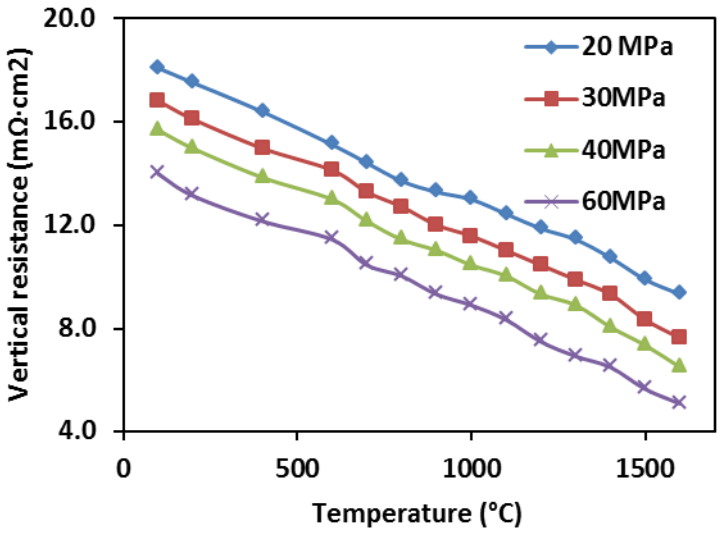

Figure 3.7 Vertical contact resistance *vs.* temperature under 20, 30, 40 and 60 MPa.

The explanation of this linear decreasing trend can be individuated in the two major phenomena underlying the vertical contact resistance reduction when temperature and pressure are raised. An increase in temperature causes a thermal expansion of the graphite tooling components, specifically of the die and the punch. An expansion of these two components leads to a reduction of the clearance responsible for the vertical resistance. The gradual approaching of the two contact surfaces translates in a higher number of the micro-peaks due to the surfaces' roughness touching each other, and therefore in an easier flow of current through the contact area. Being thermal expansion linear with temperature [167], the linear decrease of vertical resistance with augmenting temperature is explained.

Pressure plays a similar role, thanks to the Poisson expansion of the compressed punches. By applying an increasing axial load, the radial expansion of the punches is augmented, and considerations analogous to the ones concerning the

thermal contribution can be drawn. Since no permanent deformation was encountered in the punches after the experimental procedures, one could conclude that the Poisson deformation was purely linear elastic, therefore justifying the linear dependence of vertical contact resistance on the externally applied load.

The pressure factors are displayed in Table 3.3, in terms of the average ratio between resistances with respect to two different applied pressures. Then the regression of temperature and pressure dependences obtains the following expression for vertical contact resistance, R_v,

Table 3.3 Pressure factors for vertical contact resistance

Ratio	**20 MPa/ 20 MPa**	**30 MPa/ 20 MPa**	**40 MPa/ 20 MPa**	**60 MPa/ 20 MPa**
Factor	1	0.893	0.807	0.678

$$R_v(T,P) = (-0.0057 \cdot T + 18.59) \cdot (-0.0079 \cdot P + 1.14)\ [m\Omega \cdot cm^2] \quad (3.2)$$

The vertical contact resistance also consists of two parts: one states the temperature effect; the other describes the pressure impact. Both of them are linear relationships. Either thermal expansion coefficient or Poisson's ratio varies from one material to another, therefore it is hard to separate the vertical contact resistance from the properties of the employed graphite components in SPS tooling, while the horizontal contact resistance is somehow independent of the materials itself. Also, as a 0.15 mm gap is actually created between punches and die in the present investigation, even though it is filled up by conductive graphite paper, the experimentally obtained resistances for vertical contacts are higher than those results reported in some previous

studies [155, 157, 163] which considered a direct contact between punches and die or specimen and die.

3.2 Temperature Distribution in SPS of ZrC Powder

In this section, finite element simulation using COMSOL® Multiphysics software (COMSOL Inc., Burlington, MA, USA) is used to investigate the temperature evolution during the conventional SPS of ZrC. Electric current and consequent Joule heating phenomena are substantially coupled in the implementation of characterizing thermal aspects of employed SPS system. The obtained electric contact resistances are included and material properties are calibrated in the developed modeling framework.

3.2.1 Modeling of temperature distribution in SPS of ZrC

According to the Joule's law, the heat induced by the flow of electric current can be written as,

$$h = \vec{J} \cdot \vec{E} \tag{3.3}$$

where $\vec{J}$ denotes the current density (A/m^2) and it is expressed as: $\vec{J} = \lambda\vec{E}$ with $\vec{E}$ corresponding to the electric field intensity (V/m) and λ to the electric conductivity ($\Omega^{-1} \cdot m^{-1}$). Furthermore, the electric field intensity can be represented by the gradient of electric potential, V, as: $\vec{E} = -\nabla V$. Therefore,

$$h = \lambda|\nabla \mathrm{V}|^2 \tag{3.4}$$

The generated Joule heat dissipates in solids through heat conduction, with respect to time and space, as,

$$\rho_{eff} C_p \frac{\partial T}{\partial t} + \nabla \cdot \vec{q} = h \tag{3.5}$$

where ρ_{eff} is the effective density (kg/m^3), C_p is the heat capacity (*J/kg/K*), $\vec{q}$ is the heat flux vector defined as $\vec{q} = -k_T \nabla T$, with k_T representing the thermal conductivity (*W/m/K*).

Substituting Equation (3.3) into (3.5) to have the equation for a coupled Joule heating system,

$$\rho_{eff} C_p \frac{\partial T}{\partial t} - \nabla \cdot (k_T \nabla T) = \lambda (\nabla V)^2 \tag{3.6}$$

Thermal radiation equation is present in the system and it is given by,

$$q_r = \sigma_s \varepsilon (T_{em}^4 - T_{ab}^4) \tag{3.7}$$

where σ_s is the Stefan-Boltzmann constant ($5.670 \times 10^{-8} W/m^2 K^4$), ε is emissivity, T_{em} and T_{ab} are the temperature at the emitting and the absorbing surface, respectively.

The contact resistance, either electric or thermal, of the tooling setup is applied to manifest the temperature discontinuity. The current density induced by the electric contact impedance is formulated as follow,

$$\vec{n} \cdot \vec{J}_{ec} = \frac{1}{R_{ec}} (V_a - V_b) \tag{3.8}$$

where $\vec{n}$ is the normal to the contact surface, $\vec{J}_{ec}$ is the generate current density at the contacts (A/m^2), R_{ec} is the electric contact resistance $(\Omega \cdot m^2)$, in which the experimentally-derived formula will be plugged, V_a and V_b are the electric potential at any two contact surfaces.

The role of thermal contact resistance was not experimentally investigated in the present study as Yovanovich [168] has dedicated four decades of research to develop a comprehensive model for this particular phenomenon. Efforts were applied initially to analysis in the microelectronics field, and subsequently expanded to more general heat exchange issues. The COMSOL® software itself is endowed with a Cooper-Mikic-Yovanovich typology of boundary condition for thermal contact impedance in the heat transfer models. The form of the selected thermal equations is the following:

$$\vec{n} \cdot \vec{q}_{tc} = \frac{1}{R_{tc}} (T_a - T_b) \tag{3.9}$$

where $\vec{n}$ is the normal to the surface, $\vec{q}_{tc}$ is the generated heat flux at the contacts, T_a and T_b are the temperature at any two contact surfaces, R_{tc} is the thermal resistance of the gap $(K \cdot m^2/W)$ which has the dependence on the material's properties and the applied pressure as,

$$\frac{1}{R_{tc}} = 1.25 k_{tc} \frac{m_{asp}}{\sigma_{asp}} \left(\frac{p}{H_v}\right)^{0.95} \tag{3.10}$$

where k_{tc} is the thermal conductivity of the contact which actually refers to that of the graphite components, p the applied pressure, m_{asp} the surface asperities average slope,

selected as 0.4, σ_{asp} the surface asperity average height, 1 μm, and H_v the material's microhardness, set as 6.5 GPa (see also section 3.1.1).

Thermal and electric properties, including the temperature dependence, of the utilized graphite tooling, followed the expressions previously used by Olevsky *et al.* [151]. Heat capacity, thermal conductivity and electric conductivity of porous ZrC specimen during processing are given in Table 3.4 as functions of its porosity, θ, and temperature, *T (K)*. ZrC's thermal and electric properties were selected in accordance with literature data [99, 126].

Table 3.4 Properties of zirconium carbide used in simulations

Parameters	**Values**
Heat capacity, $\boldsymbol{C_p}$ (*J/kg/K*)	$(352.8 + 0.094T - 2.55 \times 10^3 T^{-2})(1-\theta)$
Thermal conductivity, $\boldsymbol{k_T}$ (*J/m/K*)	$(17.82 + 0.024T - 9.39 \times 10^{-6}T^2 + 1.68 \times 10^{-9}T^3)(1 - 0.5\theta - 1.5\theta^2)$
Electric conductivity, $\boldsymbol{S}$ (*S/m*)	$\frac{1}{39.3 \times 10^{-8} + 76.7 \times 10^{-11}T}\left(\frac{1-\theta}{1+2\theta}\right)$

Due to the geometric features of the tooling and the specimen used in the experiments, an axial-symmetric model was built in COMSOL® to investigate the temperature evolution in SPS of ZrC via finite element simulation. The major portion of the utilized model is shown in Figure 3.8 with specifying the dimensions of each component. During the simulation, the electric potential was introduced at the top electrode while the bottom one was grounded (Both are not included in Figure 3.8).

Equation (3.6) was used to couple electric current and heat conduction modules through all sub-domains. While Equation (3.8) and (3.9) were applied as supplements of Equation (3.6) only at the interface where two components are encountered. It was assumed that same electric and thermal resistances were used for punch/specimen and specimen/die contacts [163].

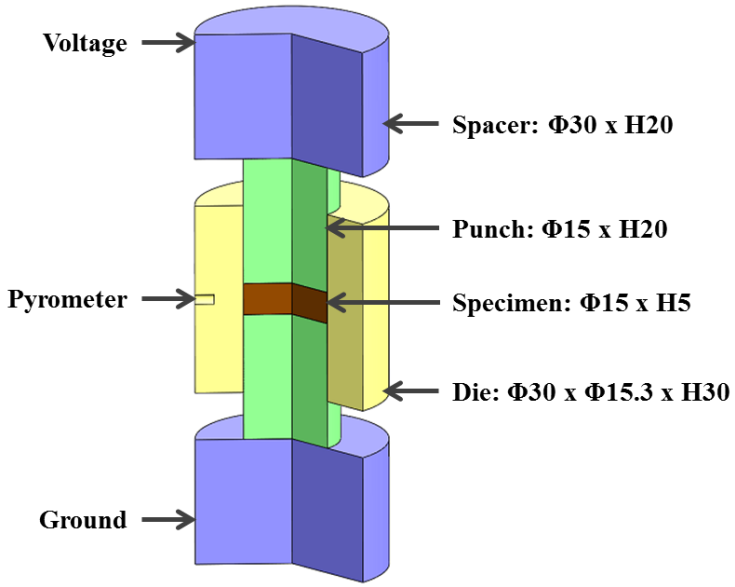

Figure 3.8 Geometric model for investigating temperature distribution in SPS of ZrC. Boundary conditions and tooling dimensions (unit: mm) are included as well.

The SPS machine logged voltage readings were converted to their root mean square values and interpolated with time to provide continuous inputs for the entire modeling process. The simulated temperature of the control point at which the temperature measuring pyrometer has been focused was compared to the one obtained from the experiment. These two sets of data have to be in good agreement with each other in order to confirm the reliability of the modeling results and retrieve the

specimen temperatures from the simulation. The radial temperature gradient was then calibrated by correlating the calculated specimen temperatures at the control point with the pyrometer temperatures measured at the same spot to allow a fair comparison of densification kinetics between SPS and hot pressing of ZrC.

The formulated modeling procedure guarantees the adherence of current simulations to actually SPS processes, and therefore the verification of the impact of the contact resistance. With regard to the finite element meshing, the relative simplicity of such models allowed the selection of a physics-defined, free-triangular mesh, with “extra fine” size, as the COMSOL® classification states, for a total of 1179 domain elements.

3.2.2 Modeling results

Since the pyrometer focused at the outer die surface to detect temperature during SPS experiments, the temperature was intended to be evaluated first at the same spot (where the "pyrometer" arrow points in Figure 3.8) in the simulations. Material properties were then slightly calibrated based on the comparison between simulating obtains to experimental data. Temperature values at the center where the ZrC specimen locates were extracted as well from the simulation, in which the volume average temperature was evaluated.

Simulated temperature values at the point of the pyrometer measurement (long-dash line) and the average temperatures in the volume of the specimen (dot-dash line) at the maximum processing temperature of 1750 ℃ are plotted together in Figure

3.9. The experimentally obtained temperature data was included as a reference (dashed line). The evolution of simulated temperatures at the pyrometer spot shows good agreement with that of the experimental readings. Acceptable discrepancies at low temperature range were most likely caused by the lagging of the utilized SPS machine as well as by the radiative heat loss during the rapid heating (100 ℃/min). However, the specimen's temperatures extracted from the simulation are way higher than those retrieved from the experiment and the gaps between these two sets of data keep growing as processing temperature rises.

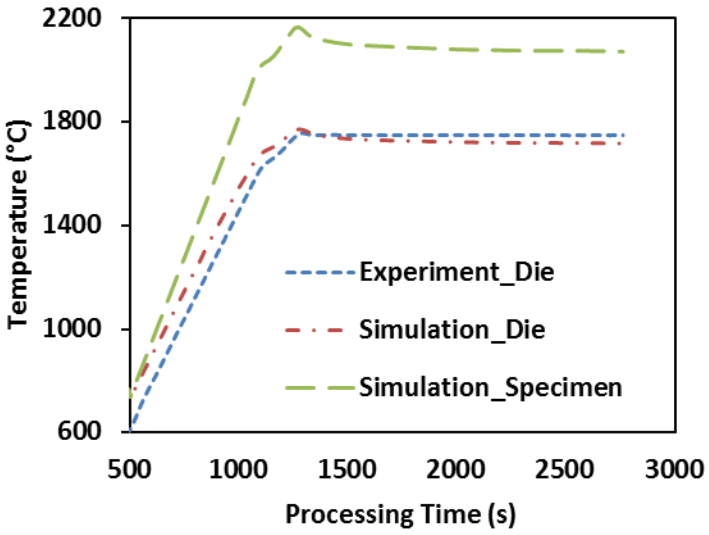

Figure 3.9 Temperature evolution in SPS of ZrC at the maximum processing temperature of 1750 ℃: simulation *vs.* experiment.

Figure 3.10 illustrates the temperature distribution obtained from conducting finite element simulation of SPS of ZrC at 1750 ℃ with a color bar indicating the temperature levels on the right. One can see that the temperature is non-uniformly distributed in the entire system and the temperature differentiation propagates along

the radial direction. This non-uniform temperature distribution in the tooling system is a common phenomenon in SPS process and should be carefully assessed [151, 169]. Meanwhile, the localized overheating occurs near the ends of punches due to the sudden increase of current density subjected to a reduced cross-sectional area [128].

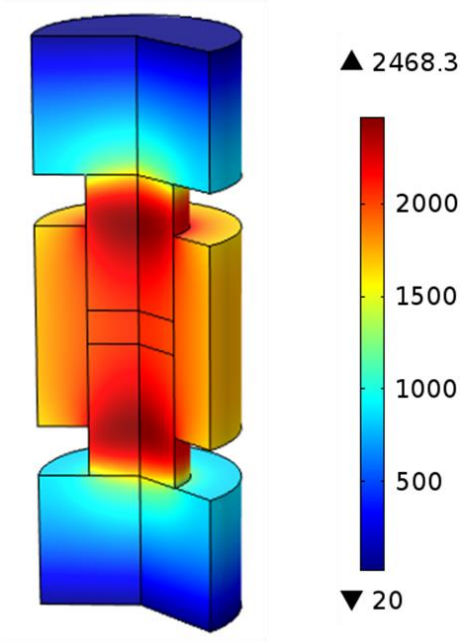

Figure 3.10 Simulation results: temperature distribution in the entire tooling setup during single die SPS of ZrC (unit: ℃).

Figure 3.10 also suggests that the contact resistance has contributed to the formation of the thermal non-uniformity as the thermal concentration at the contacts can be clearly seen from this graph. Also, the impact of the contact resistance on the evolution of specimen's temperature has been manifested via the simulation. Figure 3.11 shows the specimen's temperature evolution profiles for the resistive (blue) and the ideal (red) contact-free cases. When identical processing parameters are assigned,

the temperature rise in the ideal case is slightly higher than that of the resistive one during the early heating stage. Then it slows down and eventually falls below the other as temperature ramps up. A fixed temperature difference of ~100 ℃ appears after the maximum processing temperature is achieved. The introduction of electric contact resistance allows less current passing through the specimen and results in lower temperature at first but lately contributes to the overall thermal buildup through the Joule heating effect.

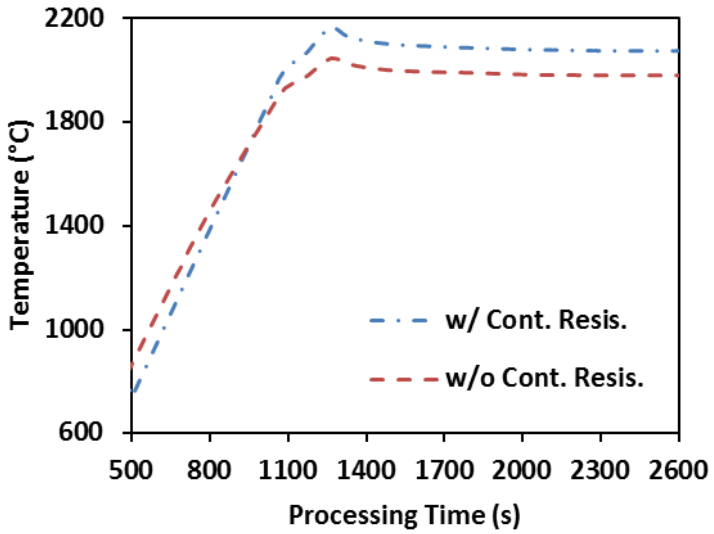

Figure 3.11 Simulation results: temperature evolution of ZrC specimen, with and without contact resistance cases.

The employed finite element model not only elucidated the electric and thermal aspects during SPS of ZrC but also provided a way to evaluate the specimen's real temperature. Moreover, it verified how the effects related to the contact resistance are of importance for the analysis of temperature evolution in typical SPS process. In the same manner, simulations were conducted to calculate specimens' average

temperatures based on other processing profiles used in CHAPTER 2. The obtained specimen's temperatures at the maximum processing temperature of 1800 ℃, 1750 ℃, 1700 ℃, 1650 ℃ and 1600 ℃ with the single-die setup as well as at 1600 ℃ with the double-die setup are summarized in Table 3.5. Temperature gradient along radial direction ($\nabla_r T$) is calculated as the temperature difference between the specimen and the die surface (pyrometer) divided by the effective thickness of the die wall which is 7.5 mm in single die setup and 11.5 mm in double die setup.

Table 3.5 Obtained specimens' average temperature (simulation-based)

Tooling Setup	**Processing/pyrometer Temperature (℃)**	**Ave. Specimen Temperature (℃)**	**$\nabla_r T$ (℃/*mm*)**
Single	1800	2135	43.5
Single	1750	2071	42.8
Single	1700	2013	41.7
Single	1650	1959	41.2
Single	1600	1906	40.8
Double	1600	2156	48.3

The calculated temperature gradient appears to increase with rising the processing temperature in single-die setups. Simulation work conducted by Antou *et al.* [123] without considering contact resistance retrieved similar thermal gradient *vs.* pyrometer temperature relationship, but the calculated thermal gradient in the referred study was way lower. After plotting the simulated specimen’s temperatures with respect to the pyrometer measured processing temperatures, as shown in Figure 3.12, a nearly linear relationship was obtained when processing temperature varies from

1600 ℃ to 1800 ℃. The trend line is similar to the one that has been attained by Antou *et al*. via finite element simulation [123], as well as by Kelly and Graeve through conducting SPS runs, to which both top and side pyrometers were attached [130]. The temperature experienced by a ZrC specimen subjected to different SPS processing temperatures therefore can be estimated via the developed modeling framework and subsequently utilized in the determination of governing mechanisms for densification and grain growth (section 3.3.1) in the SPS of ZrC powder.

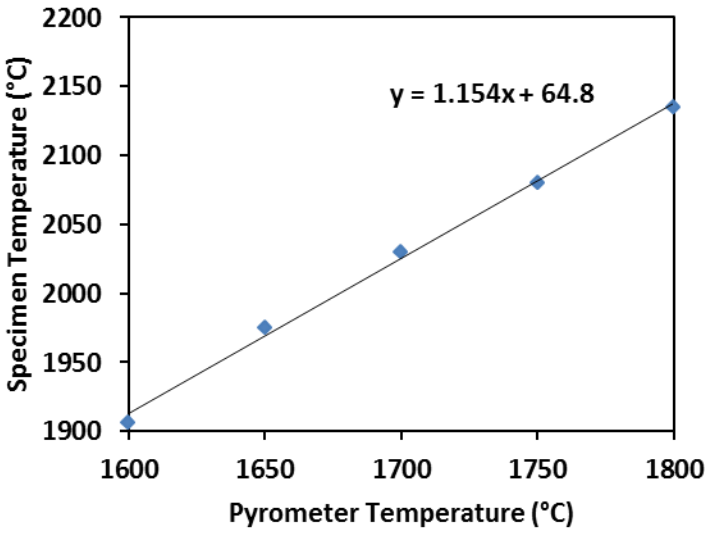

Figure 3.12 Specimen's temperature (simulation) *vs.* pyrometer detected maximum processing temperature (experiment).

In addition, the double-die SPS-processed specimen owns the highest average temperature and the largest thermal gradient compared to the single-die processed ones. The occurrence of local overheating mainly attributes to the reduced dimension of the specimen itself and the inserted small punch/die setup as described in Figure 2.3

(b). Since the electric conductivity of ZrC is of the order of magnitude higher than that of the surrounding graphite components, more current tend to go through the specimen therefore more heat is generated. Extra contacts are created by introducing small components into the system and those resistive interfaces also contribute to the formation of the temperature gradient between the specimen and the die surface.

Double die SPS actually gives a much higher temperature to the specimen than single die SPS. It explains why grain growth was overestimated when performing double die SPS of ZrC even at a relatively lower processing temperature in CHAPTER 2. It seems that the double die SPS can efficiently control the densification through manipulating temperature and pressure, but one has to sacrifice the effective size of the final specimen.

3.3 Power-law Creep of ZrC under Different Processing Conditions

The simulation results have elucidated the fundamental thermal aspects in the currently utilized SPS system. Upon the revelation of the specimen's temperature, the remaining unknowns of Equation (2.14), strain rate sensitivity, m, activation energy, Q, and material constant, A, can be determined through numerically solving this equation in regression to the experimental densification data. After arriving the optimal fitting, these obtained creep coefficients are used to solve an analytical equation that represents the porosity evolution under an ideal SPS-forging conditions (SPS with free lateral surface). The numerical solution of the SPS-forging setup is then compared to that of the regular SPS setup (SPS in a rigid die) to see which one is

more efficient on the porosity elimination. The theoretical investigations are aimed at proposing possibilities to achieve higher final density through the optimization of loading modes in the SPS of ZrC powder.

3.3.1 Determination of power-law creep and grain growth coefficients of ZrC

A phenomenological approach is employed here for the determination of the mass transport mechanism driving densification during spark plasma sintering. A significant advantage of this approach is in its capacity of using only an *in situ* macroscopic displacement data to clarify the ZrC deformational mechanisms and to directly obtain the values of the important constitutive parameters, such as the coefficients of power-law creep (strain rate sensitivity "*m*", in particular). It should be noted that similar approaches have been utilized in the above-mentioned works of Herring [45], Nabarro [46], Gifkins [146], Weertman , *etc*. [147-149].

The aforesaid classic studies, however, have been focused on the determination of the creep properties of fully dense materials, while the present work extrapolates this well-established methodology to the domain of porous (compressible) materials. The obtained values of the creep parameters can be directly used in the respective finite-element codes [151] developed for solving concrete SPS problems and enabling the predictions of the evolution of the relative density, stresses, strains, temperature, and electric current density spatial distributions.

The applied axial pressure, σ_z, is a known parameter in the conducted SPS experiments, and the specimen's temperature, *T*, has been estimated by the developed

finite element modeling framework. The coefficients A, Q and m are necessary to be pre-determined in order to solve Equation (2.14) numerically. An inverse regression can be conducted to minimize the discrepancies between numerical and experimental curves by substituting different series of A, Q and m parameters till their optimal combination is found.

Densification data obtained from performing regular SPS at 1700 ℃, control SPS and 1600 ℃ and hot pressing at 1900 ℃ were put into the platform of regression analysis. To facilitate the computation, the isothermal holding step of each process was particularly benchmarked as the use of constant temperature value can reduce the target equation's degree of freedom. In regard to the sintering stages, the hot-pressed ZrC ended up with an 84% relative density which corresponds to the intermediate sintering stage, while the regular SPS and the control SPS processed ZrC have evolved into the final sintering stage with more than 95% relative density being achieved.

A numerical differential equation solver, the 4^{th} order Runge-Kutta (RK4), was utilized to solve Equation (2.14) and plot the solutions in comparison to the experimental data in the same graph. The results of the inverse regression on regular SPS at 1700 ℃ are presented in Figure 3.13. As one can see, the numerical solution is converged with the experimental data even despite the existence of minor discrepancies near the end. The A, Q and m values at this point are then considered as the optimal combination of power-law creep coefficients of ZrC powder under the studied processing conditions, as listed in Table 3.6.

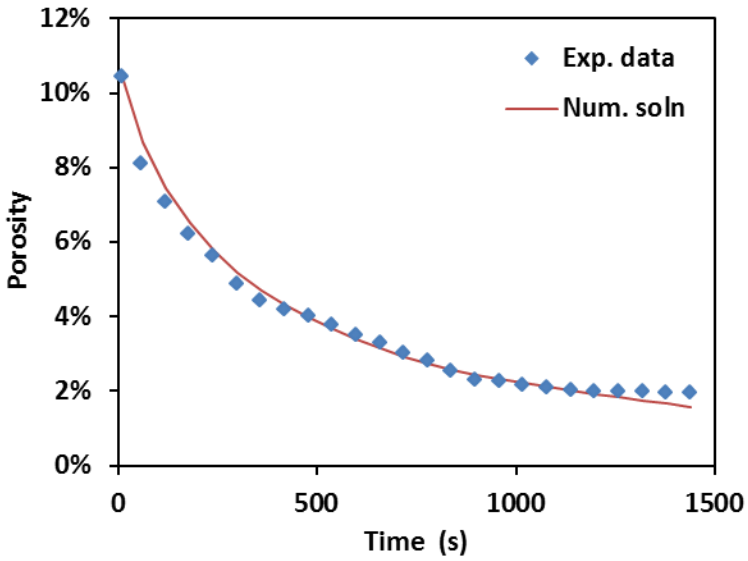

Figure 3.13 Numerical solutions *vs*. experimental data: porosity evolution in regular SPS of ZrC at 1700 ℃ under 60 MPa.

Densification mechanisms incorporated in the control SPS and hot pressing of ZrC under similar heating and loading profiles were investigated to explain the observed different densification kinetics in Figure 2.7. The selection of densification data from the control SPS runs was taking both the ramping up and the holding periods into account with relative density increasing from 75% to 95%. For hot pressing of ZrC, the densification data from the entire isothermal holding stage was selected in the regression analysis with the relative density ranging from 75% to 84%. These selections ensured the same starting porosity (~25%) in both cases.

It should be noted that, according to the selected range of relative density, the hot pressing only corresponds to the intermediate sintering stage while the control SPS includes two sintering stages with the intermediate one preceding the final one [4], and the densification rates associated with these two stages are different (see also Figure

2.7). Therefore, the study of densification mechanism involved in the intermediate stage was individuated from the one that engaged in the final stage. This approach enabled comparing densification mechanisms incorporated in hot pressing and SPS during the same sintering stage and extended the investigating approach that employed by Ref. [124], in which the intermediate and final SPS stages were counted together.

Porosity evolution during the control SPS has been first split into intermediate (Int) and final stages (Fin) in order to individuate the densification behaviors, and then these two stages were put together in one plot after inverse regression, as shown in Figure 3.14. The discontinuity of numerical solution at the junction point between the two stages (vertical dot-dash line) reflects the change of creep coefficients. The numerical solutions (Num. soln) also are in good agreement with the representative experimental data (Exp. data) in this case.

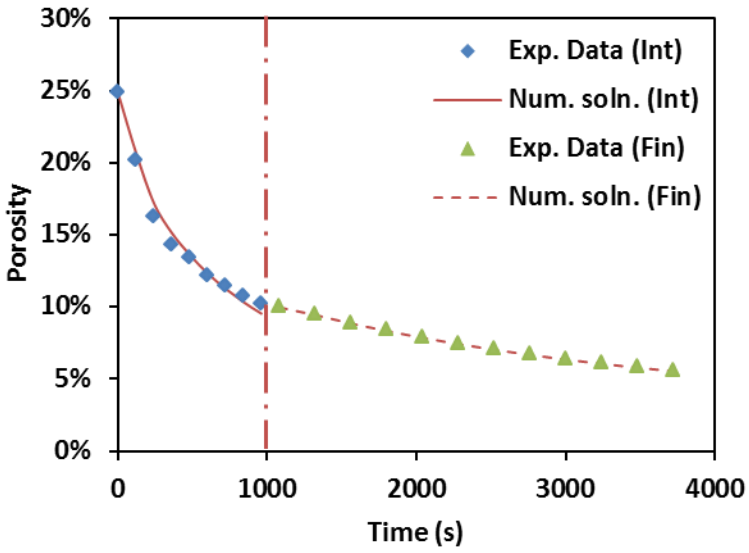

Figure 3.14 Numerical solutions *vs*. experimental data: porosity evolution in control SPS of ZrC at 1600 ℃ under 55 MPa.

In the same manner, the regression analysis on porosity evolution in the hot pressing of ZrC was conducted and the results are illustrated in Figure 3.15. As one can see, the numerical solutions reflect the representative experimental obtains. The reliability of Equation (2.14) for describing porosity evolution in the hot pressing of ZrC is therefore verified.

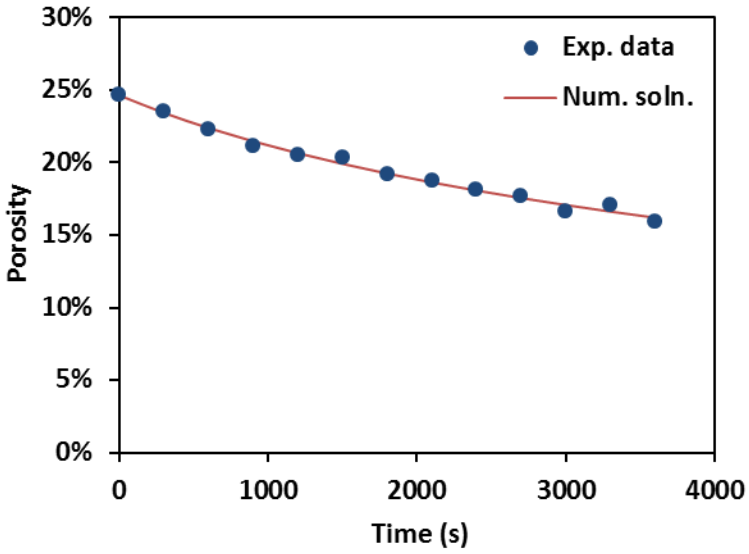

Figure 3.15 Numerical solutions *vs*. experimental data: porosity evolution in hot pressing of ZrC at 1600 ℃ under 55 MPa.

The obtained creep coefficients of ZrC powder under the three above-mentioned processing conditions are comparatively summarized in Table 3.6. All obtained m values, despite of the fluctuations, fall into a range from 0.33 to 0.5 (equivalent to n varies from 2 to 3). The densification mechanism of the selected ZrC powder involved in SPS and hot pressing is then shown to be most likely to be grain boundary sliding ($n = 2$) associated with dislocation glide controlled creep ($n = 3$). Also, high levels of apparent activation energy are exhibited, no matter what kind of

consolidation technique was used, indicating the poor sinter-ability of the studied ZrC powder.

Table 3.6 Optimal creep coefficients obtained from inverse regressions

Parameters	**Intermediate**			**Final Stage**		
	m	*Q (kJ/mol)*	*A*	*m*	*Q (kJ/mol)*	*A*
Regular SPS	N/A	N/A	N/A	0.405	567	6.53e-6
Control SPS	0.403	563	6.58e-6	0.403	576	6.58e-6
Hot pressing	0.382	653	5.92e-6	N/A	N/A	N/A

During the final SPS stage, regular SPS and control SPS resulted in almost identical creep parameters even despite the fact that they were subjected to different holding temperatures. This consistency indicates that the creep coefficients may not directly depend on the processing temperature in the investigated temperature range. The m value obtained for the hot pressing was slightly smaller than that of the control SPS obtained for the same sintering stage, while the control SPS rendered a way lower Q value than the one that the hot pressing provided. Comparatively higher strain rate sensitivity and lower activation energy retrieved from the SPS runs can be attributed to the contribution of electric current improving the neck growth between particles. Although quantitative evaluations of the current effect in the SPS process are still ongoing, as shown in [74, 119], the inter-particle necks have been observed to be formed at the early SPS stages. Extra atomic diffusional paths created this way substantially accelerated the activation of the plastic flow.

At the same time, during hot pressing, the inter-particle necks (see also Figure 2.8 a) appear to just start growing during the intermediate stage, and, thus, provided less support for mass transport. Therefore higher energy was required in the case of hot pressing. The creep coefficients of the control SPS at the intermediate and final sintering stages are nearly identical except slightly different values of the activation energies. This difference might be related to the underestimation of the specimen's temperature and the viscous analogue of the shear modulus due to the influences of porosity during the final stage of SPS.

The simulated specimen's temperatures were also utilized in the evaluation of grain growth in SPS-processed specimens. Chaim stated that, besides temperature and time, the grain growth in SPS of porous ceramics is also controlled by the pore mobility [114]. An equation that includes the dependence of the grain growth on these factors was proposed by Olevsky *et al*. as [151],

$$G^g = G_0^g + k_0 t \left(\frac{\theta_c}{\theta + \theta_c}\right)^{\frac{3}{2}} exp\left(-\frac{Q_G}{RT}\right) \tag{3.11}$$

where G_0 is the initial grain size, g is the grain growth exponent, k_0 is the grain growth constant, θ_c is the critical porosity which reflects the transition from open to close porosity and Q_G is the activation energy for grain growth (*J/mol*).

By using the simulation approach provided in the last section, the specimen's temperature, T, was evaluated to be 2303 K (~2030 ℃) in correspondence to a pycnometer measured temperature of 1700 ℃. The critical porosity, θ_c, was

determined through the open porosity measurements using a helium pycnometer (AccuPyc 1330, Micromeritics Corp., Norcross, GA, USA) by taking into account the difference between the apparent and the pycnometric relative densities.

The specimen's open porosities are plotted with respect to their relative densities in Figure 3.16. The decrease of open porosity suddenly turns into a plateau with open porosity close to zero after relative density reaches 93%, which indicates the open pores in these specimens are nearly gone. The turning point in Figure 3.16 was therefore considered to be the moment of transition from open porosity to close porosity and the value of $\theta_c$was set to 0.07 in the evaluation of other grain growth coefficients.

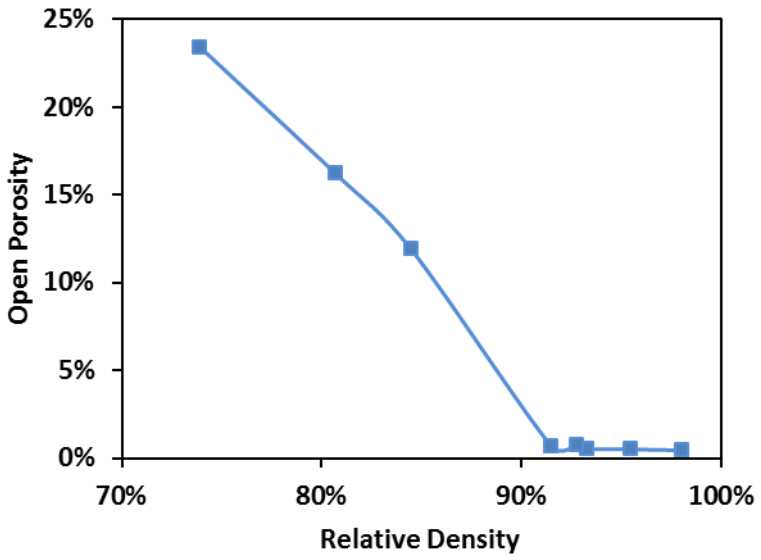

Figure 3.16 Open porosity *vs.* relative density for SPS-processed ZrC specimens.

An Excel® Solver program was used to assess the values of g, $k_0$and Q_G. By iteratively optimizing these values, as demonstrated by the dashed line in Figure 3.17,

Equation (3.11) produced a set of calculated grain sizes which are close to the experimental ones. Also, the coefficient optimization gave a grain growth exponent of $g \approx 2$ which corresponds to the grain boundary diffusion controlled grain growth [114]. The observed insignificant change in density during the final holding stage in the present study is in agreement with the study of Djohari *et al.*, in which the grain boundary diffusion has been described as a cause of virtually little densification in the later stage of sintering [170]. Also, the activation energy for grain growth was estimated to be 290 *kJ/mol*. This value is way lower than the activation energies found for zirconium lattice diffusion (720 *kJ/mol*, [171]), for carbon bulk self-diffusion (470 *kJ/mol*, [172]) in ZrC_x and for viscoelastic creep-introduced densification (576 *kJ/mol*, see also Table 3.6), suggesting that the grain growth was preferred during the final stage of SPS of ZrC compared to other mechanisms.

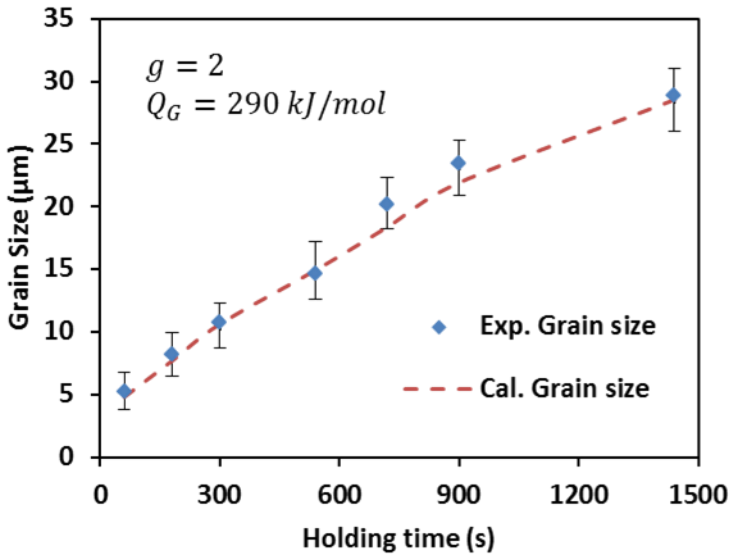

Figure 3.17 Calculated grain sizes in comparison to experimental data, SPS of ZrC at 1700 ℃.

3.3.2 Densification of porous ZrC specimens under SPS-forging conditions

When conducting SPS runs with free up-setting loading mode, the term "spark plasma sinter-forging (SPS-forging)" is used in the present study. To theoretically study the densification of ZrC under such a forging setup, the continuum theory of sintering was employed again. If a porous or powder-based cylindrical specimen is free up-set with axial stress, σ_z, being applied at its top surface, as discussed in Section 1.1.1.1, there is no lateral constrains acting on the specimen. Therefore the radial stress at the specimen's lateral surface, σ_r, according to Equation (2.7), can be written in cylindrical coordinate system, as,

$$\sigma_r = A_{cr} W^{m-1} \left[\varphi \dot{\varepsilon}_r + (\psi - \frac{1}{3}\varphi)\dot{e} \right] = 0 \tag{3.12}$$

which results in equations below, if ideal boundary conditions are applied (no contact friction),

$$\varphi \dot{\varepsilon}_r = -(\psi - \frac{1}{3}\varphi)(2\dot{\varepsilon}_r + \dot{\varepsilon}_z) \tag{3.13}$$

with the substitution of Equations (2.10) and (2.11), the ratio between the radial strain rate, $\dot{\varepsilon}_r$, and the axial strain rate, $\dot{\varepsilon}_z$, can then be obtained as the follows:

$$\frac{\dot{\varepsilon}_r}{\dot{\varepsilon}_z} = \frac{3\theta - 2}{4 - 3\theta} \tag{3.14}$$

and then the specimen's volume change rate, $\dot{e}$, is expressed as,

$$\dot{e} = 2\dot{\varepsilon}_r + \dot{\varepsilon}_z = \frac{3\theta}{4-3\theta}\dot{\varepsilon}_z \tag{3.15}$$

To simplify this analytical problem, ideal free up-setting loading mode (see also Figure 1.1**)** is assumed here. The shape change rate, $\dot{\gamma}$, under such boundary conditions can be derived as,

$$\dot{\gamma} = \sqrt{\frac{2}{3}}|\dot{\varepsilon}_z - \dot{\varepsilon}_r| = \sqrt{\frac{2}{3}}\left(\frac{6-6\theta}{4-3\theta}\right)|\dot{\varepsilon}_z| \tag{3.16}$$

putting Equation (3.15) and (3.16) together to have,

$$\dot{\gamma} = \sqrt{\frac{2}{3}}\left(\frac{2-2\theta}{\theta}\right)|\dot{e}| \tag{3.17}$$

the equivalent strain rate, *W*, is the following,

$$W = \frac{1}{\sqrt{1-\theta}}\sqrt{\varphi\dot{\gamma}^2 + \psi\dot{e}^2} = (1-\theta)\left(\frac{2(4-3\theta)}{3\theta^2}\right)^{\frac{1}{2}}|\dot{e}| \tag{3.18}$$

After substituting Equations (2.10) - (2.12), (3.15) and (3.18) into Equation (2.13), the axial stress, $\dot{\sigma}_z$, along the surface of a porous specimen under ideal free up-setting loading mode can be expressed in terms of the specimen's pre-creep coefficient, A_{cr}, strain rate sensitivity, m, and porosity, θ, as,

$$\sigma_z = -2A_{cr}\theta^{-m}(1-\theta)^2\left(\frac{2}{3}(4-3\theta)\right)^{\frac{m-1}{2}}\dot{\theta}^m \tag{3.19}$$

after representing A_{cr} explicitly by Equation (2.8), below equation is retrieved,

$$\dot{\theta} = \frac{d\theta}{dt} = -\frac{A}{T} exp\left(-\frac{Q}{RT}\right)\left(\frac{\sigma_z}{2}\right)^{\frac{1}{m}} \theta \left(\frac{2}{3}(4-3\theta)\right)^{\frac{1-m}{2m}} (1-\theta)^{-\frac{2}{m}} \qquad (3.20)$$

Equation (3.20) is derived based on the boundary conditions of a porous cylinder subjected to ideal free up-setting loading mode. Similar to Equation (2.14), this analytical equation describes how mass transport evolves with time at certain temperature and pressure under the control of power-law creep mechanism.

Since the power-law creep coefficients of ZrC under SPS conditions have already been determined (see also Table 3.6), Equation (3.20) was solved numerically to predict the densification behavior of porous ZrC specimen subjected to SPS-forging. Figure 3.18 compares the numerical solutions of SPS-forging (Equation (3.20)) to these of regular SPS (Equation (2.14)) with substituting the same initial porosity (0.25) and axial pressure (60 MPa) into the equations. The specimen's temperature was set to 2303 K in correspondence to an SPS processing temperature of 1700 ℃. Also, identical power-law creep coefficients were used in both equations to allow the same control mechanism taking place.

As one can see, under same processing parameters and power-law creep coefficients, regular SPS process gives slightly higher densification level than SPS-forging at the beginning. However, this initial lead diminishes as porosity reduces. When porosity goes below 0.1, which corresponds to the final stage of sintering [112], the porosity evolution trend reverses and SPS-forging leads the " competition" till the end with achieving a less final porosity. These developed analytical models therefore

have been verified to be able to distinguish the effects of loading modes on the densification behaviors.

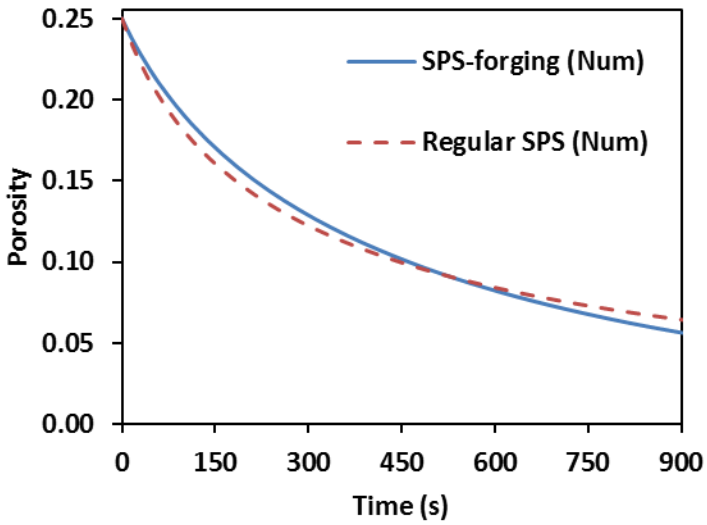

Figure 3.18 Numerical solutions of porosity evolution: ZrC subjected to SPS-forging and regular SPS runs.

The comparison also reveals, to certain extend, SPS-forging is more efficient than regular SPS in the process of pore elimination. Since the introduction of loading mode can influence the densification of porous ZrC, there should be some possibilities to manipulate loading modes in SPS of ZrC in order to reach higher final density. However, these analytical densification expressions were derived based on ideal assumptions without considering interactions between tooling and specimen such as the contact friction force. Therefore, even though the numerical solutions of these equations have provided prospects on how specimen's density evolves under different SPS loading modes, they reliabilities are still necessary to be verified via detailed experimental implementations.

3.4 Experimental Investigation of Influence of Loading Modes in SPS of ZrC

Although the free forging setup has been applied to consolidate powder compacts since decades ago [26, 27], until recently it has not been implemented in SPS devices. Spark plasma texturing (SPT) was designed with the purpose of producing thermoelectric materials with oriented microstructures and intensified properties [173-175]. Aleksandrova *et al*. used the same setup named "spark plasma sinter-forging" (SPS-forging) to investigate the contribution of electric current in the SPS process, and introduced the equations to describe the specimen's dimension change in all the directions [176]. However, densification kinetics of the SPT or SPS-forging process have not been analyzed in detail in the previously conducted studies.

The SPS-forging setup is employed to process ZrC. The densification kinetics of porous ZrC specimen subjected to SPS-forging are compared to those of the specimens exposed to a regular SPS under the same processing conditions. The modeling predictions provided in the last section are verified by the experimental observations. To regulate the shape of the final specimen, SPS-forging and regular SPS are combined to form a novel hybrid loading mode SPS setup. The hybrid SPS of ZrC is conducted with imposing loading control to secure the densification. The derived analytical densification equations are also combined to theoretically study the densification of ZrC during the hybrid SPS process.

3.4.1 Tooling setups and experiment procedures

ZrC powder (99% metal basis, Sigma-Aldrich Co., St. Louis, MO, USA) with an average particle size < 10 μm was used in the experimental investigations. The utilized powder is exactly the same to the one that was analyzed in CHAPTER 2. The weighted powder was placed in a set of 10 mm graphite tooling (I-85 graphite, Electrodes Inc., Santa Fe Springs, CA, USA) and pre-sintered in SPS apparatus (SPSS-515, Fuji Electronic Industrial Co., Kawasaki, Japan) up to 1600 ℃ with a heating rate of 100 ℃/min. The holding time was set to 1 min holding and the pressure was 45 MPa. This processing profile provided the pre-sintered samples with a relative density level around 75%, on the basis of the geometric measurements. These porous ZrC cylinders were ground to remove the residual graphite paper from its outer surfaces before density characterizations.

To form an SPS-forging setup, as shown in Figure 3.19 a, the pre-sintered cylinder was horizontally centered in a 15 mm graphite die with the supports from two aligned 15 mm graphite punches (I-85 graphite, Electrodes Inc., Santa Fe Springs, CA, USA). The current SPS-forging setup is very similar to what Ref. [176] schemed. It isolates specimen's lateral surface from the die wall and allows displacements occurring along both axial and radial directions during the forging process. During regular SPS "control" runs, both the pre- and the post-sintering steps were carried out in the 15 mm graphite tooling setup, therefore the sample was always in contact with the die wall under the applied axial load (Figure 3.19 b). In order to make the control SPS comparable to the SPS-forging except the loading mode, the ZrC powder was

also pre-sintered to a relative density of 75% and then processed again under the regular SPS conditions.

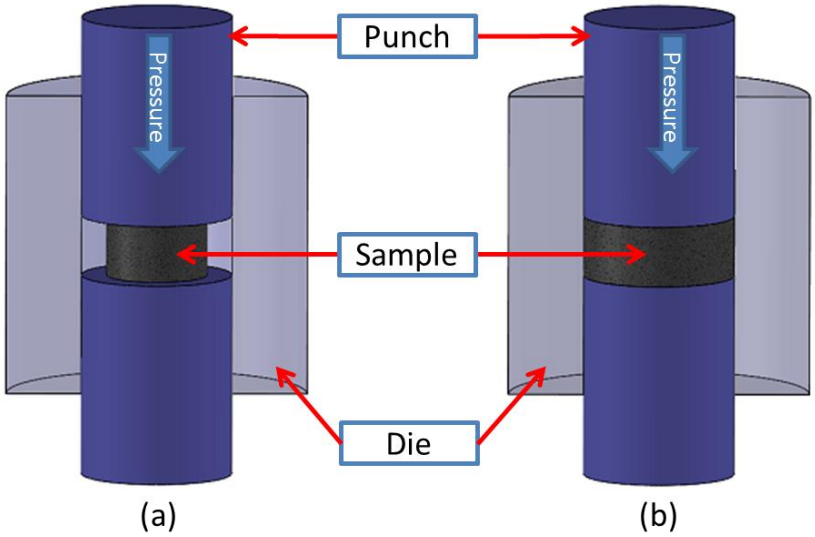

Figure 3.19 Schematics of (a): SPS-forging setup and (b): regular SPS setup.

Temperatures during both SPS-forging and regular SPS control runs were monitored by focusing a digital pyrometer at the outer surface of the graphite die. The heating rate was 100 ℃/min to 1600 ℃, and then 50 ℃/min to 1700 ℃. In SPS-forging runs, the external load was kept at the minimum level (~3 kN) at first and then increased to 4.71 kN in 1 min right before the start of the isothermal holding to give a 60 MPa pressure to the specimen. Then the axial load was increasing slightly during the holding stage of the SPS-forging process. Such a loading profile was used to accommodate the change of the specimen's cross-sectional area and maintain the resulting pressure at the same level compared to the one used in the regular SPS (60 MPa). Same loading profile was utilized in the regular SPS runs prior to the onset of holding stage. After that, the axial load was kept at 10.6 kN to provide a consistent

pressure of 60 MPa till the end of the sintering process. Holding time spanned from 1 to 15 mins and all experiments were conducted in argon atmosphere.

3.4.2 Densification of ZrC under SPS-forging and regular SPS setups

The densities of all the post-sintered specimens were determined by the Archimedes method. The ratio of the measured density of a specimen to the theoretical density of ZrC was calculated as the relative density while the fractional difference between them was counted as porosity. In Figure 3.20, the densification kinetics obtained from conducting the SPS-forging runs is compared to the one retrieved from performing the regular SPS runs. One can see that, starting from similar initial density, the SPS-forging rendered lower relative densities evolving below the regular SPS data at the beginning. Then the former started showing higher densification intensity and subsequently exceeded the achieved density under the regular SPS after 6 - 7 mins. As a result, SPS-forging processed specimens exhibited higher relative density than the regular SPS-processed ones at the end.

Compared to Figure 3.18, the relative density difference (equivalent to porosity difference) between the experimentally obtained curves appear to be a bit larger than that between the numerically solved sets, which can be attributed to the fact that the SPS-forging experiments were influenced by friction forces at the contact surfaces, while analytical equations were derived assuming ideal contact sliding conditions. Despite the discrepancies, the developed analytical models have been verified to be able to distinguish the effects of loading modes on the densification behaviors. The theoretical investigation has also clarified why the SPS-forging ended up with higher

final density than the regular SPS: the free up-setting mode generated extra shear strain components which could facilitate the deformation as well as the mass transport of the porous specimen (see also Equations (3.14) - (3.17)).

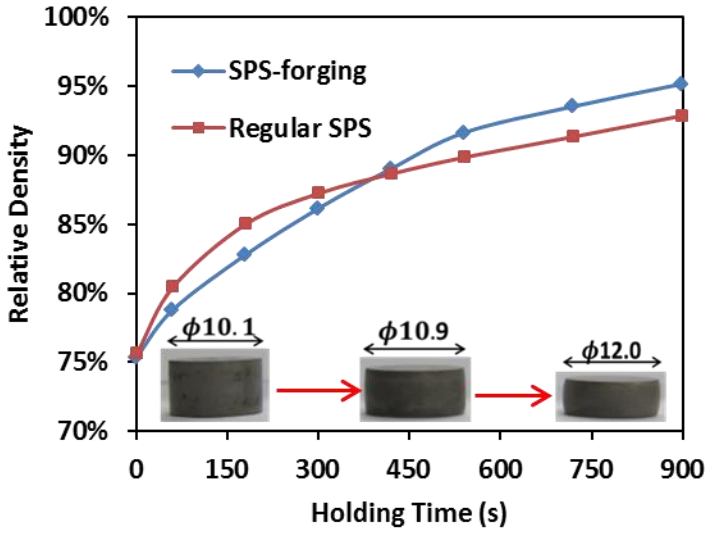

Figure 3.20 Comparison of densification kinetics: SPS-forging *vs.* regular SPS at 1700 ℃ under 60 MPa.

3.4.3 SPS of porous ZrC with hybrid loading mode

The presence of contact friction has introduced a non-uniform increase of the specimen's diameter during the SPS-forging process. As illustrated in the bottom part of Figure 3.20, slight shape barreling has appeared on the final specimens. These barreled surfaces could be the sources of cracks when the powder substance becomes denser and less deformable since there are no other constraints to offset the non-uniformity of the free up-set specimen. To regulate the shape of the final specimen and to avoid cracking, the geometry of the die cavity was utilized in the present study. The

idea was to form an SPS hybrid loading mode carrying out SPS-forging and SPS in a rigid die consecutively in one run.

To practically implement such an experimental design, the first step was aimed at pressing the pre-sintered cylinder to reach the die wall through the free-forging process so that the specimen could reach the die wall to have a disk-like shape in the next rigid die pressing step. Therefore the loading profile used in the hybrid SPS run was configured to satisfy: i) high pressure at the beginning to facilitate the onset of the specimen – die interaction; ii) moderate pressure since then to continue the deformation/densification of the specimen with the confinements from the die wall. The hybrid SPS tooling setup was designed to follow the deformation schematics illustrated in Figure 3.21. Also, porous ZrC cylinders with about 75% relative density were pre-sintered for the hybrid SPS experiments.

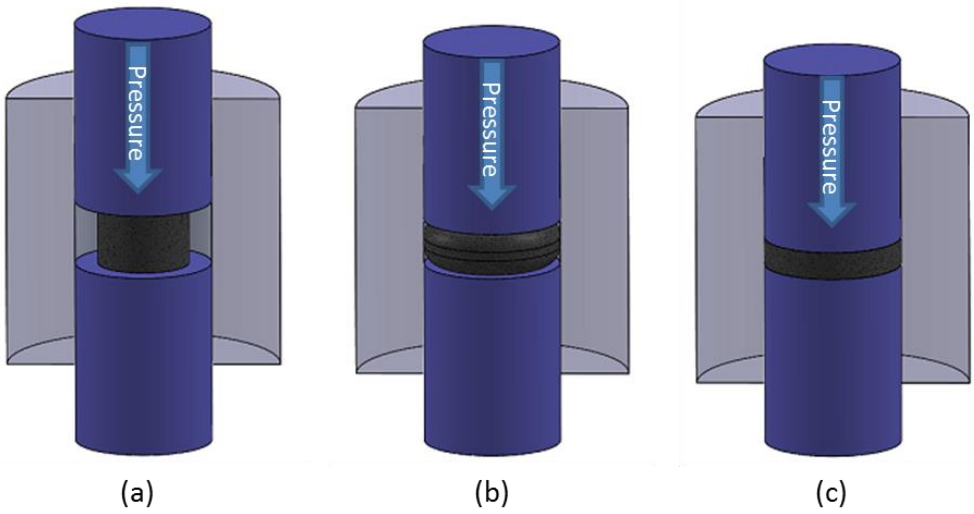

Figure 3.21 Deformation schematics for hybrid loading mode SPS process, (a): Initial, (b): intermediate and (c): final status.

Based on the above-mentioned pressurizing prerequisites and the expected deformation schematics, the employed loading profile for hybrid SPS runs is given in Figure 3.22. An initial load of 8.6 kN was applied to the pre-sintered 10 mm cylinder, which was equivalent to an initial pressure of 110 MPa. The load was kept at the same level till the specimen touches the die wall (15 mm in diameter) through the free-forging process. Then the axial load was increased and kept at 10.6 kN to provide a constant pressure of 60 MPa to process the specimen under a rigid die pressing mode till the end of each experiment.

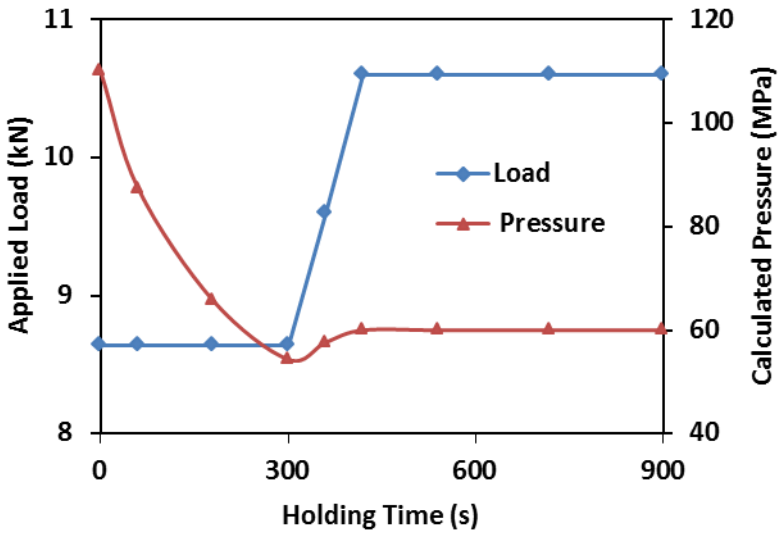

Figure 3.22 Loading profile and resulting pressure evolution in hybrid SPS of ZrC.

During the SPS-forging of a porous specimen, if the applied load is kept constant, the specimen's instantaneous cross-sectional area, S, depends on its porosity, θ, as [20],

$$S = S_0 \cdot exp\left(2\int_{\theta_0}^{\theta} \frac{\frac{\varphi}{3} - \psi}{\varphi(1-\theta)} d\theta\right) = S_0 \cdot \left(\frac{1-\theta_0}{1-\theta} \cdot \frac{\theta_0^2}{\theta^2}\right)^{2/3} \tag{3.21}$$

where S_0 is the initial cross-sectional area and θ_0 is the initial porosity. Therefore, the actual pressure, σ_z, acting on the specimen under a constant load, f, can be theoretically calculated as,

$$\sigma_z = \frac{f}{S} = \frac{f}{S_0\left(\frac{1-\theta_0}{1-\theta} \cdot \frac{\theta_0^2}{\theta^2}\right)^{2/3}} \tag{3.22}$$

The evolution of the specimen's porosity was obtained after carrying out hybrid SPS runs at 1700 ℃ with holding time ranging from 1 to 15 min. By substituting these experimental outcomes back into Equation (3.22), the evolution of the axial pressure resulted from applying the two-step loading profile in the hybrid SPS process was retrieved. As illustrated in Figure 3.22, a large pressure drop during the SPS-forging step is shown which reflects a considerable increase in the specimen's cross-sectional area. The pressure went slightly lower than 60 MPa but soon came back due to the increase of load at the moment when the specimen’s lateral surface arrived at the die wall and the loading mode switched to rigid die pressing. Since then the pressure was fixed at 60 MPa to extend the densification behavior through the second regular SPS step.

The densification kinetics of porous ZrC during hybrid SPS process are plotted in Figure 3.23, As one can see, it consists of two segments corresponding to the two different SPS setups. High axial pressure initiated fast densification when the SPS-

forging step was imposed at the beginning. During this stage, the specimen's diameter grew gradually and the axial pressure decreased accordingly. As a result, the densification slowed down as the holding time went on. The specimen reached the die wall in about 5 - 6 mins and then was subjected to the regular SPS to continue the densification process under the rigid die pressing mode. Compared to SPS-forging or regular SPS runs conducted under similar conditions (see also Figure 3.20), the hybrid SPS process was able to produce specimens with slightly higher final relative densities keeping their geometry as a regular disk-like shape. By and large, the hybrid step appears to be able to take advantages of its individual process components.

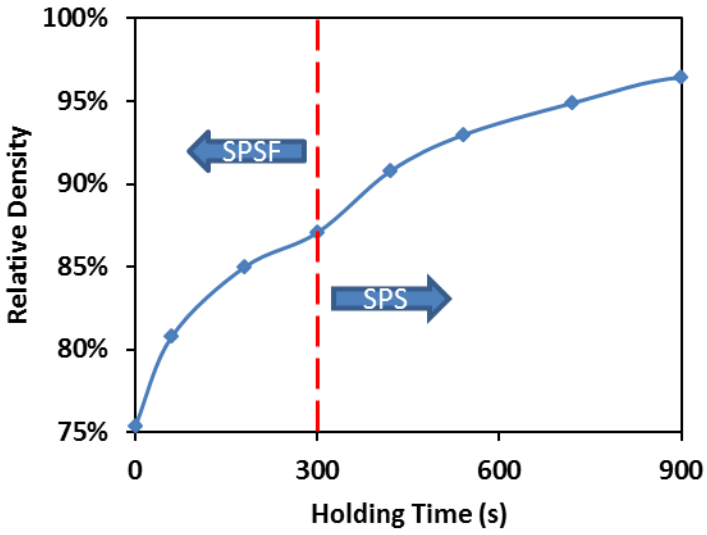

Figure 3.23 Densification kinetics of ZrC during hybrid SPS at 1700 ℃ with loading control.

To investigate the porosity evolution during the hybrid SPS process using the developed analytical models, Equations (3.20) and (3.22) were considered jointly with Equation (2.14) to represent the kinetics induced by different SPS loading modes. This

set of differential equations was solved by a numerical method using the pre-determined creep coefficients. As shown in Figure 3.24, the obtained solutions clearly reveal the transition of loading modes during the hybrid SPS process by distinguishing the specimen's shrinkage kinetics. However, during the first segment when SPS-forging is imposed, the analytical model seems not in good agreement with the experimental data as it appears to introduce a faster densification profile. The porosity non-conformance can be probably attributed to the creation of micro-voids during the specimen's fast deformation (barreling) in the real experimental runs. Despite the understandable discrepancies during the first segment, when the regular SPS is applied in the next one, the numerical solutions have provided a reliable description of the experimentally obtained porosity evolution profile.

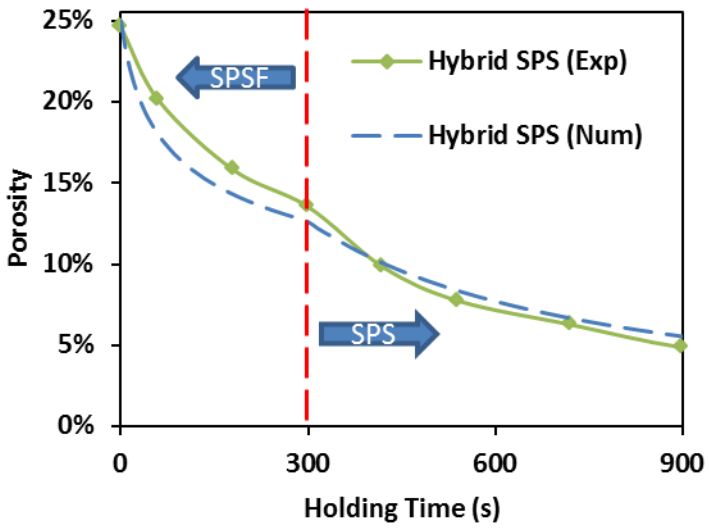

Figure 3.24 Numerical solutions *vs*. experimental data: Porosity evolution in SPS of ZrC with hybrid loading mode.

3.5 Chapter Conclusions

Horizontal and vertical electric contact resistances were experimentally examined by conducting SPS with graphite tooling under temperature control mode. The effects of both temperature and pressure on the evolution of contact resistance during SPS were quantitatively and jointly analyzed for the first time. Horizontal contact resistance displays a nonlinear relation to either the temperature or the pressure as it is mainly caused by nonlinear creep induced by thermal and mechanical effects. While the vertical contact resistance reveals an almost linear dependence on the temperature and the pressure as thermal expansion and Poisson deformation are the primary contributions. Horizontal resistance seems to have more complicated mechanism than the vertical one even though the former is approximately one order of magnitude less than the later.

Upon the clarification of contact resistance in the currently utilized SPS tooling system, the temperature evolution in the SPS tooling was able to be implemented using finite element simulation with coupling different physical phenomena. The developed modeling framework was used to characterize the thermal gradient generated between the die surface and the specimen during SPS of ZrC. The actual temperature of the ZrC specimen was calibrated by correlating the simulated temperatures with respect to the pyrometer measured ones directly. The simulation work has also suggested that both the electric and the thermal contact resistances are of importance for accurately evaluating the temperature distribution in the current SPS system.

The simulated specimen's temperatures were subsequently substituted into the porosity evolution equation which derived in CHAPTER 2 to evaluate the power-law creep coefficients of the selected ZrC powder under various processing conditions. The differential equation was solved numerically and compared to the experimental densification data in inverse regression analyses to determine the optimal creep coefficients of ZrC. The obtained strain rate sensitivity value revealed that the mass transport mechanism during the densification of the ZrC powder is most likely to be the grain boundary sliding associated with the dislocation glide-controlled creep. The determination of the optimal creep coefficients enabled the theoretical investigation of the influence of loading modes on densification kinetics. An SPS-forging setup was proposed and the corresponding porosity evolution equation was derived by assigning appropriate boundary conditions. Theoretical densification kinetics was obtained after solving the SPS-forging equation, suggesting that SPS-forging is able to introduce higher final density compared to regular rigid die pressing SPS. However, these modeling results need to be verified by experiments.

The influence of loading modes on densification efficiencies has been examined experimentally by applying SPS-forging and regular SPS setups to consolidate porous ZrC specimens. SPS-forging was shown to be able to achieve higher final density level than regular SPS under same heating and loading profiles. The shear strain components introduced by the free up-setting loading mode were considered as the major process factors which enhanced both deformation and densification in the SPS-forging process. Numerical solutions of analytical equations

exhibited good agreements with experimental results evidencing the reliability of the developed models. To avoid shape barreling after SPS-forging treatment, hybrid SPS setup was implemented by carrying out SPS-forging and regular SPS in a consecutive way with a proper loading control. Both the densification and the shape of the specimen can be controlled by the newly developed hybrid SPS process.

Both experimental and modeling approaches have been conducted to characterize the thermal and mechanical aspects in the hot consolidation (SPS and hot pressing) of ZrC powder. The obtained results can be used for future optimization purposes including the possible design of material structures in a sophisticated way.

Chapter 3, in part, is a reprint of the material as it appears in "X. Wei, D. Giuntini, A. L. Maximenko, C. D. Haines and E. A. Olevsky, Experimental investigation of electric contact resistance in spark plasma sintering tooling setup, *J. Am. Ceram. Soc.*, 98, 2015", and may appear in "X. Wei, A. L. Maximenko, C. Back, O. Izhvanov, E. A. Olevsky, Effects of loading modes on densification efficiency of spark plasma sintering: sample study of ZrC consolidation, *Phil. Mag. Lett.*, 2016" The dissertation author was the primary investigator and author of these papers.

CHAPTER 4 SPARK PLASMA SINTERING OF POWDER COMPONENTS WITH TAILORED STRUCTURES AND PROSPECTIVE APPLICATIONS

Spark plasma sintering has been shown to be able to consolidate the poorly sinter-able ZrC powder into nearly fully dense articles. However, prospective applications of such a kind of ultra-high temperature ceramics usually require the components to be fabricated to have tailored structures. As discussed in CHAPTER 1, the net-shaping capabilities in SPS of UHTC powders have merely been explored in the past due to the hard and refractory natures of the materials themselves. The successful production of the cylindrical shape ZrC specimens has provided useful information to further investigate the SPS capacity of processing carbide components with complex shapes. The annular shape or the ring-like shape is considered here as the first step to being a more complex geometry compared to a cylinder or a disk.

Special graphite tooling is designed for achieving the annular shape geometry. Experiments are carried out with applying the optimal processing conditions extracted from the SPS of cylindrical ZrC specimens. Finite element modeling framework is constructed to manifest the internal stress evolution as well as the densification during the SPS of annular shape ZrC. The formulated processing schemes are adapted to produce annular shape SiC/ZrB_2 composites with the purpose of exploring alternative materials for SPS tooling applications. The applicability of the annular shape structure to accommodate the swelling of nuclear fuel is preliminarily studied through analytical

modeling by considering the swelling of the substance. Then this idea has been extrapolated to characterize both the sintering and the swelling of annular shape fuel pellet subjected to nuclear irradiation via finite element simulation.

4.1 Fabrication of Annular Shape ZrC Pellets via SPS

4.1.1 SPS tooling and processing details

Special graphite tooling (I-85 graphite, Electrodes Inc., Santa Fe Springs, CA, USA) was utilized to produce an annular pellet with an inner diameter of 5 mm and an outer diameter of 18 mm. Tooling schematics are illustrated in Figure 4.1 with annotating the dimensions of each individual component. As one can see, one end of the thin mandrel was first inserted through the central hole on the lower punch. Such a design allows the mandrel properly sitting at the center of the die when aligning the lower punch with respect to the die wall. The weighted ZrC powder (99% metal basis, Sigma-Aldrich Co., St. Louis, MO, USA) was carefully laid into the annulus die cavity between the die wall the mandrel surface. The upper punch was used to close the powder-loaded die cavity with holding the other end of the mandrel in position.

Before assembling the graphite components together, they were pre-lined by 0.15 mm graphite foils (Fuji Electronic Industrial Co., Ltd., Kawasaki, Japan) to fill up the preset clearance between them. The powder bed was pre-compacted at the room temperature under a load of 3 kN. Then the entire tooling setup was placed in the SPS chamber (Fuji Electronic Industrial Co., Ltd., Kawasaki, Japan) along with the large graphite spacers. By referring to the conditions that were employed in processing

cylindrical shape ZrC specimens (see also CHAPTER 1), the maximum processing temperature, the heating rate and the applied pressure used in the SPS of annular shape pellets were set to 1700 ℃, 100 ℃/min (50 ℃/min after 1600 ℃) and 60 MPa, respectively. The holding time was spanned from 1 to 25 min.

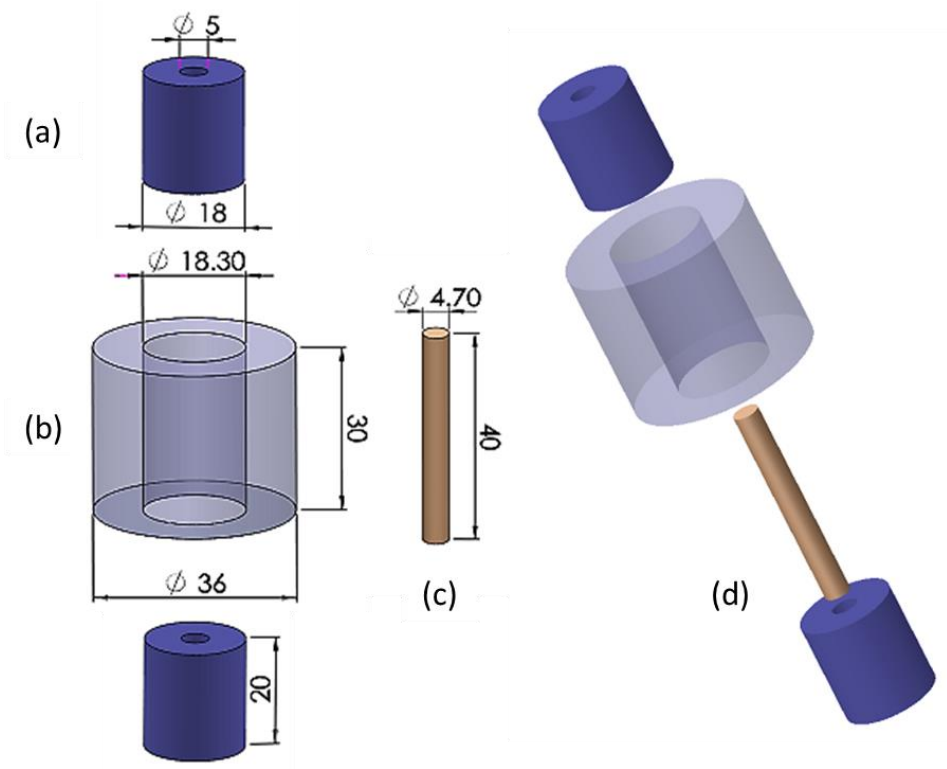

Figure 4.1 Tooling schematics for producing annular shape pellets: (a) Punch; (b) Die; (c) Mandrel; (d) Isometric view. Tooling dimensions are also presented (unit: mm).

Temperature evolution during the SPS processing was monitored by pointing a digital pyrometer at the outer die surface. The SPS machine was in the temperature control mode to regulate the rapid heating stage. Since the mandrel is the thinnest part of the annular tooling system, it could cause potential tooling failure during the pressure-assisted sintering process as a result of possible stress concentration.

Therefore the consistent 60 MPa pressure was not applied throughout the entire SPS process. Instead, the applied pressure was kept at the minimum level (~13 MPa) to ensure the pass of electric current at the beginning and then it was gradually increased to 60 MPa at selected temperatures. This two-step loading mode was aimed to i) evaluate the stability of the annular shape tooling during the process, ii) compare the densification behaviors when introducing pressures at different occasions. The SPS chamber was first vacuumed and then filled up with argon atmosphere during all experiments. The processing temperature, applied force and ram displacement were captured by the SPS computer.

Every individual experiment was repeated at least twice in order to ensure the reproducibility. The SPS-processed specimen was first ejected out with the mandrel from the die cavity by a mechanical press. After pulling out the mandrel from the specimen, a through hole was left at the center of the pellet to make the annular shape. The obtained annular pellets were ground by SiC abrasive paper to remove the excessive graphite foil from their surfaces. The densities of the annular shape ZrC pellets were measured using both geometric and Archimedes methods with the purpose of examining the reliability of the measurements. The real-time densification kinetics was obtained based on the true axial displacement of the specimen during SPS, in which the height change of the graphite tooling was subtracted from the original machine-logged readings.

4.1.2 Densification of annular shape ZrC pellets under SPS conditions

Figure 4.2 plots the evolutions of relative density and applied pressure with respect to processing time during SPS of annular shape ZrC at the maximum processing temperature of 1700 ℃. In this set of experiments, the pressure was increased from 13 MPa to 60 MPa in two minutes when processing temperature reached 1600 ℃. It is easy to observe that the increase of loading has introduced rapid densification to the specimen and more than 20% volume shrinkage has occurred during this short period of time. The densification slowed down since then even the processing temperature was further brought to 1700 ℃ and the pressure was consistently held at 60 MPa for 25 min.

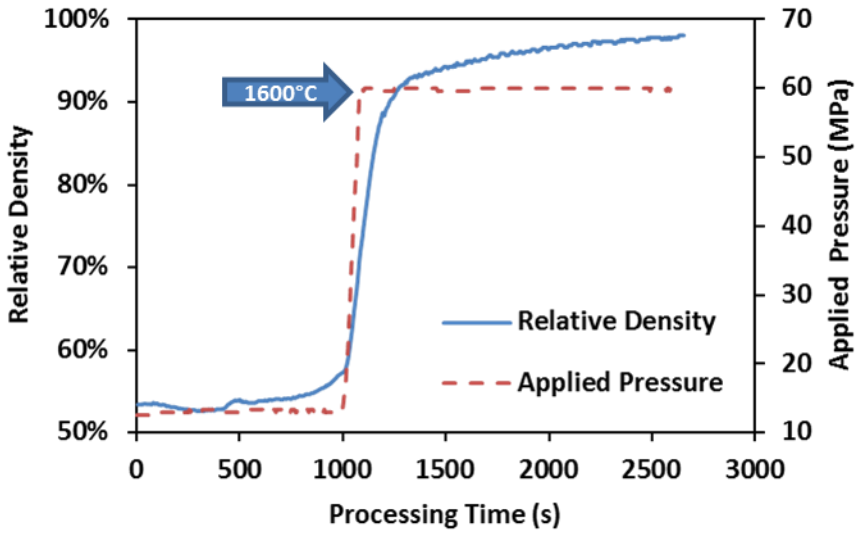

Figure 4.2 Relative density *vs*. processing time: SPS of annular shape ZrC pellets at 1700 ℃, 60 MPa pressure applied at 1600 ℃.

Annular shape ZrC pellets with high final relative densities (> 98%) were produced at the end. The obtained relative density levels are comparable to those retrieved from processing cylindrical shape ZrC specimens (see also Figure 2.5), suggesting that the selected SPS conditions were suitable for both geometries. Another set of experiments were conducted with exact the same temperature profile except the 60 MPa pressure was introduced at temperatures much lower than 1600 ℃. Fox example, Figure 4.3 presents the densification kinetics associated with SPS of annular shape ZrC, in which the pressure was increased to 60 MPa at 600 ℃.

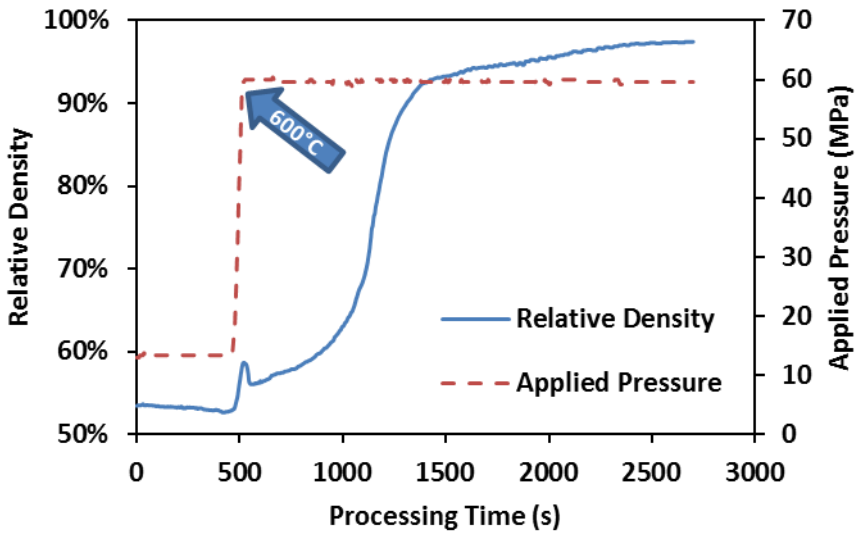

Figure 4.3 Relative density *vs*. processing time: SPS of annular shape ZrC pellets at 1700 ℃, 60 MPa pressure applied at 600 ℃.

As one can see, unlike what has been seen in Figure 4.2, the sudden rise of pressure at a lower temperature did not lead to significant volume shrinkage. By considering the high melting temperature of ZrC (~3500 ℃), it is safe to say that the ZrC powder is still in a rigid phase at 600 ℃. Therefore, the ~5% volume shrinkage

can be mainly attributed to the reduction of voids between particles and can be partially caused by the rearrangement of the particles themselves when a 60 MPa pressure was applied. Fast densification actually occurred far behind this point when processing temperature was high enough to trigger the viscous flow in the ZrC porous body. However, high relative density still has achieved as time elapsed.

Densification behaviors obtained from imposing different loading profiles in SPS of annular shape ZrC are compared in Figure 4.4 with the evolution of processing temperature. Starting from the same initial relative density, similar final relative density levels have been attained in both cases but the density evolution varies regarding individual sintering stages. Applying 60 MPa pressure at 600 ℃ appears to facilitate the densification of ZrC slightly during the early stage of SPS (from 500 s to 1000 s). While during the intermediate stage when the temperature is over 1400 ℃, both of them are experiencing rapid densification process. However, the one whose pressure was intensified at 1600 ℃ seems to give faster shrinkage with entering the final SPS stage a bit earlier compared to the one whose pressure was previously increased to 60 MPa. The evolutions of relative density during the final SPS stage are pretty much the same for both cases. Introducing pressure at low temperatures may prevent the rearrangement of ceramic particles and impede densification [74], but the effect of this phenomenon seems to be negligible to the final density level as long as the holding time at the maximum processing temperature is considerable.

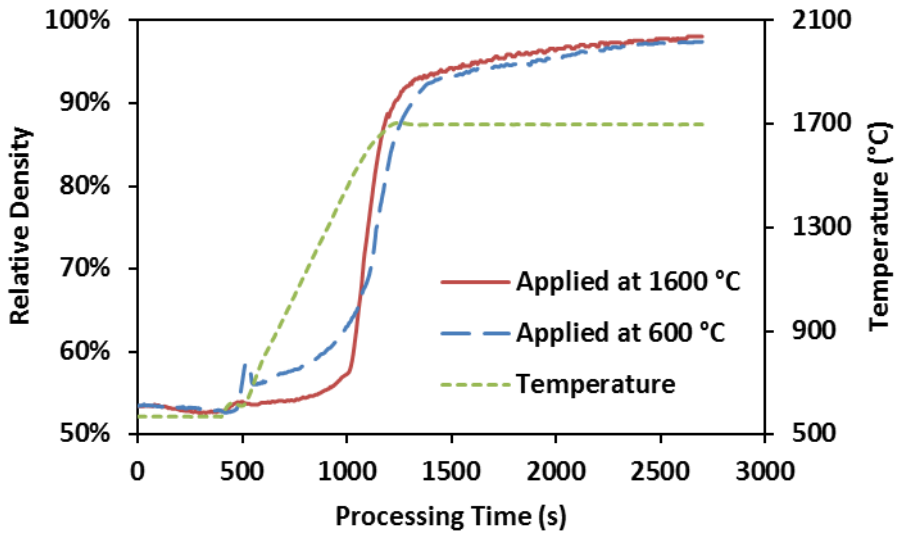

Figure 4.4 Comparison of densification kinetics under same temperature profile but different pressing occasions.

In regard to the annular shape graphite tooling, under different loading profiles, the mandrel appeared to be sustainable after several runs though it was considered as the most vulnerable component. The stability of the current tooling design is therefore validated. Nevertheless, the use of mandrel has brought geometric complexity into the tooling - specimen system, which could make a more intricate internal stress state than that in the SPS of cylindrical shape specimens. When processing a disk-like shape specimen, the tooling – specimen interaction mainly occurs between the die wall and the powder bed. While in the case of annular shape pellet, especially at an elevated processing temperature, the powder based specimen interacts with both the die wall and the thin mandrel actively through its viscoelastic deformation. To have a better understanding of the entire process, it is necessary to look into the stress distribution during SPS of annular shape ZrC via finite element simulation.

4.1.3 Stress distribution in SPS of annular shape ZrC

The COMSOL® Multiphysics software (COMSOL Inc., Burlington, MA, USA) was again used to implement the finite element simulation of stress distribution in SPS of annular shape ZrC pellet. The stress states of the porous specimen were given by the sintering constitutive equation while those of the tooling components were defined by the built-in modules. The different physics incorporated in the tooling and the specimens subdomains were lately coupled with the evolution of the velocity field during the simulation steps.

Due to the compatibility of the sintering constitutive stress - strain relationship, Equation (2.7) was not able to be directly applied to define the boundary conditions of a porous specimen subjected to uniaxial pressure in the COMSOL® modules. The stress - strain components in Equation (2.7) had to be inverted in order to obtain a strain - stress oriented expression that is physically-friendly to the simulation software. By writing Equation (2.7) explicitly using index notation, a series of linear equations were formed with individual stress and strain components as coefficients. By solving these equations, an expression which represents the strain rates in terms of the stress tensors, is obtained,

$$\dot{\varepsilon}_{ij} = \frac{(\sigma_{kk} - 3P_L)\delta_{ij}}{9\psi A_{cr} W^{m-1}} + \frac{\sigma_{ij} - \frac{1}{3}\sigma_{kk}\delta_{ij}}{\varphi A_{cr} W^{m-1}} \tag{4.1}$$

where σ_{kk} stands for either the trace of the stress tensor ($tr(\boldsymbol{\sigma})$) or the first stress invariant ($\boldsymbol{I}_1$), regardless of the coordinate system's orientation.

To simplify Equation (4.1), the mean hydrostatic stress tensor or the volumetric stress tensor, $p\delta_{ij}$, and the deviatoric stress tensor, σ_{ij}^{d}, are considered. In any pressure-assisted compacting process, these two tensors are given as the follows:

$$p\delta_{ij} = \frac{1}{3}(\sigma_{kk} - 3P_L)\delta_{ij} \tag{4.2}$$

$$\sigma_{ij}^{d} = \sigma_{ij} - \frac{1}{3}\sigma_{kk}\delta_{ij} \tag{4.3}$$

with P_L specially denotes the sintering stress of a porous body. Therefore Equation (4.1) can be alternatively expressed as,

$$\dot{\varepsilon}_{ij} = \frac{1}{A_{cr}W^{m-1}}\left(\frac{p\delta_{ij}}{3\psi} + \frac{\sigma_{ij}^{d}}{\varphi}\right) \tag{4.4}$$

the right-hand side of this equation consists of two types of stress tensors: one tends to change to volume of the stressed body while the other one tends to distort it.

It is worth noticing that the strain rate tensors are also presented in the expression of equivalent strain rate *W*, in terms of the volume change rate, $\dot{e}$, and the shape change rate, $\dot{\gamma}$, as denoted in Equation (2.9). In a non-linear viscous porous material, these two variables can be related to the mean hydraulic stress, p, and the effective shear stress, τ, respectively, as [125],

$$\dot{e} = \frac{p}{A_{cr}W^{m-1}\psi} \tag{4.5}$$

$$\dot{\gamma} = \frac{\tau}{A_{cr}W^{m-1}\varphi} \tag{4.6}$$

where τ can be expressed by the second stress deviator invariants ($\boldsymbol{J}_2$) as:

$$\tau = \sqrt{2\boldsymbol{J}_2} = \sqrt{\sigma_{ij}^d \sigma_{ji}^d} \tag{4.7}$$

in this way the equivalent strain rate, *W*, is rewritten as,

$$W = \left(\frac{1}{A_{cr}} \frac{1}{\sqrt{1-\theta}} \sqrt{\frac{p^2}{\psi} + \frac{\tau^2}{\varphi}} \right)^{\frac{1}{m}} \tag{4.8}$$

so that,

$$A_{cr} W^m = \frac{1}{\sqrt{1-\theta}} \sqrt{\frac{p^2}{\psi} + \frac{\tau^2}{\varphi}} = \sigma_{eff} \tag{4.9}$$

where σ_{eff} represents the effective stress in a porous medium.

Substituting Equation (4.8) and (4.9) into Equation (4.4) with considering $1/m = n$, to have,

$$\dot{\varepsilon}_{ij} = \left(\frac{1}{A_{cr}} \right)^n \left(\sigma_{eff} \right)^{n-1} \left(\frac{p\delta_{ij}}{3\psi} + \frac{\sigma_{ij}^d}{\varphi} \right) \tag{4.10}$$

by writing A_{cr} explicitly in the format of Equation (2.8), below equation is retrieved,

$$\dot{\varepsilon}_{ij} = \frac{A}{T} exp\left(-\frac{Q}{RT} \right) \left(\sigma_{eff} \right)^{n-1} \left(\frac{p\delta_{ij}}{3\psi} + \frac{\sigma_{ij}^d}{\varphi} \right) \tag{4.11}$$

the unit of parameter A turns out to be $K/(Pa^n \cdot s)$, which is the same as the one defined in Equation (2.8). Also, Equation (4.11) has the similar format as the general

power-law creep model (see also Equation (2.6)) but takes into account the behaviors of non-linear viscous porous material. The strain - stress oriented constitutive equation evaluates the creep strain rate of a porous body subjected to stress and temperature fields. This formulated equation can be coupled with the classic elasticity equations to represent the viscoelastic behaviors as well as to investigate the stress states in the porous specimen during pressure-assisted sintering process.

During SPS process, the porous specimen itself is subjected to both thermal and mechanical effects. The overall stress-strain relationship that the specimen experiences can be expressed by correlating the elastic deformation, the creep behavior and the thermal expansion phenomena as the follows:

$$\boldsymbol{\sigma} = \boldsymbol{C}_{el}(\boldsymbol{\epsilon} - \boldsymbol{\epsilon}_{cr} - \boldsymbol{\epsilon}_{th}) \tag{4.12}$$

where $\boldsymbol{C}_{el}$ is the stiffness tensor, $\boldsymbol{\epsilon}$ is the general elastic strain tensor based on the theory of elasticity, $\boldsymbol{\epsilon}_{cr}$ stands for the creep strain rate tensor integrated from its time derivative components which is equal to,

$$\dot{\boldsymbol{\epsilon}}_{cr} = \begin{pmatrix} \dot{\varepsilon}_r & 0 & \dot{\varepsilon}_{rz} \\ 0 & \dot{\varepsilon}_\theta & 0 \\ \dot{\varepsilon}_{rz} & 0 & \dot{\varepsilon}_z \end{pmatrix} \tag{4.13}$$

where $\dot{\varepsilon}_r, \dot{\varepsilon}_\theta, \dot{\varepsilon}_z$and $\dot{\varepsilon}_{rz}$ are from rewriting Equation (4.11) in cylindrical coordinates with respect to an axial-symmetric geometry. $\boldsymbol{\epsilon}_{th}$ represents the strain tensor caused by the thermal expansion of the material, as,

$$\boldsymbol{\epsilon}_{th} = \boldsymbol{\alpha}_{\boldsymbol{V}}(T - T_{ref}) \tag{4.14}$$

where $\boldsymbol{\alpha_V}$ is the coefficient of thermal expansion (CTE, $1/K$), T the current temperature and T_{ref} the reference temperature (K). All these equations have been implemented in the "Solid Mechanics" module in the COMSOL® software with redefining creep strain rate according to Equation (4.13) to evaluate the stress evolution in the specimen subdomain.

All the tooling components were set to undergo elastic deformation and thermal expansion during simulation as they are bulk graphite. There were no additional configurations regarding the tooling subdomain as the employed module was good enough to cover these physics. Other than analyzing the stress states, the finite element simulation was also aimed at predicting the specimen's porosity evolution. According to the mass conservation law, the specimen's volume change rate can be related to its porosity change as below,

$$\dot{e} = \dot{\varepsilon}_r + \dot{\varepsilon}_\theta + \dot{\varepsilon}_z = \frac{\dot{\theta}}{1-\theta} \tag{4.15}$$

and this differential equation can be implemented by employing "Coefficient Form PDE" module in the software.

An axial-symmetric geometry was again considered to facilitate the computation. Figure 4.5 shows the constructed geometric model with specifying the boundary conditions. A mandrel is running through the center of the punches as well as the specimen to ensure the annular geometry. An Axial load of 14.1 kN was applied at the top surface of the upper spacer which is equivalent to a pressure of 60 MPa acting on the specimen.

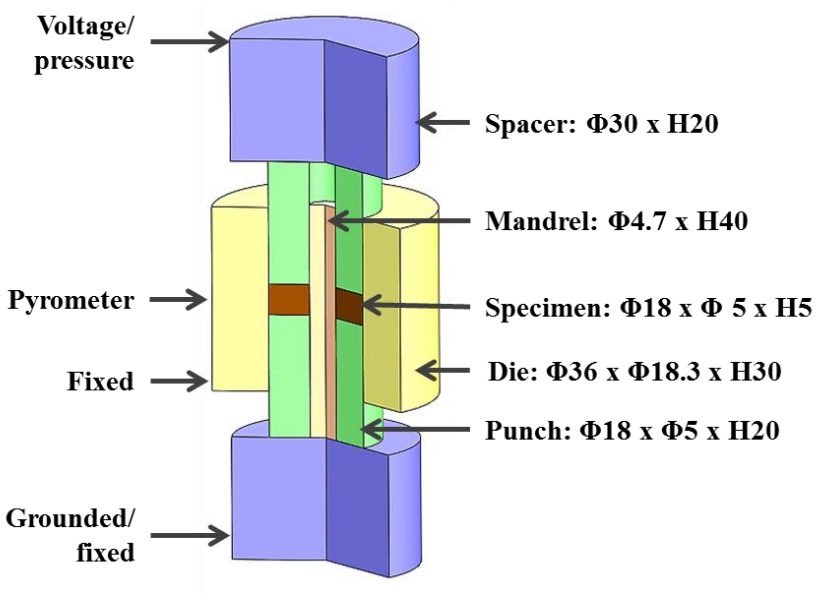

Figure 4.5 Geometric model for investigating stress distribution in SPS of annular shape ZrC. Boundary conditions and tooling dimensions (unit: mm) are also given.

Contact pairs were assigned to all interfaces where two objects are encountered in order to reflect their relative displacements introduced by the applied load. Both ZrC specimen and graphite were assumed as isotropic materials with thermal and electric properties being set as the same as what have been used in CHAPTER 3. The power-law creep coefficients of ZrC were assigned following the values presented in Table 3.6. Initial values and material constants employed in the simulations are listed in Table 4.1.

SPS machine logged voltage readings were converted to their root mean square values and interpolated with time to provide continuous inputs for the entire modeling process. The temperature during the simulation was evaluated at the control point at where the temperature measuring pyrometer has been focused and a maximum

temperature of 1700 ℃ at the die surface was considered. With regard to the finite-element meshing, the relative simplicity of such models allowed the selection of a physics-defined, free-triangular mesh, with "extra fine" size, as the COMSOL® classification states, for a total of 1206 domain elements.

Table 4.1 Initial values and material constants used in the simulations

Parameter	Value	Description
$\boldsymbol{\alpha_V}$, ZrC, (*1/K*)	6.7e-6	Thermal expansion coefficient
$\boldsymbol{\alpha_V}$, graphite, (*1/K*)	3e-6	Thermal expansion coefficient
$\boldsymbol{\theta_0}$	0.4	Initial porosity
$\boldsymbol{E}$, ZrC, (*MPa*)	389	Young modulus
$\boldsymbol{E}$, graphite, (*MPa*)	10	Young modulus
$\boldsymbol{\nu}$, ZrC	0.19	Poisson's ratio
$\boldsymbol{\nu}$, graphite	0.26	Poisson's ratio
$\boldsymbol{T_{ref}}$, (*K*)	298.14	Reference temperature
$\boldsymbol{V_{max}}$, (*V*)	4.8	Maximum voltage

Typical physics included in an SPS process such as Joule heating, pressing and densification were fully coupled in the employed software. The simulation was time-dependently conducted for a processing time span of 2700 s with a time step of 20 s, including a 1500 s dwelling stage at the maximum temperature. The Von Mises stress was selected to demonstrate the stress distribution in the tooling - specimen system during SPS of annular shape ZrC pellets as it has been commonly used as the yield criterion of materials.

Figure 4.6 maps the distribution of the Von Mises stress at the initial, the intermediate and the final stages of the simulated SPS process. One can see that the stress concentration occurs all the time at the specimen - mandrel interface as well as at the specimen - die interface. The stress concentration at the specimen - mandrel interface appears to be more pronounced than the other, indicating that the fragile mandrel becomes the most vulnerable part of the entire tooling setup.

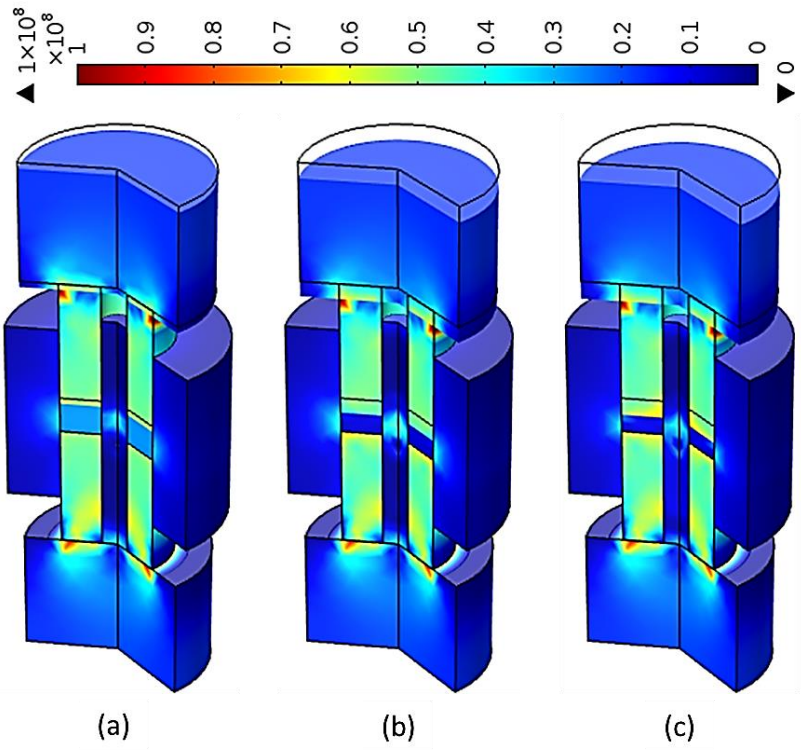

Figure 4.6 Simulation results: Von-Mises stress distribution at the: (a) beginning; (b) intermediate; and (c) final stages of the SPS of annular shape ZrC (unit: Pa).

Since the excessive stress concentration at the mandrel - specimen interface may cause potential failure of the entire system in real experiments, it is better to evaluate the magnitude of the stress concentration using the developed modeling

framework if extremely processing conditions are considered. Also, the simulation was able to show the movement of the punch - specimen entity along the axial direction as a result of the volume shrinkage of the specimen. This concurrent displacement field was not reported in other similar simulation studies [123, 177] as the specimen was considered as incompressible.

The evolution of the Von Mises stress in the mandrel during the entire simulation was shown in Figure 4.7. It is significantly erratic but overall exhibits an increasing trend. The most unstable stress state emerges abruptly from 1100 - 1200 s. This time span is exactly corresponding to the occurrence of the rapid densification, as what have been shown in Figure 4.4. One can see that the Von Mises stress oscillates up and down with sharp amplitudes, which indicates the mandrel is undergoing a metastable stress state and the failure of the mandrel is most likely to happen during such a period of time.

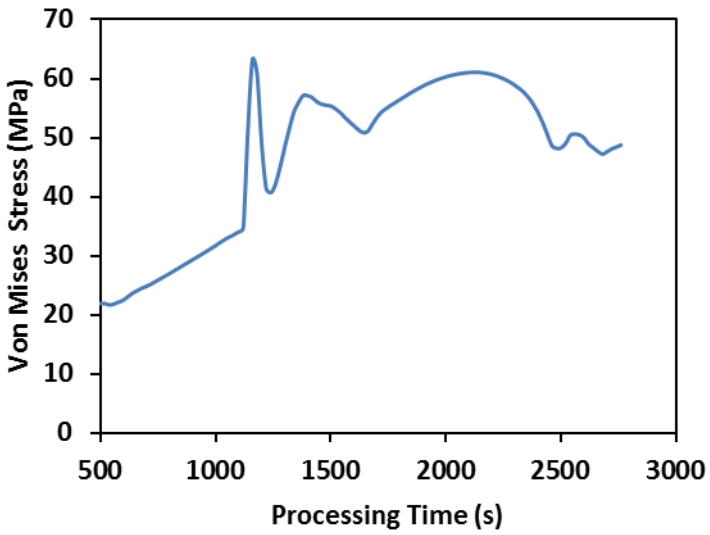

Figure 4.7 Simulation results: Von Mises stress in the mandrel *vs.* processing time.

The peak Von Mises stress from the simulation is evaluated to be around 65 MPa. It is a bit below the reported flexural strength of graphite at room temperature (97 MPa, see also CHAPTER 3), which to some extent explains the survival of the mandrel in the present study. However, stress oscillation is still harmful to the high aspect ratio mandrel. To avoid mandrel failure, one should carefully examine its service conditions before or after experiments though it was subjected to moderate processing conditions.

The viscoelastic behavior of the porous ZrC specimen during SPS largely contributed to the generation of significant stress oscillations in the mandrel. At low temperatures, the interactions between the specimen and the mandrel were elastic. Once the creep was activated at elevated temperature, the porous ZrC body started acting viscously on the mandrel. The onset of the plastic flow first caused a sudden increase of stress but soon the shrinkage of the specimen eliminated part of the stress build-up. Due to the continuously applied pressure, the viscous stress came back again with a lower magnitude and then partially released, so on and so forth till the completion of the powder consolidation process where no more viscous flow can literally occur. Both the amplitude and the frequency of von Mises stress oscillation were attenuating as processing time evolved due to the decrease of specimen's effective viscosity.

Additional attentions were particularly paid to the stress generated at the specimen - mandrel interface as the specimen might also experience an unstable stress state during the SPS process. The mean hydrostatic stress, which is one-third of the

first invariant of the stress tensor, was used to evaluate the average pressure acting on the interface as a result of the specimen's deformation. The hydrostatic stress and porosity evolutions from the simulation are plotted in Figure 4.8. The mean hydrostatic stress exhibits an overall increasing trend as porosity decreases but it appears to be less fluctuating compared to the Von Mises stress (see also Figure 4.7) during the fast densification stage. The hydrostatic stress slightly drops down near the end of the simulation which indicates that the amount of viscous flow is reduced as the specimen itself has been consolidated into high density. The localized hydrostatic stress evolution is in accordance with the Von Mises stress distribution in the investigated region (see also Figure 4.6).

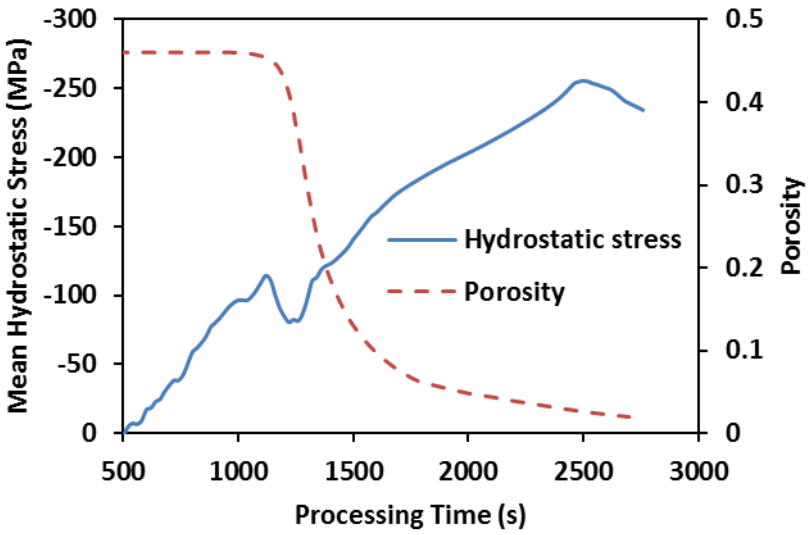

Figure 4.8 Simulation results: Mean hydrostatic stress at the specimen - mandrel interface as well as porosity *vs.* processing time.

Also, the finite element model was shown to be able to calculate the porosity evolution over the processing time and the simulated results are in good agreement

with the experimental data (see also Figures 4.2 and 4.3). Therefore the modeling provides an efficient way to correlate the densification kinetics and the internal stress state in the SPS of annular shape ZrC under given processing conditions.

Both the simulated Von Mises stress and mean hydrostatic stress have displayed increasing trends towards the processing time in the vicinity of mandrel - specimen contact even though these two types of stresses are propagating with different magnitudes. These phenomena are critical to the stress state of the mandrel as well as to that of the material around the mandrel. To avoid tooling or specimen failure, one should carefully consider the thermomechanical interaction between the mandrel and specimen before experimental implementations. Moreover, this fully coupled modeling framework can be further utilized in the optimization of loading modes to examine the stability of the graphite tooling as well as to regulate specimens with desired porosities and structures.

4.2 Annular Shape Composites for SPS Tooling Applications

As reported in CHAPTER 2, the SPS consolidation of ZrC can benefit from applying high pressure. However, the regular single-walled graphite SPS tooling, especially the die, is not able to withstand the intensified die - powder mechanical interactions due to its strength. The double-die setup could be a tentative option to archive high pressure, but one has to sacrifice the effective specimen size and to deal with extra thermal non-uniformity. Since it has been shown that the SPS pressure level significantly influences the densification kinetics, to come up with a permanent solution, it is necessary to develop alternative tooling materials for high pressure SPS

regimes. Qualified candidates should satisfy certain requirements. First of all, the selected material must be stronger than graphite so it can survive at elevated temperature under high pressure. Also, it has to be electrically conductive to flow the current and its electrical resistivity should be comparable to that of graphite to take advantages of Joule heating effect. Again, it is supposed to have considerable thermal properties in order to serve as heating elements.

The material considered in the present study is a ceramic composite consisting of SiC and ZrB_2. Previous studies have reported that the SPS-processed SiC-ZrB_2 ceramic composites possess high flexural strength (~1 GPa) and good electrical resistivity (~ $10^{-3}\,\Omega \cdot cm$) at room temperature [178]. At elevated temperatures, this kind of composite also exhibits an excellent flexural strength [179]. In addition, as suggested by Zimmermann *et al*., the thermal conductivity and heat capacity of the SiC-ZrB_2 composite are close to those of graphite and showing similar evolution trends toward the temperature [180]. Upon the selection of tooling material, the next step is to implement the single-walled die geometry, or in other words to produce an annular shape SPS die. In this consideration, the experimental procedures employed in the SPS of annular shape ZrC pellet are practically adapted to process SiC-ZrB_2 composite powder with achieving similar geometry.

4.2.1 SiC-ZrB_2 composite tooling components produced by SPS

Silicon carbide powder (SiC, 99.9% pure, < 1 μm average, Materion Advanced Material Group, Milwaukee, WI, USA) and zirconium diboride powder (ZrB_2, 99.5%

pure, -325 mesh, Materion Advanced Material Group, Milwaukee, WI, USA) were employed as starting materials. The volume percentage of ZrB_2 in the target powder composite was set to 40% as it has been reported to be the optimal ratio according to Ref. [178]. The weighted SiC and ZrB_2 powders were first mixed with tungsten carbide milling balls (Ø1 mm, Norstone Inc., Bridgeport, PA, USA) in a nylon jar (80 ml, MTI Corp., Richmond, CA, USA). The mass ratio of powder to ball was 1:10. Ethyl alcohol (95 *vol*.%, Fisher Scientific Inc., Hampton, NH, USA) was poured into the jar to blend with the powder/ball mixture. Then the jar was sealed and put onto a roll jar mill rotating for 8 hours at a fixed speed of 30 RPM to homogenize the particle distribution in the slurry.

The ethyl alcohol was volatilized by placing the slurry in a fume hood (PURAIR-P5-36-XT, AirScience USA LLC., Fort Myers, FL, USA) for 8 hours and the residual moisture was removed by drying the mixture in a baking oven (AccuTemp-09, Across International, Livingston, NJ, USA) for another 8 hours. The powders and the milling balls were separated by test sieves (Aperture 250 - 150 μm, Endecotts Ltd, London, England). The theoretical density of the mixed powder was calculated to be 4.362 g/cm^3 based on the law of mixture while the helium pycnometer suggested an absolute density of 4.358 g/cm^3. The XRD (X'pert Pro, PANalytical B.V., Almelo, the Netherlands) of the composite powder is given in Figure 4.9, one can see there are no other detectable phases presenting besides the two major ones.

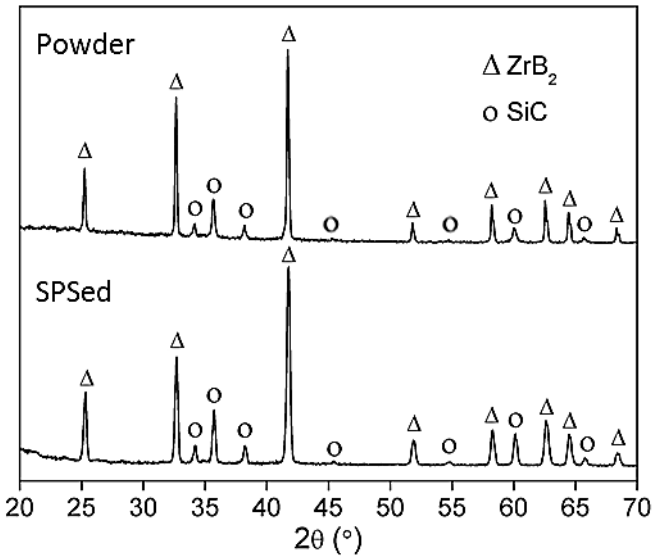

Figure 4.9 XRD patterns of the homogenized SiC-ZrB_2 powder and the SPS-processed composite.

The schematics of the annular shape SPS tooling used for processing SiC-ZrB_2 composite powders was similar to the one illustrated in Figure 4.1 except the punch opening and the mandrel diameter being enlarged to 8 mm and 7.7 mm, respectively. This modified graphite tooling was used to produce an annular shape composite die with nominal outer and inner diameters of 18 mm and 8 mm, respectively. The SiC-ZrB_2 composite punches were produced by regular 8 mm SPS tooling (I-85 graphite, Electrodes Inc., Santa Fe Springs, CA, USA) to have a diameter of 7.7 mm in correspondence to the dimensions of the composite die.

The maximum SPS processing temperature was set to 1600 ℃. The heating rate was 100 ℃/min from 600 ℃ to 1200 ℃ and then 50 ℃/min to 1600 ℃. A digital pyrometer was used to evaluate the temperature at the outer die surface. An axial pressure of 60 MPa was applied at the moment when the temperature reaches 600 ℃

and held consistently during the rest of the sintering process. The holding time at the peak temperature was 10 min. To minimize the impacts of the mismatch of thermal expansion between the composite specimen and the graphite tooling, the cooling was controlled from 1600 ℃ to 800 ℃ at 100 ℃/min. Experiments were conducted within argon atmosphere. The processing temperature, applied force and ram displacement were automatically logged by the equipped computer.

The densities of the obtained SiC-ZrB_2 composite tooling components were measured using both geometric and Archimedes methods in order to ensure the reliability of the measurements. The real-time densification kinetics was plotted taking into account the absolute height change of the specimen during SPS, in which the variations caused by the thermal expansion of the tooling components were taken away from the original machine-logged readings. The evolution of relative density in SPS of annular shape composite die is shown in Figure 4.10. As one can see, the densification has evolved into the final stage during the isothermal holding and a relative density of ~ 98% was achieved at the end of the SPS process. The height of the final annular shape component was about 8 mm which to some degree evidences the tooling capacity for producing thick products other than disks or pellets.

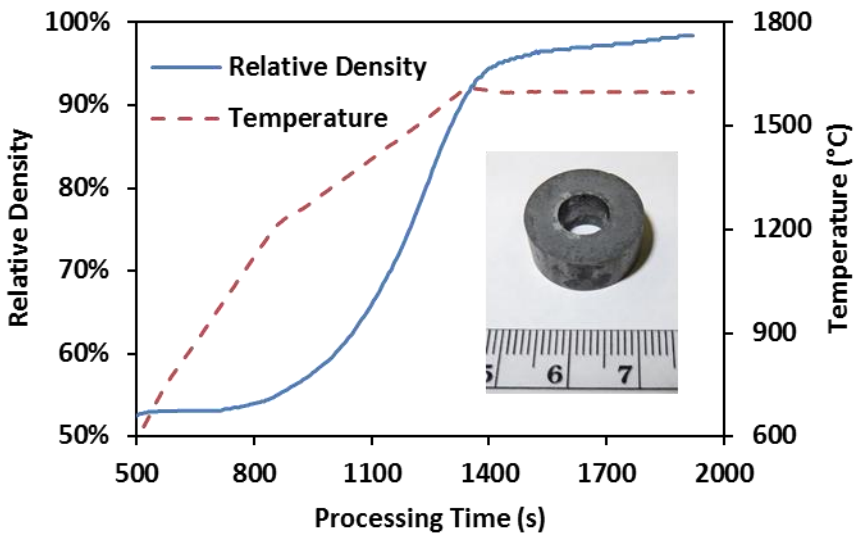

Figure 4.10 Relative density and temperature evolutions in SPS of SiC-ZrB_2 composite die under 60 MPa.

One of the obtained composite components was fractured at the room temperature in order to characterize its microstructures and phase compositions after sintering. The XRD pattern of the SPS-processed composite is compared to that of the starting powder in Figure 4.9. These two sets of diffractive peaks appear to be in good agreement with each other, indicating that the major phases of the mixed powder are properly retained in the consolidated composite. EDS (X-Max-50 detector, Oxford Instruments, Concord, MA, USA) was used along with SEM (Quanta 450, FEI Co., Hillsboro, OR, USA) to examine the fractured surface of the sintered composite. As shown in Figure 4.11, ZrB_2 (bright regions) is uniformly dispersed in the SiC matrix (dark regions), suggesting that the powder homogenization was sufficient. Also, from the SEM image, the examined specimen only exhibits a small quantity of pores sitting

at the triple junctions of the adjacent grains. This observation is in accordance with the experimentally measured densification level (see also Figure 4.10).

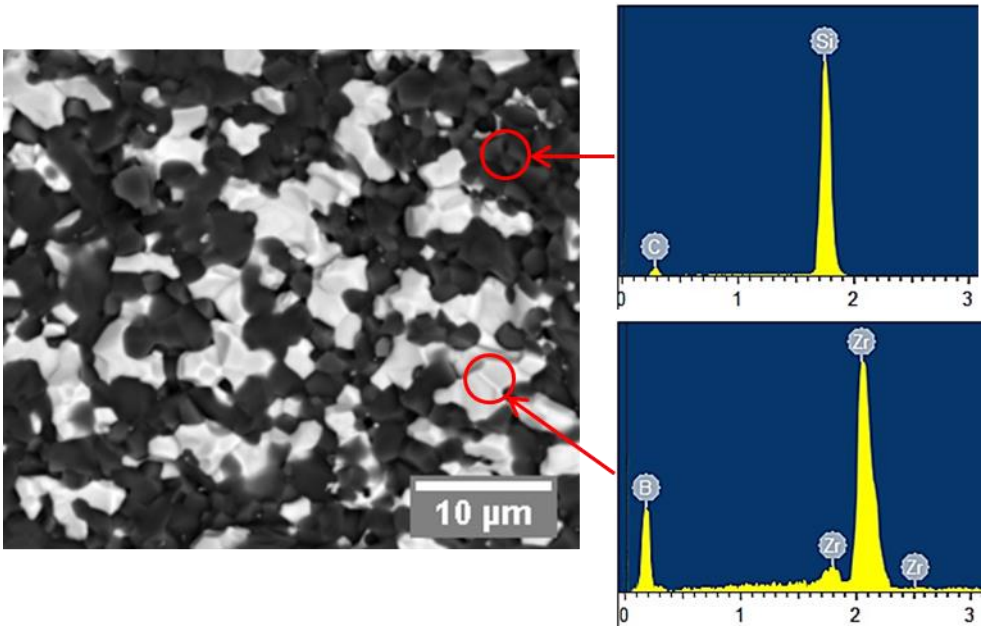

Figure 4.11 Backscattering SEM image of the fractured surface of SPS-processed SiC-ZrB_2 composite with presenting phase constituents.

4.2.2 SPS of powder materials using the SiC-ZrB_2 composite tooling

During SPS process, the applied axial pressure can be transmitted into the radial stress acting on the die wall via the deformation of the powder specimen. An SPS die is supposed to be able to sustain the radial impaction at the maximum SPS temperature to secure the entire sintering process. To determine whether the SPS-fabricated composite components are capable or not, the SiC-ZrB_2 punches and die were first tested in SPS of alumina powder with introducing a high level of axial pressure. Approximately 0.3 g alumina powder (Al_2O_3, 99.99% pure, -325 mesh, Materion Advanced Material Group, Milwaukee, WI, USA) was used for the test run.

The tooling configuration used for the test is illustrated in Figure 4.12. The composite punches were used to hold the powder specimen in the SiC-ZrB_2 composite die. Two 18 mm graphite spacers (I-85 graphite, Electrodes Inc., Santa Fe Springs, CA, USA) were attached to the punches to transmit the load from the machine's hydraulic loading unit. Also, graphite foils were inserted between tooling components to improve the contact quality between them.

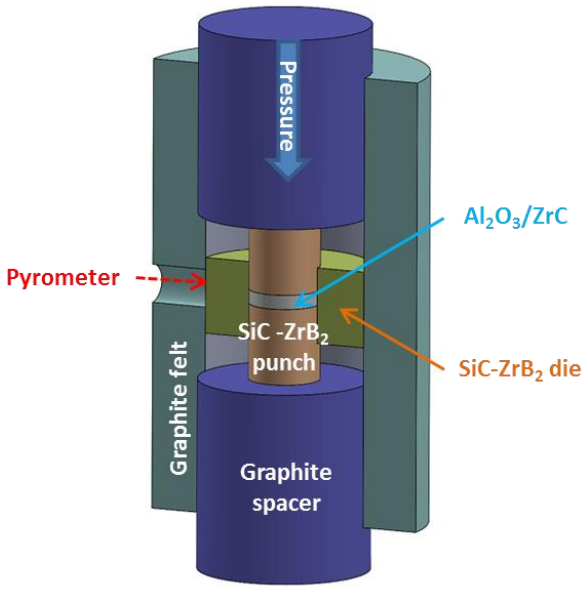

Figure 4.12 Schematics of the SPS tooling setup using composite punches and die.

The test runs were carried out using the same SPS machine with a maximum processing temperature of 1400 °C. In order to follow the commonly utilized SPS conditions, the heating rate was set to 100 °C/min after 600 °C. Digital pyrometer was used to measure the temperature of the die. The axial pressure was initially kept at the minimum level (~ 80 MPa). When the target testing temperature has arrived, the axial pressure was increasing at a constant rate of 10 MPa/min during the holding period.

Upon the completion of each pressure increase cycle (1 min), an extra 1 min holding time was given before the start of next cycle to stabilize the pressure distribution. The holding time at 1400 °C was 25 mins in order to give sufficient time for pressure intensification steps.

The spacers and the tooling components were wrapped by thick graphite felt to reduce thermal radiation except the opening located at the die surface for temperature measurement. The SPS machine was operated under the argon atmosphere protection mode during the test run. If the composite tooling had failed during the test, the heating and loading units of the SPS machine would have been shut off immediately. Then the axial pressure right before the shutoff could be recognized as the maximum stress that the tooling can sustain at the selected processing temperature. If not, the pressure should be increased to the next level. To avoid any broken pieces dropping down to the chamber, a graphite pan made out of graphite paper was placed under the bottom spacer.

The pressure evolution during the SPS run was demonstrated in Figure 4.13. As one can see, the axial pressure was gradually increased from 80 MPa to 210 MPa when holding time propagates at 1400 °C. Also, fully dense alumina specimens with an average grain size less than 5 μm were obtained (see the SEM image in Figure 4.13). In addition, the composite tooling survived from imposing such a processing profile. The sustainable pressure of the composite tooling is much higher compared to that of the commonly used graphite tooling, suggesting that the SiC-ZrB_2 could be a promising candidate material for high pressure SPS tooling components.

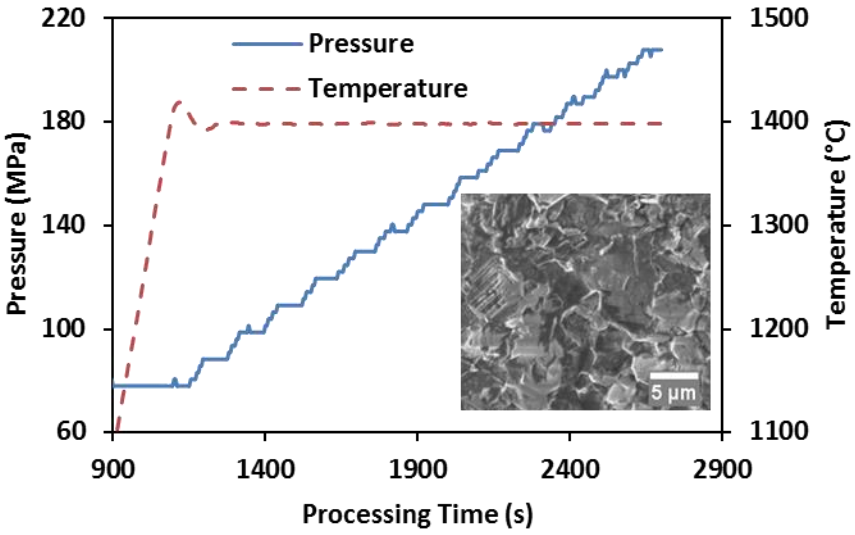

Figure 4.13 Pressure evolution in composite tooling SPS of alumina at 1400 ℃ with presenting the obtained microstructure.

After evaluating the pressure level that the composite tooling could resist through SPS of alumina powder, the tooling was used in the SPS consolidation of ZrC powder as it is the target material of this study. As studied in CHAPTER 2, the regular SPS-processed ZrC specimens not only own high relative densities but also possess large grains due to long term holding at high temperature. It is well-known that large grains to some extent compromise the strength of materials. To reduce grain size in powder consolidation process, one needs to either lower the processing temperature or shorten the holding time. Therefore, the composite tooling was very logically employed here to achieve high pressure in order to compensate the temperature and holding time requirements in SPS of ZrC.

The high pressure SPS of ZrC was conducted at a maximum processing temperature of 1500 ℃. The heating rate was set to 100 ℃/min during the ramping

stage and the pressure was kept at 190 MPa throughout the entire holding stage (9 min). The obtained ZrC specimen was measured to have a relative density of 96.3%, which is comparable to those prepared by regular SPS at 1700 ℃ or higher temperature under moderated pressures (see also Figure 2.4). The microstructure of the high pressure SPS-processed ZrC specimen is shown in Figure 4.14, one can see that, compared to the microstructures in Figure 2.10, smaller grains are observed in the current case. Also, less intra-granular pores are exhibited, indicating the high temperature pore formation mechanism [130] was attenuated to some degree as a result of the lower processing temperature.

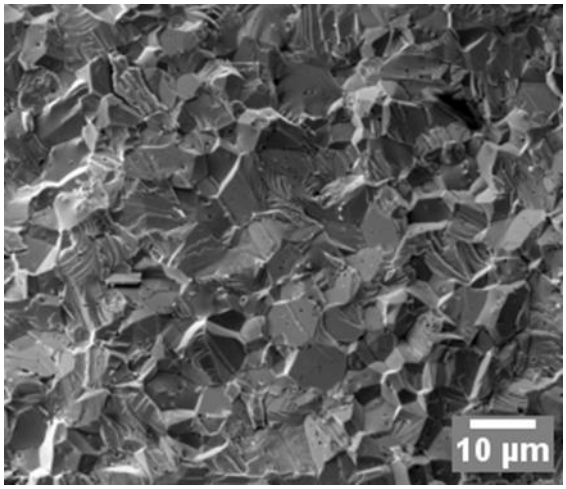

Figure 4.14 SEM image of ZrC specimen processed by high pressure SPS using composite tooling.

Although the capacity of the present SPS device limits the attainable size of the annular shape composite die, the experimental outcomes still can be scaled up for advanced SPS tooling design in the future. The pressure evolution in the volume of the composite die at room temperature can be explained by the thick-walled cylinder

equations. However, at high temperature, the internal stress is incorporated with the creep of the powder specimen as well as the interaction between the powder and the tooling material. These mechanisms still need to be elaborated.

One more experiment was carried out to determine the ultimate axial pressure that the die can sustain. During such a test, instead of raising the axial pressure step by step, the pressure was continuously increased to bring the composite die into failure through the internal pressure buildup from the deformation of the powder-based specimen. The composite tooling was also tested with ZrC powder at 1500 °C using the same SPS machine. Axial pressure intensification was imposed during the isothermal holding stage. The axial pressure upon the crack of the composite die was recorded to be 217.6 MPa.

The composite SPS tooling cracked under the SPS conditions gives different micromorphology compared to the one fractured at room temperature. A layer of pebble-like dots was observed on top of the ZrB_2 phase after being ruptured under SPS conditions (Figure 4.15 a), while the fracture occurred at room temperature only consists of the two major phases (Figure 4.15 b, see also Figure 4.11). Energy dispersive X-ray has detected a certain amount of oxygen existing in these dots. The formation of the oxidation layer can be most likely attributed to the reaction between local discharges and residual oxygen due to the sudden breakdown of electric current. This transient discharging also influenced the morphology of SiC phase as it appears to be similar to the one obtained by Olevsky *et al.* when conducting flash spark plasma sintering of pure SiC powder [181].

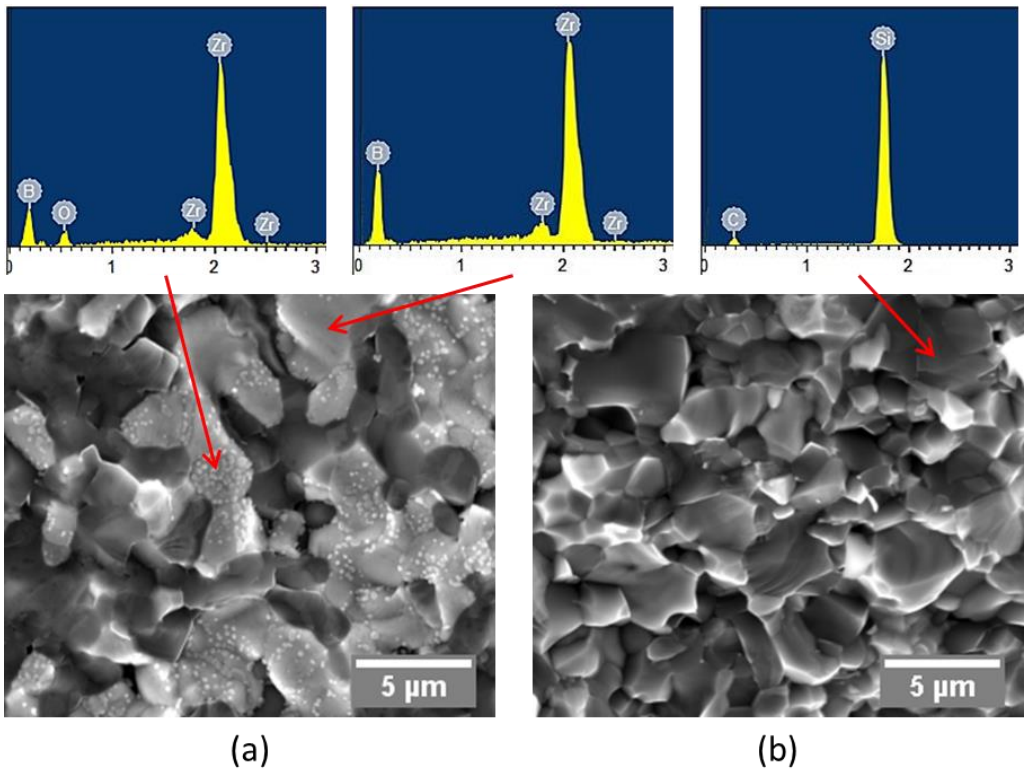

Figure 4.15 SEM images of SiC-ZrB2 composite: (a) Fractured under SPS conditions; (b) Fractured at room temperature.

4.3 Analytical Investigation of Porosity Evolution in the Swelling of Porous Annular Shape Pellet

ZrC was selected in the present study as it can serve as a surrogate material for high temperature nuclear fuel, in particular the uranium carbide (UC) because they possess similar thermal and mechanical properties as well as share same cubic crystal structure and space group [182, 183]. Therefore the experimental and simulating steps that have been carried out to study the SPS of annular shape ZrC pellets could be lately transplanted into the production of annular shape UC fuel pellets. However, the feasibility of applying such a geometry is necessary to be evaluated before performing

any further fabrication process, especially how an annular shape fuel pellet responses when subjected to irradiation-induced swelling phenomena.

The swelling of fuel rods and pellets during the nuclear reaction can be either caused by the fission gas precipitation or by the thermally-induced deformation [184-186]. Fuel pellets are usually consolidated from powder-based materials. Most of them are disk-like shape plates with high relative densities [187]. This kind of geometry, although is easy to be produced, potentially limits its capacity of accommodating the swelled volume. When a highly dense pellet subjected to the swelling phenomenon, only a small portion of the swelled substance can flow into the residual pores while most of it contributes the volume expansion of the fuel matrix. As a result, the fuel pellet usually cracks into fragments after service [188].

The limitation of the cylindrical shape disk inspires the consideration of an annular shape pellet. The central hole of the pellet is designed to accommodate the swelled volume to some extent. Additionally, the pellet is supposed to have a certain porosity as the porous structure also can be the sinks of the swelled volume. To demonstrate the potential applicability of this special design, a preliminary attempt is to investigate the porosity evolution of a porous annular shape pellet subjected to volume swelling. Since swelling is opposite to sintering in the physical senses, it is very logically to apply sintering equations to describe the swelling phenomena. Analytical equations are derived based on the constitutive behaviors of the porous material to correlate the porosity change with the volume swelling. Numerical

solutions of these equations are used to characterize the relationship between the geometric parameters and the accommodation capacity of the annular shape pellets.

4.3.1 Analyses on two different swelling stages

A representative annular shape pellet is illustrated in Figure 4.16, its inner and outer radii were set to be "a" and "b", respectively. The height of this pellet was not taken into account in the analytical study due to the symmetry. Since the fuel pellets are actually stacked together in reality, both the top and the bottom surfaces of the individual pellet were assumed to be fixed along the axial direction to simplify the boundary conditions. Also, the outer wall of the pellet was confined along the radial direction by assuming the existence of the cladding. While the inner wall was free to move along the radial direction.

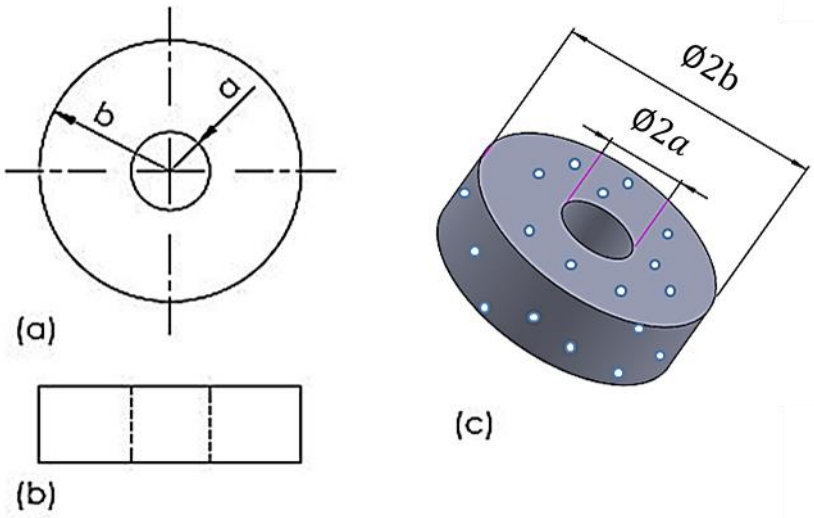

Figure 4.16 Schematics of a representative annular pellet: (a) Top view; (b) Front view; (c) Isometric view.

The sources of swelling were assumed from the mechanical side only such as the flow and the expansion of the substance. The swelling of the fission products will be discussed in the next section. Based on the symmetric properties and the boundary conditions of the geometric model, the continuity equations of the volume change rate, $\dot{e}$, of an annular shape pellet subjected to a velocity field can be written in cylindrical coordinate system as follows [189];

$$\dot{\varepsilon}_r = \frac{\partial V_r}{\partial r}, \qquad \dot{\varepsilon}_\varphi = \frac{V_r}{r}, \qquad \dot{\varepsilon}_z = 0 \tag{4.16}$$

$$\dot{e} = \dot{\varepsilon}_r + \dot{\varepsilon}_\theta + \dot{\varepsilon}_z = \frac{\partial V_r}{\partial r} + \frac{V_r}{r} = \frac{1}{r}\frac{\partial}{\partial r}(rV_r) \tag{4.17}$$

where V_r is the velocity component along radial direction and r is the radial coordinate.

Equation (4.17) can be integrated with respect to r to have,

$$V_r = \frac{1}{2}\dot{e}r + \frac{B}{r} \tag{4.18}$$

where B is the constant of integration which can be determined by solving Equation (4.18) at $V_{r=b} = 0$,

$$B = -\frac{1}{2}\dot{e}b^2 \tag{4.19}$$

therefore

$$V_r = \frac{1}{2}\dot{e}\left(r - \frac{b^2}{r}\right) \tag{4.20}$$

also,

$$V_{r=a} = \dot{a} = \frac{1}{2}\dot{e}\left(a - \frac{b^2}{a}\right) \tag{4.21}$$

$$\dot{\varepsilon}_r = \frac{1}{2}\dot{e}\left(1 + \frac{b^2}{r^2}\right) \tag{4.22}$$

$$\dot{\varepsilon}_\theta = \frac{1}{2}\dot{e}\left(1 - \frac{b^2}{r^2}\right) \tag{4.23}$$

According to the mass conservation law, the volume change rate of a porous body, $\dot{e}$, can be written in terms of its porosity, θ, and the theoretical density of the substance itself (the porous skeleton), ρ_T, as [190],

$$\dot{e} = \frac{\dot{\theta}}{1-\theta} - \frac{\dot{\rho}_T}{\rho_T} \tag{4.24}$$

Based on the above-derived expressions, two stages were considered to describe the swelling process: i) The swelled substance is assumed to first fill up the central hole under the Laplace stress; ii) Upon the closure of the large central hole ($a = 0$), the excessive substance starts flowing into the internal pores to introduce the densification of the substance. Since these two stages incorporate different physical phenomena, they were analyzed separately but were combined to elucidate an overall swelling behavior lately.

During the first swelling stage, the theoretical density of the substance was set to remain constant to give, $\dot{\rho}_T = 0$. The volume swelling was considered as a result of the increase of the substance's apparent volume. Under such an assumption, the substance's volume change rate, $\dot{e}$, follows below expression,

$$\dot{e} = \frac{\dot{\theta}}{1-\theta} = \frac{\dot{\lambda}}{\lambda} \tag{4.25}$$

where λ is defined as the normalized volume, represents the ratio between the current volume and the initial volume of the substance.

Then the equivalent strain rate in this case, *W*, is obtained by substituting Equations (4.22) and (4.23) into Equation (2.9), we have,

$$W = \frac{|\dot{e}|}{\sqrt{1-\theta}} \sqrt{\frac{1}{6}\varphi\left[1+3\left(\frac{b^2}{r^2}\right)^2\right]+\psi} \tag{4.26}$$

therefore the stress which causes the swelling along the radial direction, according to the constitutive low of porous materials (see also Equation (2.7)), can be written in cylindrical coordinate system, as,

$$\sigma_r = A_{cr}|\dot{e}|^m \left(\frac{\frac{1}{6}\varphi\left[1+3\left(\frac{b^2}{r^2}\right)^2\right]+\psi}{1-\theta}\right)^{\frac{m-1}{2}} \left[\frac{1}{6}\varphi(1+3\frac{b^2}{r^2})+\psi\right] + P_L \tag{4.27}$$

taking into account that $\sigma_{r=a} = 0$, and writing ψ and φ explicitly in terms of porosity, θ, (see also Equations (2.10)and (2.11)), below expressions are obtained,

$$A_{cr}|\dot{e}|^m \left(\frac{\frac{1}{6}\varphi\left[1+3\left(\frac{b^2}{a^2}\right)^2\right]+\psi}{1-\theta}\right)^{\frac{m-1}{2}} \left[\frac{1}{6}\varphi(1+3\frac{b^2}{a^2})+\psi\right] = -P_L \tag{4.28}$$

so that,

$$|\dot{e}|^m = \frac{-P_L}{A_{cr}(1-\theta)^{\frac{1-m}{2}}\left(\frac{1}{6}\varphi\left[1+3\left(\frac{b^2}{a^2}\right)^2\right]+\psi\right)^{\frac{m-1}{2}}\left[\frac{1}{6}\varphi(1+3\frac{b^2}{a^2})+\psi\right]} \tag{4.29}$$

The Laplace stress, P_L, largely depends on the materials itself and can be recognized as the stress required to stop the free sintering of the same material with same porosity but a cylindrical shape. In this consideration, P_L was determined by applying similar procedures that have been used to derive Equation (4.29). By assuming there is no shape change in the disk-like counterpart ($\dot{\gamma}' = 0$), the equivalent strain rate, W', and the resulting "anti-sintering" stress, $P_L{}'$, are retrieved as follows:

$$W' = \frac{1}{\sqrt{1-\theta}}\sqrt{\varphi\dot{\gamma}'^2+\psi\dot{e}'^2} = \sqrt{\frac{\psi}{1-\theta}}\left|\dot{e}'\right| \tag{4.30}$$

$$P_L{}' = -A\left|\dot{e}'\right|^m\left(\frac{\psi}{1-\theta}\right)^{\frac{m-1}{2}}\psi = -A\left|\frac{\dot{\lambda}'}{\lambda'}\right|^m\left(\frac{\psi}{1-\theta}\right)^{\frac{m-1}{2}}\psi \tag{4.31}$$

where $\dot{e}'$ is the volume change rate in the porous disk, and λ' is the normalized volume of this disk with $\dot{\lambda}'/\lambda' = \dot{e}'$. Since it has been assumed that $P_L = P_L{}'$, Equation (4.31) is substituted back into (4.29) to have the following equations:

$$\dot{e} = \frac{\left|\frac{\dot{\lambda}'}{\lambda'}\right|}{\left(\frac{1}{6}\frac{\varphi}{\psi}\left[1+3\left(\frac{b^2}{a^2}\right)^2\right]+1\right)^{\frac{m-1}{2m}}\left[\frac{1}{6}\frac{\varphi}{\psi}\left(1+3\frac{b^2}{a^2}\right)+1\right]^{\frac{1}{m}}} \tag{4.32}$$

$$\dot{\theta} = \frac{d\theta}{dt} = \frac{\left|\frac{\dot{\lambda}'}{\lambda'}\right|(1-\theta)}{\left(\frac{1}{6}\frac{\varphi}{\psi}\left[1+3\left(\frac{b^2}{a^2}\right)^2\right]+1\right)^{\frac{m-1}{2m}}\left[\frac{1}{6}\frac{\varphi}{\psi}(1+3\frac{b^2}{a^2})+1\right]^{\frac{1}{m}}} \tag{4.33}$$

The volume change rate of the cylindrical shape disk, $\dot{\lambda}'/\lambda'$, has been experimentally measured to be 1.17 in 3.2 $\times 10^7$ seconds (one year), by series of real in-plant experiments. By solving a system of differential equations (Equations (4.21), (4.32) and (4.33)), the porosity evolution during the first stage of swelling can be evaluated with respect to time as long as the inner diameter of the annular pellet is larger than zero ($a > 0$, the existence of a central hole).

On the other hand, if we assume that both the annular pellet and the cylindrical disk have same volume change rate under swelling process, for example $\dot{e} = \dot{e'}$ or $\dot{\lambda}/\lambda = \dot{\lambda}'/\lambda'$. The relationship between the porosity and the normalized volume can be then simplified as,

$$\frac{d\theta}{d\lambda} = \frac{\frac{1}{\lambda}(1-\theta)}{\left(\frac{1}{6}\frac{\varphi}{\psi}\left[1+3\left(\frac{b^2}{a^2}\right)^2\right]+1\right)^{\frac{m-1}{2m}}\left[\frac{1}{6}\frac{\varphi}{\psi}\left(1+3\frac{b^2}{a^2}\right)+1\right]^{\frac{1}{m}}} \tag{4.34}$$

therefore the porosity evolution during the first stage of swelling can be evaluated with respect to the volume change by solving a system of differential equations (Equations (4.21) and (4.34)).

During the second stage, since the central hole has been filled up, the swelled substance is supposed to flow into the inter- and intra-granular pores distributed in the

matrix. In such a case the theoretical density of the porous skeleton would have to change accordingly, which gives $\dot{\rho}_T \neq 0$. However, since the overall space has been already occupied, the apparent volume of the pellet is constrained, therefore,

$$\dot{e} = \frac{\dot{\theta}}{1-\theta} - \frac{\dot{\rho}_T}{\rho_T} = 0 \tag{4.35}$$

The volume swelling during this stage was assumed to be accommodated by the change of the theoretical density of the substance. Below relationships are established based on Equation (4.35) and the mass conservation law,

$$\frac{\dot{\rho}_T}{\rho_T} = -\frac{\dot{\lambda}}{\lambda} \tag{4.36}$$

$$\frac{\dot{\theta}}{\dot{\lambda}} = \frac{d\theta}{d\lambda} = -\frac{1}{\lambda}(1-\theta) \tag{4.37}$$

So by solving above equations, the porosity change during the second stage of swelling with respect to the volume change can be evaluated. Similarly, if the assumption that has been applied in the first stage of swelling is still held here ($\dot{\lambda}/\lambda = \dot{\lambda}'/\lambda$), then the time dependence of the porosity change is obtained as below,

$$\dot{\theta} = \frac{d\theta}{dt} = -\left|\frac{\dot{\lambda}'}{\lambda'}\right|(1-\theta) \tag{4.38}$$

the above-derived equation can be solved together with Equations (4.21), (4.32) and (4.38) to represent how the porosity varies with time in the second stage of swelling.

4.3.2 Numerical approximations for two different swelling stages

The outer radius "b" was assigned to be 9 mm in accordance with the dimensions of the fabricated annular shape pellet. The inner radius plays an important role in determining the amount of the accommodated volume. The initial inner radius "a" was set to 1 mm, 1.5 mm and 2 mm with the purpose of obtaining comparable results. The initial porosity of the porous annular pellet was fixed at 0.36 in all the cases. Runge-Kutta 4th order method was again employed to iteratively solve these series of differential equations. Numerical solutions regarding two stages of swelling were combined to represent the porosity evolution on the entire time scale, as shown in Figure 4.17.

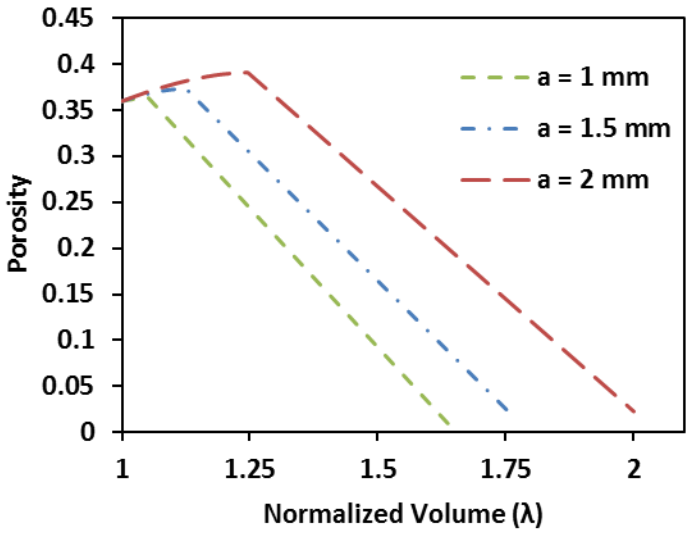

Figure 4.17 Numerical solutions: Porosity evolution vs. volume change when different inner radii are considered, two swelling stages are combined.

During the first stage of swelling, the porosity of the substance goes up nonlinearly as the substance flows into the central large hole. The moment when the volume increases to a critical value is corresponding to the closure of the central hole. This process is different to a general expansion case in which the substance's porosity increases linearly with its volume, indicating that the sintering of substance to some degree occurs during the swelling. Other than simply filling up the central hole, the substance itself also shrinks due to the existence of sintering stress, or in other words the effect of the Laplace stress - P_L.

On the contrary, the porosity evolution appears to be inversely proportional to the volume change in the second stage. The swelled substance flows into the internal pores to increase the theoretical density of the substance. Therefore this stage is literally recognized as a pure densification process. The change of the substance's theoretical density can be introduced by many factors, for example, phase transformation of the substance, or precipitation of fission solids. However, possible mechanisms of theoretical density augmentation are not included in the analytical calculation since it is beyond the scope of the present study.

By comparing the swelling behavior of annular pellets with different initial inner radii, one can see that a larger inner radius is corresponding to a higher capacity of accommodating the swelled volume. The analytical solutions also provide some thresholds regarding the porosity evolution and the volume change, which are considered as critical values of the swelling process, as summarized in Table 4.2.

Table 4.2 Obtained critical values from solving analytical equations

Inner radius, $\boldsymbol{a}$	1 mm	1.5 mm	2 mm
Maximum Porosity, $\boldsymbol{\theta_{max}}$	0.364	0.374	0.391
Intermediate Volume, $\boldsymbol{\lambda_i}$	1.052	1.125	1.246
Maximum Volume, $\boldsymbol{\lambda_{max}}$	1.639	1.759	1.989

The relationship between the porosity evolution and the swelling time was also retrieved by solving the differential equations with respect to different inner radii. As shown in Figure 4.18, it is similar to the previously obtained porosity - volume relationship, the porosity first goes up as the substance fills up the central hole, then it drops down in the subsequent densification step. The major difference is that the change of porosity is not linearly proportional to the time during both the first and the second stages. This phenomenon is most likely caused by the nonlinear viscoelastic properties of the substance. Also, one can see that smaller inner diameter corresponds to shorter swelling time, indicating that a pellet with smaller inner diameter is less capable of accommodating the swelled volume as its substance occupies more room.

The swelling accommodation capacity of a porous annular shape pellet has been preliminarily studied through the theoretical analyses. Two stages of swelling are identified by correlating the change of porosity with respect to the normalized volume as well as to the processing time. The analytical modeling shows that the porosity of the annular shape pellet first rises up to the maximum value and then all the way drops down to the minimum level during the swelling process. The relationship between the

porosity evolution and the volume change has revealed that the proposed porous annular shape geometry is able to accommodate the swelling of the substance. Also, a larger central hole appears to exhibit higher volume compensation capacity. However, it may have lower strength as it possesses less mass.

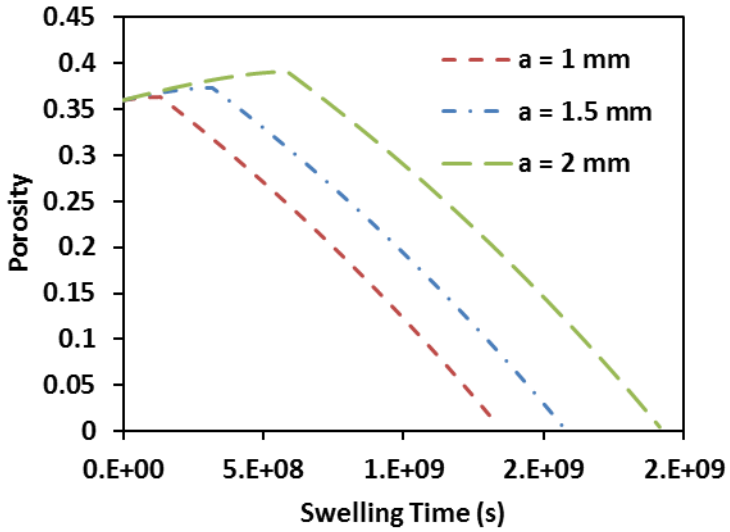

Figure 4.18 Numerical solutions: Porosity evolution vs. swelling time when different inner radii are considered, two swelling stages are combined.

In fact, one needs to consider the overall structural stability of the fuel pellet in order to satisfy the requirements of the service environment in real practice. Since the SPS technique has been evidenced to be able to produce porous pellets with desired geometry and good mechanical properties [122, 191], the prospect of adapting this technique into the fabrication of annular shape nuclear fuel pellets seems to be promising.

4.4 Modeling of Annular Shape Uranium Carbide Fuel under Irradiation-induced Swelling and Sintering

Uranium carbide (UC) fuel is considered in the present study as it offers several important advantages over commonly used uranium dioxide fuel. For example, UC possesses high thermal conductivity which reduces the thermal gradient through the fuel pellets. Also, unlike UO_2, the thermal conductivity of UC increases with temperature. Therefore both the magnitude and the rising trend of the thermal conductivity of UC fuel seem to comply with the safety demands for the modern nuclear reactors. In addition, carbide fuel usually produces higher breeding ratio than that the oxide one resulting from its high heavy metal atom density and high fissile atom density [186].

The most detrimental property of carbide fuel is the high swelling rate at elevated temperatures as it affects the performance and the integrity of fuel rods. The contributing factors to fuel swelling usually are the generation of fission products and fission gases. These products and gases increase in quantities as functions of fuel burnup [192]. The axial swelling restraint from the fuel-cladding mechanical interaction after the gap closure leads to the buildup of tensile stress in the cladding and could eventually cause the breach of the cladding. The release of fission products from the breach in the cladding can spread radioactivity through the primary coolant circuit and cause the shutdown of the reactor as well as the replacement of fuel assembly [193]. Therefore, it is necessary to control the swelling of carbide fuel in order to use them successfully.

Theoretical study in Section 4.3 was shown that the porous annular shape structure is able to accommodate the volume swelling caused by the viscous flow of the substance. The present study is devoted to the extrapolation of this proposed structure to the real nuclear fuel and to the investigation of the fuel pellet's behavior under the irradiation conditions. Stress accumulation of fuel pins with annular shape pellets is modeled as a function of time and burnup by taking into account the temperature non-uniformity in the pellets and non-linear creep of the UC nuclear fuel. The finite element simulated outcomes are compared to the analytical modeling results to reveal the different behaviors between irradiation and viscoelasticity-induced swelling.

4.4.1 Modeling of free swelling of UC fuel under irradiation conditions

The fission of ^{235}U in nuclear reactor is accompanied by the formation of solid and gaseous fission products. Solid fission products stay within the fuel and usually contribute to the fuel swelling linearly with the fuel burnup. Fission gases can either be retained in the fuel or released. The retained part of the fission gases also plays a role in the fuel swelling. Because of the high retention characteristics of the fission gases in carbide fuels, the contribution of retained fission gases is usually higher than that of solid fission products [194].

The value of the volume swelling strain due to solid swelling is usually estimated between 0.5% and 3% per one percent burnup. Based on the experimental data of Harrison [195], the solid fission swelling rate in the present study was considered to be about 1.17% per one percent burnup. As a result of fission, about

0.25 - 0.28 atoms of Xenon (Xe) and Krypton (Kr) are produced (there are 0.24 atoms of Xe and 0.04 atoms of Kr to have a total of 0.28 fission gas atoms) [196].

The behavior and impact of fission gas after its formation in the fuel is typically separated into several individual processes such as:

- Nucleation of fission gas bubbles;
- Single atom diffusion within the fuel grains to the bubbles and grain boundaries;
- Irradiation-induced resolution of the fission gas bubbles by fission fragments;
- Swelling of the bubbles under the influence of internal gas pressure.

The terms "bubbles" and "pores" used in this section is defined discriminately. A major difference between a bubble and a pore is that the pressure of the gas within the pore is generally quite small compared to that of the gas in the bubble as it is created during the fabrication of fuel pellets [184].

According to Ref [197], the number of nucleation sites for bubble formation and the resulting number of bubbles can be considered as material constants. For UC pellets, the number of bubbles was taken equal to $N_1 = 0.4 \cdot 10^{17}/cm^3$ for the intra-granular bubbles and $N_2 = 1.2 \cdot 10^{10}/cm^3$ for the grain surface inter-granular bubbles. Geometry of the grain and the bubbles considering in the finite element modeling is illustrated in Figure 4.19.

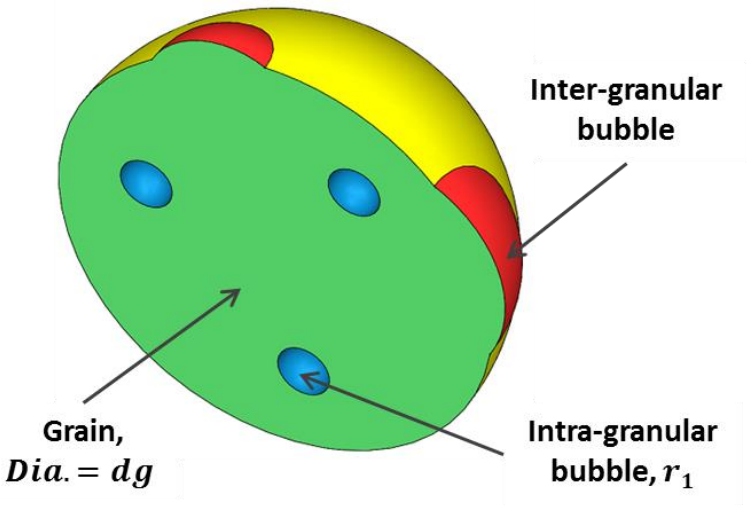

Figure 4.19 Geometry of the grain, intra- and inter-granular bubbles.

After the formation of fission gas, it starts migrating into the bubbles, the grains and the pores via a diffusion mechanism. The atomic concentration of the fission gas atoms in the UC grains, $C_g(\bar{r}, t)$, and the gas concentration in the inter-granular bubbles, $m_b(\bar{r}, t)$, can be described as the follows [197]:

$$\frac{\partial C_g}{\partial t} = \beta + D_g \nabla^2 C_g - \frac{\partial m_b}{\partial t} \tag{4.39}$$

$$\frac{\partial m_b}{\partial t} = 4\pi N_1 D_g C_g r_1 - y m_b \tag{4.40}$$

where $\bar{r}$ is the radial position within the grain, β is the gas atom generation rate, and D_g is the gas atom diffusion coefficient in the matrix. r_1 is the average radius of the intra-granular bubbles and y is the rate of resolution per gas atom in the bubbles. In general, Equation (4.39) describes the gas diffusion in the grain with the internal sources of gas. While Equation (4.40) gives the kinetics of the gas accumulation in the intra-granular bubbles taking into account the gas resolution under irradiation effects.

The last term in Equation (4.40) with the coefficient y indicates the amount of gas that can be driven back from the bubbles into the matrix through their interaction with the energetic fission fragments. According to Ref. [198], y is given by,

$$y = y'\dot{F} \tag{4.41}$$

where $\dot{F}$ is the fission rate density.

By applying the boundary condition, $C_g(\bar{r}, t) = 0$ at $\bar{r} = 0.5d_g$, where d_g is the grain diameter, to Equation (4.39) at the grain boundary [199]. It is possible to find the amount of trapped gas in the intra-granular bubbles as well as the portion of the gas that has moved into the inter-granular bubbles through the grain surface. Prajoto *et al*. reported that the UC experimental data are best simulated with $0.0875 \cdot 10^{-17} < y' < 1.4 \cdot 10^{-17}$ [197]. In the present study, the modeling y' was taken equal to 10^{-18}. Fission rate density, $\dot{F}$, can be calculated form the power density of the nuclear fuel, Q_N. In the current case, Q_N was selected between 120 W/cm^3 and 320 W/cm^3. Taking into account that the heating energy of a single fission is about 200 MeV, below relationship can be obtained,

$$\dot{F} = \frac{Q_N}{200MeV} = \frac{Q_N}{3.2 \cdot 10^{-11}\, J/fission} \tag{4.42}$$

this gives $\dot{F}$=3.7·10^{12} fission/cm^3/s for Q_N= 120 W/cm^3 and $\dot{F}$=9.9·10^{12} fission/cm^3/s for Q_N=320 W/cm^3. The gas atom generation rate, β, then can be calculated as (by assuming 0.28 atoms of Xe and Kr are produced per fission),

$$\beta = \frac{0.28 \cdot \dot{F}}{N_{cc}} = 11.2 \cdot 10^{-24} \dot{F} \tag{4.43}$$

where N_{cc} is the number of atoms in one cubic centimeter of nuclear fuel. For UC pellet with 75% relative density, N_{cc} was calculated to be $2.5 \cdot 10^{22}$ atoms. The fission rate density also defines the burnup rate. For example, one year burnup can be calculated as,

$$B_{UC} = \dot{B}_{UC} \cdot 3.2 \cdot 10^{7}(s) = \frac{\dot{F} \cdot 3.2 \cdot 10^{7}}{N_{cc}} = 1.28 \cdot 10^{-15} \dot{F} \tag{4.44}$$

this value is equal to 0.47% for Q_N= 120 W/cm^3 and 1.27% for Q_N= 320 W/cm^3.

The diffusion coefficient, D_g, in Equation (4.39) consists of two parts. One part corresponds to the temperature-independent irradiation-induced diffusion. It was found that the diffusion coefficient in this case is only determined by the defect production rate [197],

$$D_g' = 1.5 \cdot 10^{-31} \dot{F} \tag{4.45}$$

while the other part is temperature-dependent, which was retrieved from the experiments conducted by Ritzman *et al.*[200]. The combined diffusion coefficient has the following form,

$$D_g = 0.46\, exp\left(-\frac{326000}{RT}\right) + 1.5 \cdot 10^{-31} \dot{F} \qquad (cm^2/s) \tag{4.46}$$

The flow of the fission gases increases the pressure level in the intra-granular bubbles. This pressure can be calculated from the van der Walls equation of state, as,

$$p_g = \frac{m^* kT}{V_1 - m^* \Omega} \tag{4.47}$$

where m^* is the average number of gas atoms in the bubbles, Ω is the atomic volume for UC, which is $3.04 \cdot 10^{-29}$ m^3, and V_b is the intra-granular bubble volume, $V_1 = 4/3\pi r_1^3$ with r_1 as the intra-granular bubble radius. The average number of gas atoms per one bubble is expressed as,

$$m^* = \frac{m_b(\bar{r}, t) \cdot N_{cc}}{N_1} \tag{4.48}$$

The total pressure exerted on the intra-granular bubble can be expressed as the sum of three terms [201],

$$p_1 = p_g - \frac{2\gamma}{r_1} + p_{out} \tag{4.49}$$

where γ stands for the specific surface energy ($\gamma = 2\,J/m^2$) [197], and p_{out} results from the macroscopic pressure acting on the fuel pellet. In order to elaborate such a relationship, a representative unit cell of porous material was considered in the analysis. As shown in Figure 4.20, a spherical bubble is surrounded by a layer of an incompressible elastic substance.

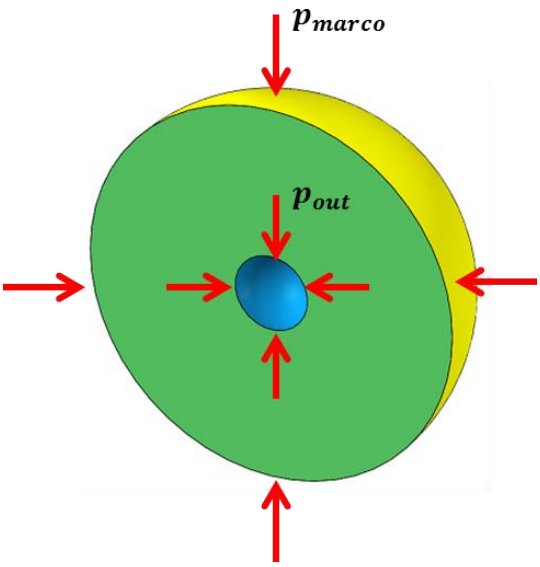

Figure 4.20 Schematics of a representative unit cell of porous material.

By applying the self-consistent approach to this porous unit cell, below expression can be obtained [2, 125],

$$p_{out} = p_{marco}\frac{4G\theta + 3K}{3K + 4G} \tag{4.50}$$

where p_{macro} is the macroscopic pressure, G and K are the bulk and shear moduli of UC, respectively. These elastic constants can be determined by the Young modulus and Poisson's ratio of UC, as follows [202, 203],

$$E_{UC} = 224 \cdot (1 - 2.3\theta)\left(1 - 9.2 \cdot 10^{-5}(T - 273)\right)\,[GPa] \tag{4.51}$$

$$G = \frac{E}{2(1+\nu)}, \qquad K = \frac{E}{3(1-2\nu)} \tag{4.52}$$

where T is the absolute temperature, θ is the overall porosity of the UC pellet and the Poisson's ratio of UC at room temperature is taken equal to 0.288 [202].

The internal pressure tends to increase bubble size due to the creep of materials around the bubble. With the purpose of estimating the macroscopic swelling due to the microscopic internal pressure in the intra-granular bubbles, p_1, the schematics of a unit cell in Figure 4.20 was considered again. The continuum theory of sintering was employed to solve this problem in details. The relative macroscopic swelling rate of grains introduced by the swelling of intra-granular bubbles can be expressed as,

$$\dot{e}_1 = A_{cr}^{UC} \frac{p_1}{\psi_1} \tag{4.53}$$

where ψ_1 is the normalized bulk modulus of intra-granular bubble and it can be represented by a function of the intra-granular porosity, θ_1, in the form of Equation (2.11). A_{cr}^{UC} is the creep coefficient of UC, according to Ref. [201], it is given as below,

$$A_{cr}^{UC} = \left(\frac{1.4}{d_g^2}\right) exp\left(\frac{-335\ kJ/mol}{RT}\right) + 1.7 \times 10^{-27}\dot{F} \tag{4.54}$$

where the grain size, d_g, was chosen to be 5 μm in the present study.

From the value of swelling rate of the intra-granular bubble, $\dot{e}_1$, the equation for the evolution of the intra-granular bubble radius can be obtained as,

$$\frac{dr_1}{dt} = \frac{\dot{e}_1 + \dot{e}_{solid}}{4\pi N_1 r_1^2} \tag{4.55}$$

where $\dot{e}_{solid}$ is assumed to be the volume swelling rate introduced by the precipitation of solid fission products through nuclear fuel burnup. It can be calculated as $\dot{e}_{solid} = 1.17\dot{B}_{UC}$ by assuming the solid fission swelling rate to be 1.17% per one percent

burnup (see also Section 4.3.1), in which the burnup rate, $\dot{B}_{UC}$, is given by Equation (4.44).

If the fission gas is not completely trapped in the intra-granular bubbles, it tends to move to the grain boundaries. At the grain boundaries, it either partially releases into pores or partially forms inter-granular bubbles. The amount of the gases released into pores was assumed to be proportional to the ratio of the pore to the grain boundary surface in the material. In the present study, the total porosity (0.25) was split into two parts: i) the UC kernel porosity and ii) the volume fraction of pores between the hot-pressed kernels. These two types of porosity were assigned by θ_k=0.1 and θ_s=0.15, respectively. The ratio between the pore and the grain boundary surface then can be calculated as,

$$c_{out} = \frac{\theta_k}{1-\theta_k}\frac{d_g}{d_p} + \frac{\theta_s}{1-\theta_s}\frac{d_g}{d_k} \tag{4.56}$$

Where d_k is the average diameter of the kernels, ~ 50 μm. Average diameter of the pores in the kernels is assumed to be equal to grain size, $d_p \approx d_g$. The above-defined coefficient, c_{out}, was used as follows: if the amount of gas atoms that has been moved to grain boundaries by diffusion is denoted as g_{out}, then $c_{out}g_{out}$of them are released into open pores and do not contribute to the internal pressure buildup in the fuel pellet anymore while all other gas atoms are assumed to be trapped into the inter-granular bubbles.

The shape of the inter-granular bubbles is different from that of the spherical intra-granular ones. They are more like lenticular shape, as shown in Figure 4.21, the volume of this kind of lenticular inter-granular bubble depends on its dihedral angle with respect to the grain boundary, as [204],

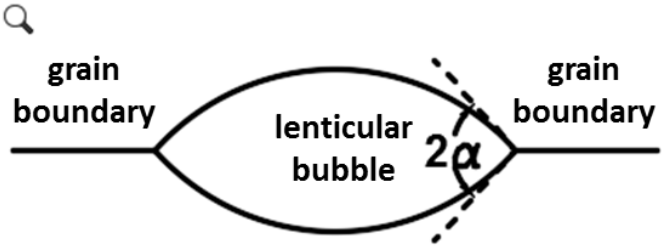

Figure 4.21 Schematics of lenticular inter-granular bubble.

$$V_2 = \frac{4}{3}\pi r_2^3 \frac{1 - 1.5\cos(\alpha) + 0.5\cos^3(\alpha)}{sin^3(\alpha)} \tag{4.57}$$

where α is the contact angle between the bubble and the grain boundary, r_2 is the curvature radius of the inter-granular bubble. Therefore, the gas pressure in the inter-granular bubble and the macroscopic swelling rate of grains due to swelling of inter-granular bubbles can be rewritten according to Equations (4.47) to (4.53), by substituting intra-granular bubble volume, V_1, with inter-granular bubble volume, V_2, replacing intra-granular bubble radius, r_1, with inter-granular bubble radius, r_2 and changing intra-granular porosity, θ_1, to inter-granular porosity, θ_2.

In the same manner, Equation (4.55) is transformed into,

$$\frac{dr_2}{dt} = \frac{\dot{e}_1 + \dot{e}_2 + \dot{e}_{solid}}{4\pi N_2 f(\alpha) r_2^2} \tag{4.58}$$

where f is a function of α from Equation (4.57), also known as the bubble shape factor, the relative volume change due to swelling of inter-granular bubbles is given as, $\dot{e}_2$. Therefore the total volume swelling rate is,

$$\dot{e}_{swell} = \dot{e}_1 + \dot{e}_2 + \dot{e}_{solid} \tag{4.59}$$

As it can be seen from previous analyses all the swelling calculations are based on the modeling of the fission gas diffusion in the UC grains through Equations (4.39) and (4.40). In the current investigation, the numerical solutions of these equations are based on the approach that proposed in Ref. [199]. By substituting Equation (4.40) into (4.39), below expression can be obtained for gas concentration in intra-granular bubbles,

$$\frac{\partial C_g(\bar{r},t)}{\partial t} = \beta + D_g \nabla^2 C_g - 4\pi N_1 D_g C_g r_1 + y m_b \tag{4.60}$$

and this equation can be transformed into a variational principle through Euler's theorem with respect to gas concentration, $C_g(\bar{r},t)$, as the follows:

$$\delta \int_0^{d_g/2} \left[\frac{D_g}{2}\left(\frac{dC_g}{d\bar{r}}\right)^2 + 2\pi N_1 D_g r_1 C_g^2 + \frac{C_g^2}{2\delta t} - (\beta + y m_b) C_g - C_g \frac{C_g^0}{\delta t} \right] \bar{r}^2 d\bar{r} = 0 \tag{4.61}$$

where the Dirichlet boundary conditions are assumed to be applied. An approximate solution to this equation can be obtained by choosing trial functions that satisfies the

boundary conditions and minimizes the integral in terms of free parameters in the function.

Quadratic functions were employed as they allow an exact representation of Equation (4.61) for long times. The spherical grain was split into two concentric regions of approximately equal volume as shown in Figure 4.22. In each region, the gas concentration is represented by a quadratic function. In the central region I, the gas concentration function is expressed by Equation (4.62) with the boundary condition of $dC_g/d\bar{r} = 0\ at\ \bar{r} = 0$. In the peripheral region II, the concentration function has the form of Equation (4.63) being constrained by $C_g = 0\ at\ \bar{r} = d_g/2$ [199],

$$C_g = \frac{C_1(0.64 - \rho^2)}{0.48} + \frac{C_2(\rho^2 - 0.16)}{0.48} \tag{4.62}$$

$$C_g = C_2 5(10\rho^2 - 19\rho + 9) + C_3 10(18\rho - 10\rho^2 - 8) \tag{4.63}$$

where C_1, C_2 and C_3 are three free parameters which are given by the radius ratios $\rho \equiv 2\bar{r}/d_g$ at $\rho_1 = 0.4$, $\rho_2 = 0.8$ and $\rho_3 = 0.9$, respectively. These positions are corresponding to the midpoint of the radius of region I, the interface of the two regions and the midpoint of region II (see also Figure 4.22). Also, these two equations are constrained to be continuous at the common boundary of the two regions.

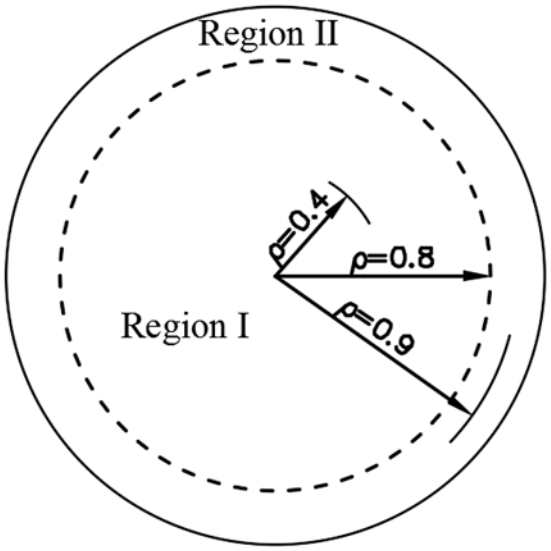

Figure 4.22 Schematics of the separation of pellet grain into regions.

In the same manner, the gas concentration in the intra-granular bubbles, $m_b(\bar{r}, t)$, was approximated using piecewise linear functions. Equations (4.64) and (4.65) are for region I and region II, respectively,

$$m_b = 2m_1 - m_2 + 2.5(m_2 - m_1)\bar{r} \tag{4.64}$$

$$m_b = 9m_2 - 8m_3 + 10(m_3 - m_2)\bar{r} \tag{4.65}$$

where m_1, m_2 and m_3 are gas concentrations in the intra-granular bubbles at above-mentioned three positions for the values of ρ. C_1, C_2 and C_3, m_1, m_2 and m_3 are dimensionless.

After substituting Equations (4.62) - (4.65) into Equation (4.61), below sets of differential equations are obtained,

$$\frac{dC_1}{dt} = \beta - (92.87k' + k'')C_1 + k'261.6C_2 - k'215.28C_3 + y(1.004m_1 - 0.05m_2 + 0.08m_3)$$

$$\frac{dC_2}{dt} = \beta + 87.16k'C_1 - (627.13k' + k'')C_2 + k'688.96C_3 + y(-0.063m_1 + 1.2m_2 - 0.25m_3) \quad (4.66)$$

$$\frac{dC_1}{dt} = \beta - 8.51k'C_1 + 508.6k'C_2 - (1072.85k' + k'')C_3 + y(0.006m_1 - 0.25m_2 + 1.4m_3)$$

and

$$\frac{dm_1}{dt} = k''C_1 - ym_1$$

$$\frac{dm_2}{dt} = k''C_2 - ym_2 \quad (4.67)$$

$$\frac{dm_3}{dt} = k''C_3 - ym_3$$

where coefficients $k' = D_g/d_g^2$ and $k'' = 4\pi D_g r_1 N_1$. According to the approximating Equations (4.62) - (4.65), the average values of the gas concentration in the grains and the intra-granular bubbles are,

$$\bar{C}_g = 0.2731C_1 + 0.3025C_2 + 0.3248C_3 \quad (4.68)$$

$$\bar{m}_b = 0.2560m_1 + 0.2208m_2 + 0.5232m_3 \quad (4.69)$$

where the values of C_1, C_2 and C_3, m_1, m_2 and m_3 are from solving Equations (4.66) and (4.67) for all moments of time.

After the gas concentration in the intra-granular bubble has been retrieved, the gas concentration in the inter-granular bubbles can be calculated based on the mass conservation law, as,

$$m_{gb} = 2(1 - c_{out})(\beta t - \bar{C}_g - \bar{m}_b) \tag{4.70}$$

this value together with the gas concentration in the intra-granular bubbles, $\bar{m}_b$, allows the prediction of the swelling of the nuclear fuel due to the generation of fission gases.

4.4.2 Analyses of stress development and temperature distribution in the fuel pellet

If the free macroscopic swelling strain is developed in the fuel pellet, macroscopic stresses on the claddings are propagated as a result of the radial constraint of the fuel pellet. These stresses were analyzed using the theory of elasticity. The statement of this problem is similar to that of the problem of thermal stress development: it is the difference between the volume swelling of the fuel pellet and that of the cladding layer who gives the stresses. The stress level is determined by the elastic displacement field during the volume swelling, which can be evaluated by applying the elastic potential energy function with respect to the volume,

$$U_{el} = \frac{1}{2} \int [K(e - e_{swell}) + G\gamma^2] dVol \tag{4.71}$$

where U_{el} is the elastic potential energy, e and γ are the invariants of the normal strain and shear strain tensors, respectively. e_{swell} is the accumulated swelling strain. When

the elastic displacement fields are determined, all developed elastic stresses can be calculated using Hook's law as the follows:

$$\sigma_{ij}^{el} = \left(K - \frac{2}{3}G\right) e\delta_{ij} + 2Ge_{ij}^{d} \tag{4.72}$$

where e_{ij}^{d} is the strain tensor deviator.

An important feature of high temperature swelling of UC fuel is the stress relaxation due to the creep of substance. As stated before, the purpose of considering a porous pellet is to potentially reduce the stress level at the cladding interface through the creep deformation. The macroscopic creep of the UC fuel, according to Ref. [201], has been formulated as,

$$\dot{\varepsilon}_{cr}^{UC} = \left(A_{cr}^{UC} + B_{cr}^{UC}\left(\sigma_{eff}^{UC}\right)^{1.44}\right)\sigma_{eff}^{UC} \tag{4.73}$$

where σ_{eff}^{UC} is the effective stress in porous UC pellet, which can be written explicitly by analogy to Equation (4.9), in which the stress components can be taken from the elastic solutions of Equations (4.71) and (4.72). A_{cr}^{UC} and B_{cr}^{UC} are creep constants for UC, A_{cr}^{UC} has been given by Equation (4.54) and B_{cr}^{UC} is based on Ref. [201], as,

$$B_{cr}^{UC} = 10.5exp\left(\frac{-529\ kJ/mol}{RT}\right) \tag{4.74}$$

Concerning the thermal properties of the UC fuel pellet, both the kernel porosity and the inter-kernel porosity were taken into account. Structurally, the analyzed UC fuel is made from the hot consolidation of UC kernels. The UC kernel itself has an average diameter of 50 μm and contains UC grains of 5 μm. Its porosity

is assigned as θ_k=0.1. While the inter-kernel porosity is assumed to be θ_s=0.15 to make a total porosity of 0.25 in the annular shape fuel pellet. During nuclear reaction, besides the heat conduction in the solid, there is also heat conduction in the fission gas-filled bubbles. The thermal conductivity of the stoichiometric UC kernel was taken as a function of temperature according to Ref. [205],

$$k_T^{UC} = [20.2 + 1.48 \cdot 10^{-3}(T - 273)]\, W/(m \cdot K) \tag{4.75}$$

the influences of multiple porosities on the effective thermal conductivity of the gas-filled porous material were evaluated by a series model in the present study [206],

$$k_T^{eff} = (1 - \theta)k_T^k + \theta k_T^g \tag{4.76}$$

where is k_T^k the thermal conductivity of the continuous matrix phase and k_T^g is the thermal conductivity of the gaseous phase. This equation were applied two times: i) for the calculation of the thermal conductivity of the porous kernel, in this case the kernel porosity, θ_k, was used; ii) for the assessment of the thermal conductivity of the material as a whole, in this case the inter-kernel porosity, θ_s, and the result from step i) were both substituted into the series equation.

Fission provides internal heat sources with powder between 120 W/cm^3 and 320 W/cm^3. The temperature at the outer surface of the pellet was assumed to be constant and equal to the temperature of the outer coolant, 920 ℃ (1193 K). Physical properties of UC which were employed in the simulation are listed in Table 4.3. In order to reduce computational cost, a 2D geometric model was constructed in COMSOL® Multiphysics. As shown in Figure 4.23, the annular pellet is 30 mm in

height, 18 mm in outer diameter and 5 mm in inner diameter. Due to its geometric symmetry, only the sub-domain in the first quadrant (positive axes) has been implemented in the simulation. The boundaries of the upper right-hand quarter of the 2D geometric model are numbered and the corresponding boundary conditions in the subsequent mechanical and thermal analyses are given in Table 4.4. In the solid mechanics module, boundary #4 was fixed along radial direction to impose constraints from the cladding layer and boundary #3 was subjected to a certain load to offset axial swelling. In the heat transfer module, boundary #4 was set to a constant temperature which equals to 1193 K while the others were defined as thermal-insulated boundaries.

Table 4.3 Physical properties of UC and initial values used in simulation

Property	**Value**	**Description**
$\boldsymbol{\alpha_V}$, (*1/K*)	13e-6	Thermal expansion coefficient
$\boldsymbol{\rho}$, (kg/m^3)	13600	Nominal density
$\boldsymbol{\theta_0}$	0.25	Initial porosity
$\boldsymbol{E}$, (*GPa*)	219	Young modulus at 25 ℃
$\boldsymbol{\nu}$	0.288	Poisson's ratio at 25 ℃
$\boldsymbol{\alpha}$, (°)	60	Contact angle for lenticular pores
$\boldsymbol{r_{p0}}$, (μm)	1.5e-4	Initial pore size
$\boldsymbol{\varepsilon_e}$	0.42	Emissivity
$\boldsymbol{T_{out}}$, *(K)*	1193	Outer temperature

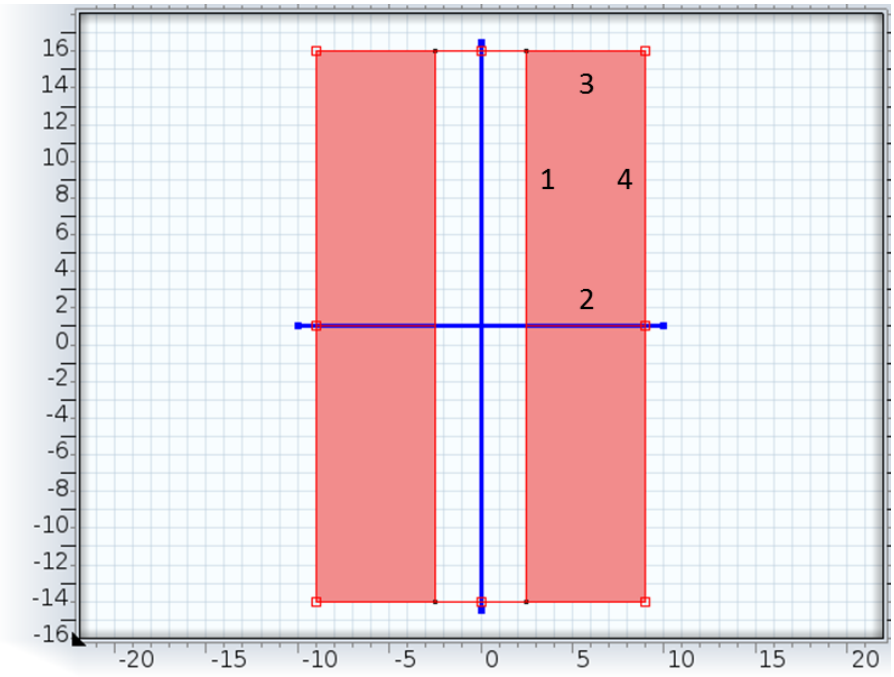

Figure 4.23 2D geometric model for annular fuel pellet with numbered boundaries

Table 4.4 Boundary conditions in simulation of annular shape UC fuel

Boundary#	1	2	3	4
Mechanical	free	symmetry	load	constrained r-dir.
Thermal	insulated	insulated	insulated	1193 K

4.4.3 Modeling results

Thermal and mechanical modules were coupled by COMSOL® Multiphysics software and solved using time-dependent solver on a total time span of two months of exploitation (~5·10^6 s). The atomic share of the released fission gas in the grains ($\bar{C}_g/\beta/t$), in the intra-granular bubbles ($\bar{m}_b/\beta/t$) and in the inter-granular bubbles ($g_{out}/\beta/t$) along the radial direction of the annular fuel pellet were evaluated at

different exploitation times under a nuclear fuel power density of 120 W/cm^3. As shown in Figure 4.24, the fission gas atoms in the grains are non-uniformly distributed. Much higher atomic concentration appears at the vicinity of the outer boundary, indicating that the fission gas atoms tend to dilute in the grains rather than diffusing into bubbles in this region. Also, one can see that the atomic concentration of diluted fission gas in the grains goes up with increasing exploitation time. The longer the irradiation, the more the gas atoms generated.

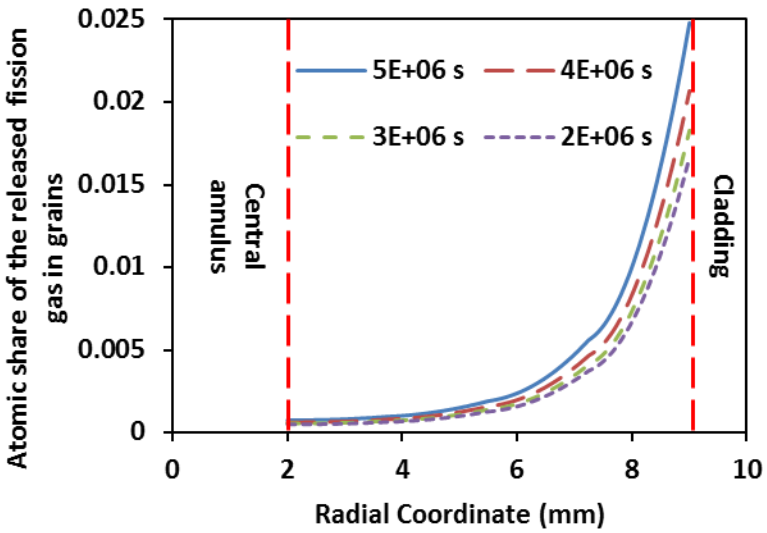

Figure 4.24 Atomic share of the released fission gas in the grains along radial direction with a nuclear fuel power density of 120 W/cm^3.

Due to the dilution of fission gas in the grains, the atomic gas concentration in the intra-granular bubbles drops rapidly in the corresponding region, as shown in Figure 4.25. The interaction between fission gas atoms in the grains and those in the intra-granular bubbles has been described by the diffusion mechanism (see also Equations (4.39) and (4.40)). When comparing Figure 4.24 to Figure 4.25, one can see

that there is an equilibrium stage existing before the midpoint of the pellet's radius (~5mm) and it soon shifts after that with giving more diluted gas atoms but less diffused ones. However, the influence of irradiation time on the level of atomic gas concentration in the intra-granular bubbles seems to be more distinguishable than that of the diluted gas atoms in the grains.

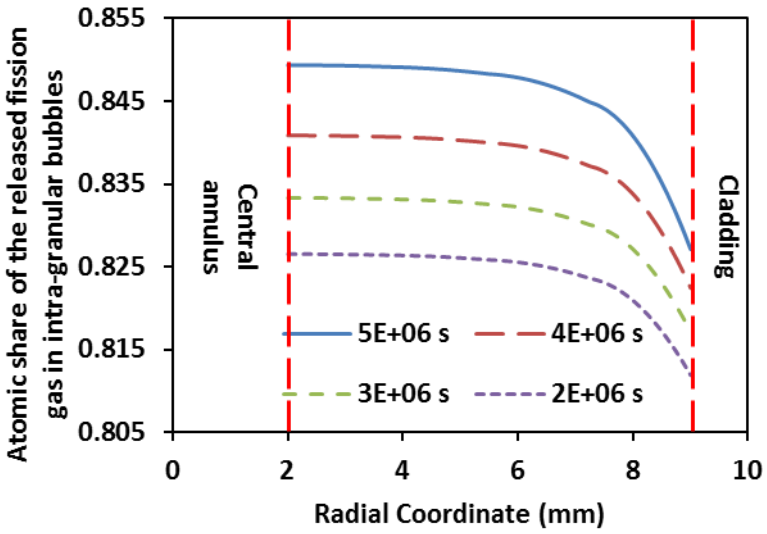

Figure 4.25 Atomic share of the released fission gas in intra-granular bubbles along radial direction with a nuclear fuel power density of 120 W/cm^3.

Part of gas atoms in the intra-granular bubbles can further migrate into grain boundaries to form inter-granular bubbles. Figure 4.26 gives the atomic gas concentration in the inter-granular bubbles as a function of radial coordinate. The evolution of gas concentration follows that of gas concentration in intra-granular bubbles but with fewer variations. This phenomenon can be attributed to the fact that the amount of the fission gas released into inter-granular bubbles was assumed to be proportional to the amount of gas released into pores (see also Equation (4.56)) as well

as to the amount of gas trapped in grains and inter-granular bubbles (see also equation (4.70)). One can also see that the irradiation time likewise affects the level of atomic gas concentration in the inter-granular bubbles.

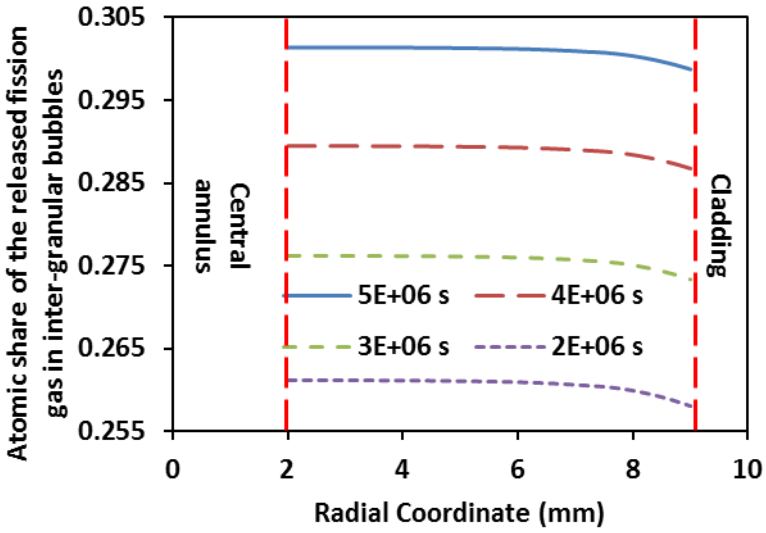

Figure 4.26 Atomic share of the released fission gas in inter-granular bubbles as a function of radial coordinate with a nuclear fuel power density of 120 W/cm^3.

The temperature distribution within the volume of the fuel pellet was retrieved from the simulation. As illustrated in Figure 4.27, by irradiating under a power density of 120 W/cm^3 for approximate two months (~ $5 \cdot 10^6$ s), the temperature distribution exhibits a thermal difference of 150 K along the radial direction. It is easy to see that the highest temperature appears near the central annulus while the lowest one is close to the cladding side as it was pre-defined as a constant in the modeling setup. The obtained temperature distribution diagram can be used to explain the evolution of atomic gas concentration along the radial direction. Since the diffusion of fission gas atoms is highly temperature-dependent (see also Equation (4.46)), at a higher

temperature, fission gas atoms are subjected to a stronger diffusion mechanism while on the other side the kinetics is opposite. Therefore, gas atoms tend to move from grains to bubbles within the high temperature region which is close to the central annulus and nearly no gas atoms are diluted in the grains. Within the low temperature region, gas atoms prefer being trapped in the grains rather than diffusing into bubbles which give in a rapid increase of gas atoms concentration in the grains.

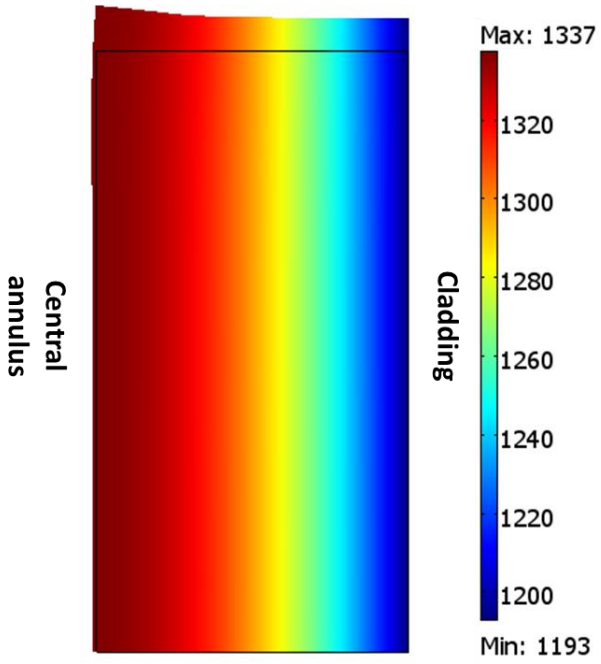

Figure 4.27 Temperature distribution after $5 \cdot 10^6$ s with a nuclear fuel power density of 120 W/cm^3 (Unit: K).

Figure 4.28 comparatively plots the simulated temperature values along radial direction when the pellet is subjected to nuclear fuel power density of 120 W/cm^3 and 320 W/cm^3. One can see that higher powder density provides larger temperature difference (~ 400 K) between the central annulus and the cladding side of the fuel

pellet. Compared to a low fuel power density of 120 W/cm^3, a high fuel power density of 320 W/cm^3 can introduce a much larger atomic gas concentration difference in the grains and the bubbles according to the above-discussed diffusion mechanism of fission gas atoms. In such a case, more inhomogeneous volume swelling of fission gas bubbles might happen.

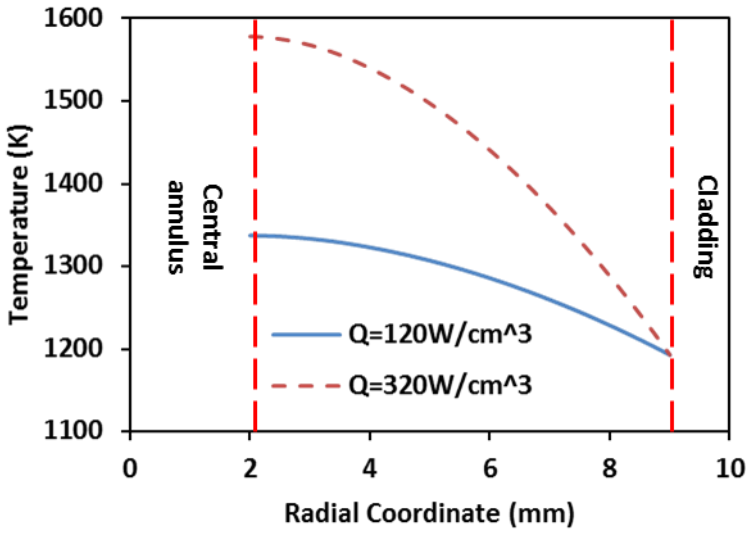

Figure 4.28 Temperature as a function of radial coordinate with a nuclear fuel power density of 120 W/cm^3 and 320 W/cm^3.

The swelling strain rates (see also Equation (4.73)) were integrated with respect to irradiation time and summed up to denote the total swelling strain generated in the annular pellet during fuel exploitation. The accumulated swelling strains at different time steps are plotted with respect to radial coordinate in Figure 4.29. In general, the highest strain is located near the central annulus while the circumferential area possesses the lowest one. Despite the fact that the evolution of total swelling strain exhibits an overall decreasing trend, a local minimum of swelling strain is

observed when it propagates between 1 - 2 mm from the inner wall. Also, one can see that the magnitude of the local minimum in each individual curve rises with increasing irradiation time. These fluctuations of swelling strain can be most likely attributed to the variation of the fission gas pressure due to a non-uniform temperature field.

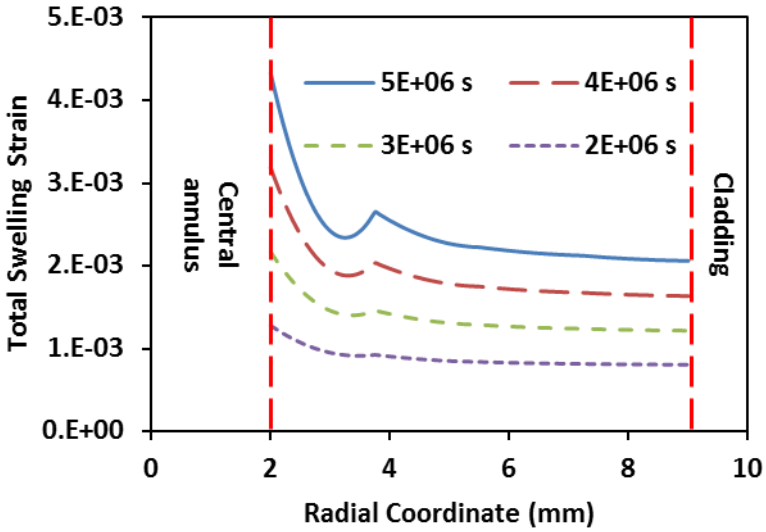

Figure 4.29 Total swelling strain as a function of radial coordinate with a nuclear fuel power density of 120 W/cm^3.

The displacement distribution in the pellet after two months of exploitation ($5 \cdot 10^6$ s) is demonstrated in Figure 4.30 with the arrows indicating the displacement field. As one can see that the magnitude of displacement increases along the axial direction. Also, the maximum displacement appears around the top left-hand corner of the pellet, indicating that an intensification of accumulated swelling strain is formed. The non-uniform displacement distribution in the pellet is in accordance with the overall evolution trend of the total swelling strain described in Figure 4.29, in which higher strain usually corresponds to larger displacement. It is worth noting that the

displacements around the central hole are negligible in comparison to those along the axial direction. This observation differs from the two-stage (swelling-sintering) assumption made in Section 4.3.1 for viscous flow based swelling of the substance, which indicates that the swelling of fission gas bubbles is prone to propagating along the axial direction.

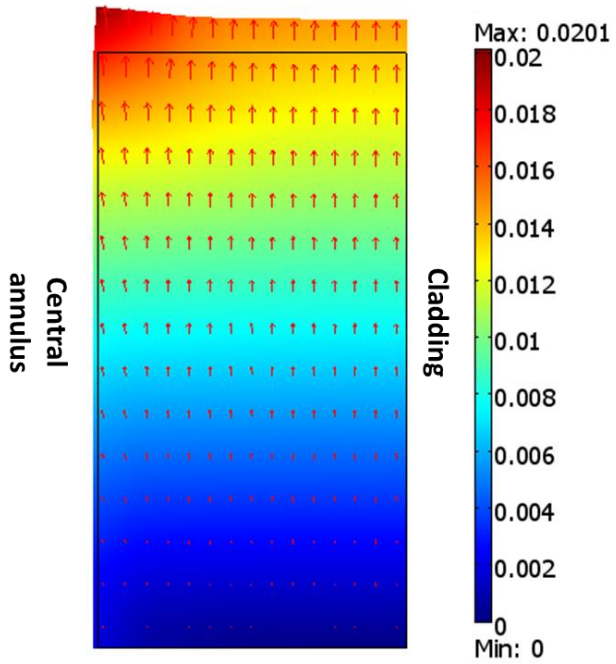

Figure 4.30 Distribution of total displacement after $5 \cdot 10^6$ s with a nuclear fuel power density of 120 W/cm^3 (Unit: mm). Arrows indicate displacement field.

The evolution of total swelling strain similarly influences the evolution of total porosity distribution in the pellet as they are correlated by the mass conservation law (see also Equation (2.12)). As shown in Figure 4.31, the total porosity likewise gives an overall decreasing trend along the radial direction. However, careful examination of the porosity values reveals that the porosity discrepancy between the inner hole and

the outer wall of the pellets is actually negligible. Therefore one can assume that the porosity is literally uniformly distributed within the pellet.

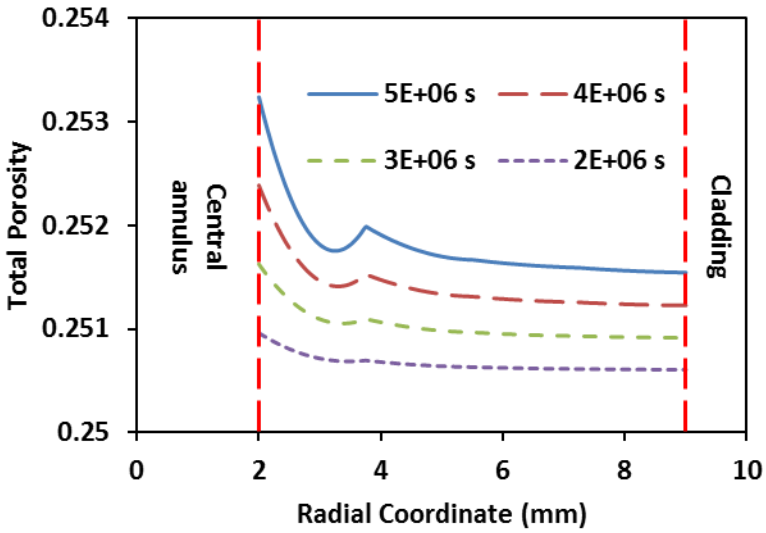

Figure 4.31 Total porosity as a function of radial coordinate with a nuclear fuel power density of 120 W/cm^3.

Above-mentioned porosity distribution is mapped in Figure 4.32. One can see that only the region close to the upper left-hand corner has slightly higher porosity compared to the rest of the pellet after 5 $\cdot 10^6$ s. In addition, all porosity values retrieved from different exploitation times are higher than the pre-assigned initial porosity (0.25), indicating the annular pellet is swelling everywhere and the creep of the porous UC fuel is not sufficient to accommodate the swelling of it.

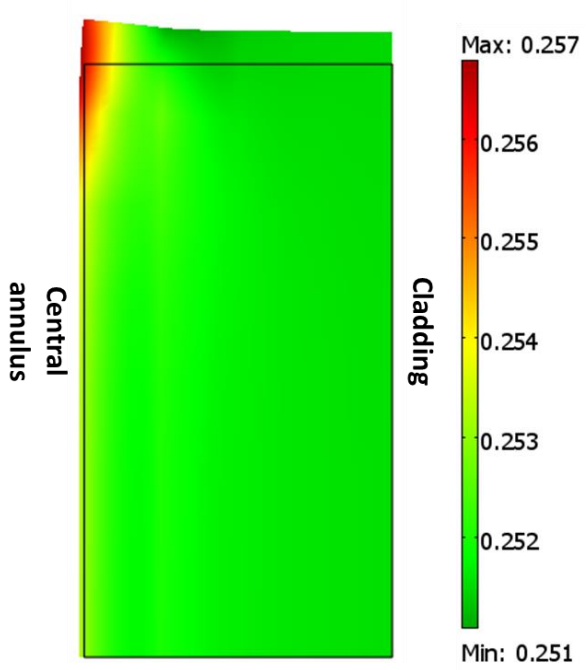

Figure 4.32 Total porosity distribution after 5 $\cdot 10^6$ s with a nuclear fuel power density of 120 W/cm^3.

The radial stress distribution in the pellet is a matter of interest as it is directly related to the stress state of the cladding layer. It can be seen from Figure 4.33 that the modeling result predicts very high stress development in the pellet. The highest radial stress appears at the top of the cross-section where the local minimum of swelling strain forms (see also Figure 4.29). Such a cross-sectional region also exhibits higher radial stress than anywhere else in the pellet, which implies that the fluctuation of swelling strain within this region not only contributes to non-uniform displacement field but also causes stress concentration. The radial stress at the lower right-hand corner of the annular pellet was calculated to be ~70 MPa, which can be recognized as the tensile stress acting on the cladding side. This kind of highly developed stress is harmful to the cladding during nuclear irradiation and it is necessary to be essentially

taken into account when designing and selecting the structures and the properties for cladding materials.

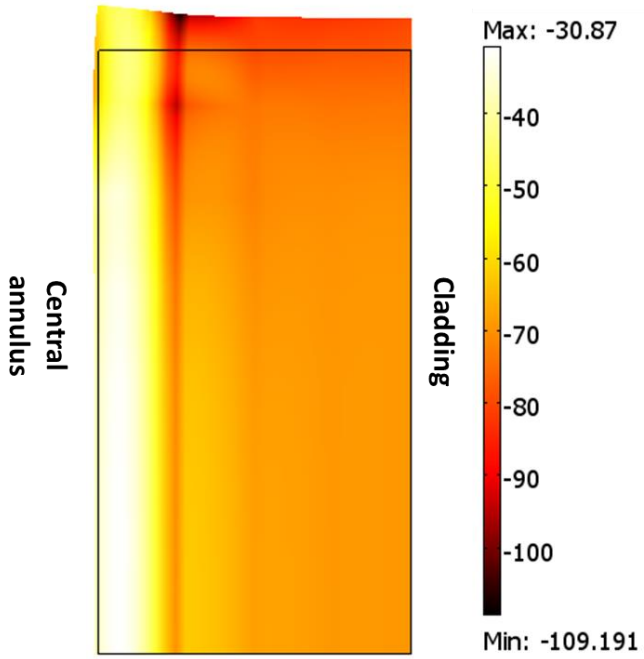

Figure 4.33 Radial stress distribution after 5 $\cdot 10^6$ s with a nuclear fuel power density of 120 W/cm^3.

The developed finite element modeling framework predicts high stress level on the cladding after a short time of fuel exploitation (about two months). The creep of the porous UC fuel appears to be not sufficient enough to accommodate the irradiation-induced swelling and stress buildup due to the generation of fission gases and solids. This type of mismatch gives porosity augmentation throughout the pellet as well as stress concentration at the interface close to the cladding layer. To refine the simulation results, the creep parameters of UC need more precise experimental assessments. Also, fission gas swelling during fuel irradiation depends on the specific

internal surface area of the porous nuclear fuel and gas adsorption porosimetry can give reliable data for theoretical estimation of fission gas release from the fuel.

4.5 Chapter Conclusions

The optimal SPS conditions for producing disk-like shape ZrC specimens have been applied to process annular shape ZrC pellets. Such a special geometry has been implemented by inserting a thin mandrel throughout the graphite components of the SPS tooling. The densification kinetics of the annular shape ZrC pellets were studied with introducing pressure at different time occasions during the process. Although the application of pressure immediately influenced the densification during either the initial or the intermediate sintering stage, it appeared to have not effects on the final density level of the processed pellets. Even despite the successful experiments, the stress state of the thin mandrel has raised further consideration as it accounts for the most vulnerable part of the entire tooling setup.

To investigate the stress evolution in the SPS of annular shape ZrC pellets, a finite element simulation was employed. A stress – strain oriented sintering constitutive equation was derived from the original one to appropriately couple other physics in the simulation. The Von Mises stress has been selected as the indicator of stress distribution in the entire tooling - specimen system. It was shown that the stress concentration at the specimen - mandrel interface is more intense compared to that at the specimen - die interface. The simulation also revealed that a fluctuant stress state in the mandrel forms during the rapid densification of ZrC pellet which renders the consideration of mandrel sustainability. The overall increasing trend of the hydrostatic

stress at the specimen - mandrel interface again emphasized that it is necessary to take the pressure acting on the mandrel into consideration in real practice.

The experimental procedures of fabricating ZrC pellets have been practically adapted to process SiC-ZrB_2 composite powders in order to make tooling components for SPS applications. Both cylindrical shape punches and annular shape dies were produced via SPS. The applicability of the composite SPS tooling was first evaluated with SPS of alumina powder at 1400 ℃, in which the axial pressure was gradually increased to 210 MPa and fully dense specimens were obtained. Since the composite tooling was survived from applying high pressure, it has been used in the SPS of ZrC powder at even higher processing temperature. It is shown that the composite tooling was able to withstand an axial pressure of 190 MPa at 1500 ℃ and produce highly dense ZrC specimens. These observations have suggested that the SPS-processed SiC-ZrB_2 components could be considered as a good candidate of tooling materials for high pressure SPS.

A prospective application of sintered annular shape carbide pellet is to utilize its geometric features to accommodate the volume swelling during its service such as nuclear reaction at elevated temperature. The feasibility of applying such a special geometry has been preliminary examined through investigating its porosity evolution during the volume swelling, in which both the central hole and the internal pores were considered as sinks of swelled volume. Analytical expressions were derived based on pre-assigning two-stage swelling to a porous annular shape pellet. Numerical solutions showed that the porosity of the pellet first rises and then drops with respect to either

the normalized volume or to the processing time. It appears that the accommodation capacity of an annular shape pellet could benefit from increasing the size of the central hole while the overall structural strength might be compromised.

As an extrapolation of the analytical study on the swelling of a porous annular shape pellet, finite element simulation has been employed to investigate the swelling and sintering of annular shape nuclear UC fuel under irradiation conditions. Fission gases and solids were considered as the sources of fuel pellet swelling. Diffusion of fission gas atoms in the grains, intra- and inter-granular bubbles have been formulated as functions of fission rate and exploitation time. The irradiation-induced swelling was coupled with the temperature-activated sintering of the UC fuel in the simulation. The concentrations of fission gas atoms along radial direction were shown to significantly depend on the temperature distribution in the pellet. The evolution of total swelling strain simultaneously influenced the displacement and stress distributions as well as gave porosity augmentation in the pellet. The simulation results also predicted high radial stress in the pellet, which indicated the sintering (creep) of the UC fuel cannot adequately accommodate the irradiation-induced swelling of the pellet. In addition, the modeling is shown that the swelling is preferred to propagate along the axial direction rather than the radial direction, which raises the considerations for reevaluating and redesigning of the structure of the annular shape pellets.

CHAPTER 5 CONCLUSIONS

5.1 Achieved Goals

Spark plasma sintering has been successfully employed to consolidate micron-sized zirconium carbide powders to map the densification level with respect to the processing parameters. Compared to hot pressing, under the same processing conditions, SPS achieved a higher level of densification due to the assistance of the electric current. The pressure effect in the densification of ZrC under SPS conditions was investigated via conducting single- and double-die SPS experiments. It is shown that the magnitude of the applied pressure can introduce fast densification and lower processing temperature. This observation triggers the research interests in manipulating loading mode in order to enhance densification efficiency in SPS of ZrC.

Transverse rupture strength and microhardness of the ZrC specimens have been examined and correlated to their relative density and average grain size. Heat capacity and thermal conductivity of the ZrC specimens with various porosities were measured at different temperatures. The obtained mechanical and thermal properties of the SPS-processed ZrC specimens have demonstrated the feasibility of applying them to serve under high temperature and loads.

An in-depth investigation was conducted to elucidate the densification behavior of ZrC under regular SPS and hot pressing conditions. An analytical equation that describes the porosity evolution in rigid die pressing of ZrC at elevated temperature has been formulated based on the continuum theory of sintering, in which

the mass transfer phenomenon was expressed by the non-linear power-law creep of porous material.

To determine the creep coefficients, the clarification of the contact resistance and temperature distribution in the SPS tooling - specimen system was quantitatively evaluated. The evolutions of electric contact resistances in the SPS graphite tooling system were obtained using specially designed experiments. Both temperature and pressure effects were included in the investigations. The finite element modeling approach was utilized to reveal the temperature distribution in SPS of ZrC by considering the contribution of contact resistance.

The simulated temperature within the specimen's cross-section was subsequently used in solving the derived densification equation, the numerical solutions of which were inversely regressed to the experimental data. The mass transfer driving densification mechanism in the hot consolidation of ZrC was revealed to be the grain boundary sliding associated with dislocation glide controlled creep. Comparison of the activation energy in SPS with the one in the hot pressing of ZrC has confirmed the benefits of introducing electric current assistance in the powder consolidation processes.

The obtained creep coefficients were employed in the evaluation of the densification behavior of ZrC under the proposed spark plasma sinter forging (SPS-forging) regime. The theoretical predictions have been verified by experimental observations to show that the SPS-forging was able to enhance the densification efficiency in the later stages of SPS. To construct optimal loading schematics, SPS-

forging and regular SPS were combined to form a hybrid loading mode SPS. By imposing loading control during the SPS of porous ZrC under the hybrid setup, both the densification and the deformation of the specimen have been guaranteed.

Being employed as a surrogate material of uranium carbide fuel, ZrC powder were fabricated into annular shape pellets via SPS to meet the geometric requirements of novel nuclear fuel pellets. Special tooling components were used to tailor the structure during the densification process. Such a tooling setup was examined to be stable when the axial load was applied at either low or high temperatures. However, the finite element simulation has suggested that the stress concentration at the mandrel to specimen interface can cause tooling failure. Besides the stress distribution, the developed modeling framework was shown to be able to dynamically correlate the densification of the specimen with the motion of the tooling components.

An immediate application of the annular shape geometry was the production of the high strength tooling components for the SPS process. An SPS tooling setup including cylindrical punches and annular shape die made out of SiC-ZrB_2 powders was utilized to process alumina and ZrC powders. It is shown that the composite tooling was capable of handling the highly applied axial pressure during SPS at moderate temperatures. As a result, microstructures have been refined in the obtained highly dense specimens.

As the developed SPS procedures for making annular shape ZrC pellets can be eventually implemented to produce UC nuclear fuel pellets. The feasibility of applying a porous nuclear fuel pellet with annular shape geometry to accommodate volume

swelling during the nuclear reaction was first evaluated through analytical models. The evolutions of porosity and the volume changes introduced by the swelling of substance were formulated based on the non-linear viscous behavior of materials. The obtained results suggested that both the central hole and the porous ring can accommodate the swelled substance to a certain degree. Finite element simulations were conducted in addition to the analytical study to take into consideration the irradiation-imposed swelling. The modeling outcomes indicated that the swelling caused by the generation and diffusion of fission gases in the annular shape fuel pellets appeared to suppress those initiated by the precipitation of fission solids. The simulation predicted also significant stress buildup in the fuel pellet after a short period of exploitation due to the accumulation of fission gas bubbles.

5.2 Scientific and Engineering Novelties

a. The manipulation of loading modes has been implemented for the first time in SPS of a typical UHTC such as ZrC. The theoretical-experimental approach has not only elucidated the influences of loading modes on SPS densification efficiency but also provided the guidelines to optimize the densification behavior.

b. The SPS technique has been experimentally evidenced to be able to process carbide components with tailored structures. Fabricated near net-shaped SiC-ZrB_2 composite parts have been successfully used as alternative tooling in high-pressure SPS applications.

c. Applications of the SPS-processed annular shape pellets have been extrapolated to the compensation of volume swelling during their service. Analytical and numerical studies have been carried out to evaluate the swelling behaviors under conventional and irradiative conditions, respectively.

5.3 Summary of Conducted Work

A flowchart that sums up the conducted work corresponding to the formulated research objectives and tasks in Figure 1.7 is given in Figure 5.1. It is safe to conclude here that all preset tasks have been sufficiently accomplished in the present study.

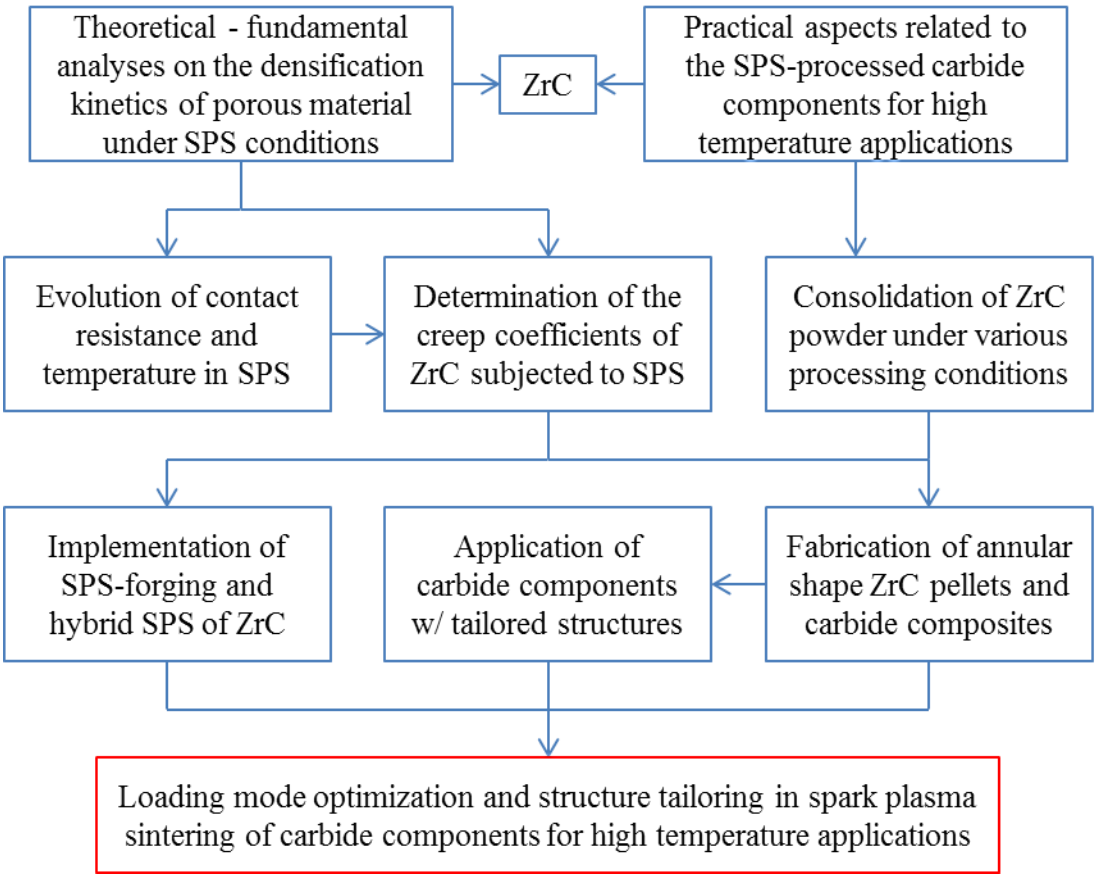

Figure 5.1 Summary of conducted work in a flowchart.

REFERENCES

[1] G. C. Kuczynski. Self-diffusion in sintering of metallic particles. Trans. AIME. 1949;185:169-178.

[2] J. K. Mackenzie, and R. Shuttleworth. A phenomenological theory of sintering. Proc. Phys. Soc. B. 1949;62:833-852.

[3] W. D. Kingery, and M. Berg. Study of the initial stages of sintering solids by viscous flow, evaporation-condensation, and self-diffusion. J. Appl. Phys. 1955;26:1205-1212.

[4] R. L. Coble. Sintering crystalline solids. I. Intermediate and final state diffusion models. J. Appl. Phys. 1961;32:787-792.

[5] M. F. Ashby. A first report on sintering diagrams. Acta Metall. 1974;22:275-289.

[6] A. L. Gurson. Continuum theory of ductile rupture by void nucleation and growth .1. Yield criteria and flow rules for porous ductile media. J. Eng. Mater.-T. ASME. 1977;99:2-15.

[7] M. N. Rahaman, L. C. De Jonghe, and R. J. Brook. Effect of shear stress on sintering. J. Am. Ceram. Soc. 1986;69:53-58.

[8] V. V. Skorokhod, E. A. Olevsky, and M. B. Shtern. Continuum theory of sintering. I. Phenomenological model. Analysis of the effect of external forces on the kinetics of sintering. Powder Metall. Met. Ceram. 1993;32:21-26.

[9] V. V. Skorokhod, E. A. Olevskii, and M. B. Shtern. Continuum theory of sintering. II. Effect of the rheological properties of the solid-phase on the kinetics of sintering. Powder Metall. Met. Ceram. 1993;32:112-117.

[10] Z. Z. Du, and A. C. F. Cocks. Constitutive models for the sintering of ceramic components.2. Sintering of inhomogeneous bodies. Acta Metall. Mater. 1992;40:1981-1994.

[11] M. N. Rahaman, L. C. Dejonghe, and C. H. Hsueh. Creep during sintering of porous compacts. J. Am. Ceram. Soc. 1986;69:58-60.

[12] R. M. McMeeking, and L. T. Kuhn. A diffusional creep law for powder compacts. Acta Metall. Mater. 1992;40:961-969.

[13] D. S. Wilkinson, and M. F. Ashby. Pressure sintering by power law creep. Acta Metall. 1975;23:1277-1285.

[14] H. Riedel, K. V, and J. Svoboda. Densification and creep in the final stage of sintering. Acta Metall. Mater. 1994;42:3093-3103.

[15] A. C. F. Cocks, and N. D. Aparicio. Diffusional creep and sintering - the application of bounding theorems. Acta Metall. Mater. 1995;43:731-741.

[16] Z. A. Munir, U. Anselmi-Tamburini, and M. Ohyanagi. The effect of electric field and pressure on the synthesis and consolidation of materials: A review of the spark plasma sintering method. J. Mater. Sci. 2006;41:763-777.

[17] J. R. Groza, and A. Zavaliangos. Sintering activation by external electrical field. Mater. Sci. Eng. A. 2000;287:171-177.

[18] M. Cologna, J. S. C. Francis, and R. Raj. Field assisted and flash sintering of alumina and its relationship to conductivity and mgo-doping. J. Eur. Ceram. Soc. 2011;31:2827-2837.

[19] M. A. Meyers, and K. K. Chawla. Mechanical behavior of materials: Cambridge University Press; 2009.

[20] E. Olevsky, and A. Molinari. Kinetics and stability in compressive and tensile loading of porous bodies. Mech. Mater. 2006;38:340-366.

[21] E. A. Olevsky, J. Ma, J. C. LaSalvia, and M. A. Meyers. Densification of porous bodies in a granular pressure-transmitting medium. Acta Mater. 2007;55:1351-1366.

[22] J. A. Alvarado-Contreras, R. M. German, A. L. Maximenko, and E. A. Olevsky. Coupled densification-shape distortion analysis of liquid phase sintering affected by gravity. Metall. Mater. Trans. A. 2013;45:927-933.

[23] L. Galuppi, and L. Deseri. Combined effects of interstitial and laplace pressure in hot isostatic pressing of cylindrical specimens. J. Mech. Mater. Struct. 2014;9:51-86.

[24] Y. G. Dorofeev. Distribution of density in powder blanks during free upsetting. Sov. Powder Metall. Met. Ceram. 1975;14:351-355.

[25] Y. G. Dorofeev, G. A. Dreev, and V. N. Mishchenko. Characteristic hot-forging defects in porous powder blanks of stepped shape. Sov. Powder Metall. Met. Ceram. 1988;27:681-684.

[26] G. A. Baglyuk. Free upsetting of heated porous cylindrical specimens. Sov. Powder Metall. Met. Ceram. 1988;27:532-535.

[27] G. A. Baglyuk. Analysis of the kinematics of the process of free upsetting of a porous cylinder in the presence of contact friction. Powder Metall. Met. Ceram. 1993;32:16-20.

[28] H. K. Cho, J. Suh, and K. T. Kim. Densification of porous alloy-steel preforms at high-temperature. Int. J. Mech. Sci. 1994;36:317-328.

[29] H. N. Han, Y. G. Lee, K. H. Oh, and D. N. Lee. Analysis of hot forging of porous metals. Mater. Sci. Eng. A. 1996;206:81-89.

[30] R. Narayanasamy, and K. S. Pandey. A study on the barrelling of sintered iron preforms during hot upset forging. J. Mater. Process. Technol. 2000;100:87-94.

[31] R. V. Egorova, M. S. Egorov, and A. V. Skorikov. Free upsetting of heated cylindrical specimens of powder materials astaloy 85 mo and distaloy hp-1 from höganäs. Metallurgist. 2013;57:442-448.

[32] L. C. Dejonghe, and M. N. Rahaman. Loading dilatometer. Rev. Sci. Instrum. 1984;55:2007-2010.

[33] M. N. Rahaman, and L. C. De Jonghe. Sintering of cdo under low applied stress. J. Am. Ceram. Soc. 1984;67:C-205-C-207.

[34] K. R. Venkatachari, and R. Raj. Shear deformation and densification of powder compacts. J. Am. Ceram. Soc. 1986;69:499-506.

[35] K. R. Venkatachari, and R. Raj. Enhancement of strength through sinter forging. J. Am. Ceram. Soc. 1987;70:514-520.

[36] R. Narayanasamy, and K. S. Pandey. Salient features in the cold upset-forming of sintered aluminium–3.5% alumina powder composite preforms. J. Mater. Process. Technol. 1997;72:201-207.

[37] A. Shirizly, J. Tirosh, and L. Rubinski. Open die forging of porous materials. Mater. Sci. Eng. A. 1998;249:55-61.

[38] A. R. Cooper, and L. E. Eaton. Compaction behavior of several ceramic powders. J. Am. Ceram. Soc. 1962;45:97-101.

[39] K. Kawakita, and K. H. Ludde. Some considerations on powder compression equations. Powder Technol. 1971;4:61-68.

[40] P. J. Denny. Compaction equations: A comparison of the heckel and kawakita equations. Powder Technol. 2002;127:162-172.

[41] N. A. Fleck. On the cold compaction of powders. J. Mech. Phys. Solids. 1995;43:1409-1431.

[42] A. K. Ariffin, and D. T. Gethin. Model for thermal analysis in cold uniaxial powder compaction. Powder Metall. 1998;41:123-129.

[43] C. L. Martin, and D. Bouvard. Study of the cold compaction of composite powders by the discrete element method. Acta Mater. 2003;51:373-386.

[44] R. Spriggs, and S. Dutta. Mechanisms of sintering during hot pressing and recent technological advances. In: G. C. Kuczynski, editor. Sintering and related phenomena: Springer US; 1973. p. 369-394.

[45] C. Herring. Diffusional viscosity of a polycrystalline solid. J. Appl. Phys. 1950;21:437-445.

[46] F. R. N. Nabarro. Steady-state diffusional creep. Philos. Mag. 1967;16:231-237.

[47] Y. M. Liu, H. N. G. Wadley, and J. M. Duva. Densification of porous materials by power-law creep. Acta Metall. Mater. 1994;42:2247-2260.

[48] S. Bhattacharya, K. Jakus, and I. Grosse. Modelling pressure-assisted densification by power-law creep. J. Mater. Sci. 1997;32:6183-6189.

[49] R. L. Coble. Diffusion models for hot pressing with surface energy and pressure effects as driving forces. J. Appl. Phys. 1970;41:4798-&.

[50] S. C. Liao, K. D. Pae, and W. E. Mayo. The effect of high-pressure on phase-transformation of nanocrystalline tio2 during hot-pressing. Nanostruct. Mater. 1995;5:319-325.

[51] H. T. Martirena, and J. C. Burfoot. Grain-size and pressure effects on the dielectric and piezoelectric properties of hot-pressed PZT-5. Ferroelectrics. 1974;7:151-152.

[52] R. Moussa, J. L. Chermant, and F. Osterstock. Creep of hot-pressed SiC-Al materials. J. Phys-Paris. 1986;47:679-683.

[53] N. A. Fleck, L. T. Kuhn, and R. M. McMeeking. Yielding of metal powder bonded by isolated contacts. J. Mech. Phys. Solids. 1992;40:1139-1162.

[54] R. M. Govindarajan, and N. Aravas. Deformation processing of metal powders: Part I-cold isostatic pressing. Int. J. Mech. Sci. 1994;36:343-357.

[55] E. Arzt, M. F. Ashby, and K. E. Easterling. Practical applications of hotisostatic pressing diagrams: Four case studies. Metall. Trans. A. 1983;14:211-221.

[56] A. S. Helle, K. E. Easterling, and M. F. Ashby. Hot-isostatic pressing diagrams - new developments. Acta Metall. 1985;33:2163-2174.

[57] F. B. Swinkels, D. S. Wilkinson, E. Arzt, and M. F. Ashby. Mechanisms of hot-isostatic pressing. Acta Metall. 1983;31:1829-1840.

[58] H. N. G. Wadley, R. J. Schaefer, A. H. Kahn, M. F. Ashby, R. B. Clough, Y. Geffen, and J. J. Wlassich. Sensing and modeling of the hot isostatic pressing of copper pressing. Acta Metall. Mater. 1991;39:979-986.

[59] M. F. Ashby. Hip 6.0, background reading. Cambriage, UK: University of Cambridge; 1990.

[60] E. Olevsky, H. J. Dudek, and W. A. Kaysser. Hiping conditions for processing of metal matrix composites using the continuum theory for sintering-I. Theoretical analysis. Acta Mater. 1996;44:707-713.

[61] J. M. Duva, and P. D. Crow. The densification of powders by power-law creep during hot isostatic pressing. Acta Metall. Mater. 1992;40:31-35.

[62] J. Besson, and M. Abouaf. Rheology of porous alumina and simulation of hot isostatic pressing. J. Am. Ceram. Soc. 1992;75:2165-2172.

[63] Z. Y. Fu, H. Wang, W. M. Wang, and R. Z. Yuan. Composites fabricated by self-propagating high-temperature synthesis. J. Mater. Process. Technol. 2003;137:30-34.

[64] J. C. LaSalvia, D. K. Kim, and M. A. Meyers. Effect of mo on microstructure and mechanical properties of TiC-Ni-based cermets produced by combustion synthesis-impact forging technique. Mater. Sci. Eng. A. 1996;206:71-80.

[65] E. R. Strutt, E. A. Olevsky, and M. A. Meyers. Combustion synthesis/quasi-isostatic pressing of tic–niti cermets: Processing and mechanical response. J. Mater. Sci. 2008;43:6513-6526.

[66] C.-Y. Huang, and G. S. Daehn. Densification of composite powder compacts in pressure cycling. Acta Mater. 1996;44:1035-1045.

[67] C.-Y. Huang, and G. S. Daehn. Effect of cyclic pressure on the low temperature consolidation of several composite powder systems. Acta Mater. 1997;45:4283-4296.

[68] Y. Fu, G. Jiang, J. J. Lannutti, R. H. Wagoner, and G. S. Daehn. Effect of cyclic pressure consolidation on the uniformity of metal matrix composites. Metall. Mater. Trans. A. 2002;33:183-191.

[69] A. Zavaliangos, and A. Laptev. The densification of powder mixtures containing soft and hard components under static and cyclic pressure. Acta Mater. 2000;48:2565-2570.

[70] G. Jiang, W. Wu, G. S. Daehn, and R. H. Wagoner. Experimental and numerical investigation of idealized consolidation: Part II: Cyclic compaction. Acta Mater. 2000;48:4331-4335.

[71] G. R. Shaik, and W. W. Milligan. Consolidation of nanostructured metal powders by rapid forging: Processing, modeling, and subsequent mechanical behavior. Metall. Mater. Trans. A. 1997;28:895-904.

[72] G. D. Zhan, J. E. Garay, and A. K. Mukherjee. Ultralow-temperature superplasticity in nanoceramic composites. Nano Lett. 2005;5:2593-2597.

[73] R. Chaim, and Z. Shen. Grain size control by pressure application regime during spark plasma sintering of Nd-YAG nanopowders. J. Mater. Sci. 2008;43:5023-5027.

[74] E. Olevsky, I. Bogachev, and A. Maximenko. Spark-plasma sintering efficiency control by inter-particle contact area growth: A viewpoint. Scr. Mater. 2013;69:112-116.

[75] L. An, A. Ito, and T. Goto. Two-step pressure sintering of transparent lutetium oxide by spark plasma sintering. J. Eur. Ceram. Soc. 2011;31:1597-1602.

[76] W. Li, E. A. Olevsky, J. McKittrick, A. L. Maximenko, and R. M. German. Densification mechanisms of spark plasma sintering: Multi-step pressure dilatometry. J. Mater. Sci. 2012;47:7036-7046.

[77] W. G. Fahrenholtz, E. J. Wuchina, W. E. Lee, and Y. Zhou. Introduction. Ultra-high temperature ceramics: John Wiley & Sons, Inc; 2014. p. 1-5.

[78] A. L. Chamberlain, W. G. Fahrenholtz, and G. E. Hilmas. Pressureless sintering of zirconium diboride. J. Am. Ceram. Soc. 2006;89:450-456.

[79] W. G. Fahrenholtz, G. E. Hilmas, S. C. Zhang, and S. Zhu. Pressureless sintering of zirconium diboride: Particle size and additive effects. J. Am. Ceram. Soc. 2008;91:1398-1404.

[80] X. Zhang, G. E. Hilmas, W. G. Fahrenholtz, and D. M. Deason. Hot pressing of tantalum carbide with and without sintering additives. J. Am. Ceram. Soc. 2007;90:393-401.

[81] W. A. Sanders, and S. J. Grisaffe. The hot-pressing of hafnium carbide (melting point, 7030 °F). Nonmetallic Materials. Cleveland, OH: NASA Lewis Research Center; 1960. p. 1-16.

[82] Z. Guo-Jun, G. Wei-Ming, N. De-Wei, and K. Yan-Mei. Ultrahigh temperature ceramics (uhtcs) based on ZrB_2 and HfB_2 systems: Powder synthesis, densification and mechanical properties. J. Phys. Conf. Ser. 2009;176:012041.

[83] M. Gasch, D. Ellerby, E. Irby, S. Beckman, M. Gusman, and S. Johnson. Processing, properties and arc jet oxidation of hafnium diboride/silicon carbide ultra high temperature ceramics. J. Mater. Sci. 2004;39:5925-5937.

[84] A. Bellosi, S. Guicciardi, V. Medri, F. Monteverde, D. Sciti, and L. Silvestroni. Processing and properties of ultra-refractory composites based on Zr- and Hf-borides: State of the art and perspectives. In: N. Orlovskaya and M. Lugovy, editors. Boron rich solids: Springer Netherlands; 2011. p. 147-160.

[85] D. Lahiri, V. Singh, G. R. Rodrigues, T. M. H. Costa, M. R. Gallas, S. R. Bakshi, S. Seal, and A. Agarwal. Ultrahigh-pressure consolidation and deformation of tantalum carbide at ambient and high temperatures. Acta Mater. 2013;61:4001-4009.

[86] J. Besson, F. Valin, P. Lointier, and M. Boncoeur. Densification of titanium diboride by hot isostatic pressing and production of near-net-shape components. J. Mater. Eng. Perform. 1992;1:637-649.

[87] B. C. Schulz. Processing and characterization of tantalum-hafnium carbides. Tuscaloosa, Alabama: The university of Alabama; 2011.

[88] A. L. Chamberlain, W. G. Fahrenholtz, and G. E. Hilmas. Reactive hot pressing of zirconium diboride. J. Eur. Ceram. Soc. 2009;29:3401-3408.

[89] M. Ziemnicka-Sylwester. TiB_2-based composites for ultra-high-temperature devices, fabricated by SHS, combining strong and weak exothermic reactions. Materials. 2013;6:1903-1919.

[90] B.-R. Kim, K.-D. Woo, J.-M. Doh, J.-K. Yoon, and I.-J. Shon. Mechanical properties and rapid consolidation of binderless nanostructured tantalum carbide. Ceram. Int. 2009;35:3395-3400.

[91] Z. A. Munir, D. V. Quach, and M. Ohyanagi. Electric current activation of sintering: A review of the pulsed electric current sintering process. J. Am. Ceram. Soc. 2011;94:1-19.

[92] O. Guillon, J. Gonzalez-Julian, B. Dargatz, T. Kessel, G. Schierning, J. Räthel, and M. Herrmann. Field-assisted sintering technology/spark plasma sintering: Mechanisms, materials, and technology developments. Adv. Eng. Mater. 2014;16:830-849.

[93] A. Bellosi, F. Monteverde, and D. Sciti. Fast densification of ultra-high-temperature ceramics by spark plasma sintering. Int. J. Appl. Ceram. Tec. 2006;3:32-40.

[94] T. Mizuguchi, S. Guo, and Y. Kagawa. Transmission electron microscopy characterization of spark plasma sintered ZrB_2 ceramic. Ceram. Int. 2010;36:943-946.

[95] M. Thompson, W. G. Fahrenholtz, and G. Hilmas. Effect of starting particle size and oxygen content on densification of ZrB_2. J. Am. Ceram. Soc. 2011;94:429-435.

[96] E. Khaleghi, Y. S. Lin, M. A. Meyers, and E. A. Olevsky. Spark plasma sintering of tantalum carbide. Scr. Mater. 2010;63:577-580.

[97] H. J. Ryu, Y. W. Lee, S. I. Cha, and S. H. Hong. Sintering behaviour and microstructures of carbides and nitrides for the inert matrix fuel by spark plasma sintering. J. Nucl. Mater. 2006;352:341-348.

[98] G. Vasudevamurthy, T. W. Knight, E. Roberts, and T. M. Adams. Laboratory production of zirconium carbide compacts for use in inert matrix fuels. J. Nucl. Mater. 2008;374:241-247.

[99] Y. Katoh, G. Vasudevamurthy, T. Nozawa, and L. L. Snead. Properties of zirconium carbide for nuclear fuel applications. J. Nucl. Mater. 2013;441:718-742.

[100] V. P. Bulychev, R. A. Andrievskii, and L. B. Nezhevenko. The sintering of zirconium carbide. Sov. Powder Metall. Met. Ceram. 1977;16:273-276.

[101] L. Zhao, D. Jia, X. Duan, Z. Yang, and Y. Zhou. Pressureless sintering of ZrC-based ceramics by enhancing powder sinterability. Int. J. Refract. Met. Hard Mater. 2011;29:516-521.

[102] I. I. Spivak, and V. V. Klimenko. Densification kinetics in the hot pressing and recrystallization of carbides. Sov. Powder Metall. Met. Ceram. 1973;12:883-887.

[103] P. Barnier, C. Brodhag, and F. Thevenot. Hot-pressing kinetics of zirconium carbide. J. Mater. Sci. 1986;21:2547-2552.

[104] E. Minhaga, and W. D. Scott. Sintering and mechanical-properties of ZrC-ZrO_2 composites. J. Mater. Sci. 1988;23:2865-2870.

[105] X.-G. Wang, W.-M. Guo, Y.-M. Kan, G.-J. Zhang, and P.-L. Wang. Densification behavior and properties of hot-pressed ZrC ceramics with Zr and graphite additives. J. Eur. Ceram. Soc. 2011;31:1103-1111.

[106] C. Nachiappan, L. Rangaraj, C. Divakar, and V. Jayaram. Synthesis and densification of monolithic zirconium carbide by reactive hot pressing. J. Am. Ceram. Soc. 2010;93:1341-1346.

[107] R. Orru, R. Licheri, A. M. Locci, A. Cincotti, and G. C. Cao. Consolidation/synthesis of materials by electric current activated/assisted sintering. Mater. Sci. Eng. R. 2009;63:127-287.

[108] J. E. Garay. Current-activated, pressure-assisted densification of materials. Ann. Rev. Mater. Res. 2010;40:445-468.

[109] D. Sciti, S. Guicciardi, and M. Nygren. Spark plasma sintering and mechanical behaviour of ZrC-based composites. Scr. Mater. 2008;59:638-641.

[110] M. Gendre, A. Ma ître, and G. Trolliard. A study of the densification mechanisms during spark plasma sintering of zirconium (oxy-)carbide powders. Acta Mater. 2010;58:2598-2609.

[111] M. Gendre, A. Ma ître, and G. Trolliard. Synthesis of zirconium oxycarbide (ZrC_xO_y) powders: Influence of stoichiometry on densification kinetics during spark

plasma sintering and on mechanical properties. J. Eur. Ceram. Soc. 2011;31:2377-2385.

[112] B. Núñez-González, A. L. Ortiz, F. Guiberteau, M. Nygren, and L. Shaw. Improvement of the spark-plasma-sintering kinetics of zrc by high-energy ball-milling. J. Am. Ceram. Soc. 2012;95:453-456.

[113] J. Xie, Z. Fu, Y. Wang, S. W. Lee, and K. Niihara. Synthesis of nanosized zirconium carbide powders by a combinational method of sol–gel and pulse current heating. J. Eur. Ceram. Soc. 2014;34:13.e11-13.e17.

[114] R. Chaim. Densification mechanisms in spark plasma sintering of nanocrystalline ceramics. Mater. Sci. Eng. A. 2007;443:25-32.

[115] E. Olevsky, and L. Froyen. Constitutive modeling of spark-plasma sintering of conductive materials. Scr. Mater. 2006;55:1175-1178.

[116] E. Olevsky, S. Kandukuri, and L. Froyen. Analysis of mechanisms of spark-plasma sintering. Key Eng. Mater. 2008;368-372:1580-1584.

[117] E. A. Olevsky, S. Kandukuri, and L. Froyen. Consolidation enhancement in spark-plasma sintering: Impact of high heating rates. J. Appl. Phys. 2007;102:114913.

[118] E. A. Olevsky, and L. Froyen. Impact of thermal diffusion on densification during SPS. J. Am. Ceram. Soc. 2009;92:S122-S132.

[119] D. Giuntini, X. Wei, A. L. Maximenko, L. Wei, A. M. Ilyina, and E. A. Olevsky. Initial stage of free pressureless spark-plasma sintering of vanadium carbide: Determination of surface diffusion parameters. Int. J. Refract. Met. Hard Mater. 2013;41:501-506.

[120] M. Tokita. Industrial applications forfunctionally graded materials fabricated by spark plasmasintering (SPS) systems. Korus 2000: 4th Korea-Russia International Symposium on Science and Technology, Pt 3, Proceedings. 2000:251-256.

[121] M. Tokita. Industrial applications of advanced spark plasma sintering. Am. Ceram. Soc. Bull. 2006;85:32-34.

[122] E. Olevsky, E. Khaleghi, C. Garcia-Cardona, and W. L. Bradbury. Fundamentals of spark-plasma sintering: Applications to net-shaping of high strength temperature resistant components. Mater. Sci. Forum. 2010;654-656:412-415.

[123] G. Antou, G. Mathieu, G. Trolliard, and A. Maître. Spark plasma sintering of zirconium carbide and oxycarbide: Finite element modeling of current density, temperature, and stress distributions. J. Mater. Res. 2009;24:404-412.

[124] X. Wei, C. Back, O. Izhvanov, O. Khasanov, C. Haines, and E. Olevsky. Spark plasma sintering of commercial zirconium carbide powders: Densification behavior and mechanical properties. Materials. 2015;8:6043-6061.

[125] E. A. Olevsky. Theory of sintering: From discrete to continuum. Mater. Sci. Eng. R. 1998;23:41-100.

[126] L. N. Grossman. High-temperature thermophysical properties of zirconium carbide. J. Am. Ceram. Soc. 1965;48:236-&.

[127] U. Anselmi-Tamburini, J. E. Garay, and Z. A. Munir. Fast low-temperature consolidation of bulk nanometric ceramic materials. Scr. Mater. 2006;54:823-828.

[128] D. Giuntini, E. A. Olevsky, C. Garcia-Cardona, A. L. Maximenko, M. S. Yurlova, C. D. Haines, D. G. Martin, and D. Kapoor. Localized overheating phenomena and optimization of spark-plasma sintering tooling design. Materials. 2013;6:2612-2632.

[129] X. Wei, D. Giuntini, A. L. Maximenko, C. D. Haines, and E. A. Olevsky. Experimental investigation of electric contact resistance in spark plasma sintering tooling setup. J. Am. Ceram. Soc. 2015;98:3553-3560.

[130] J. P. Kelly, and O. A. Graeve. Mechanisms of pore formation in high-temperature carbides: Case study of tac prepared by spark plasma sintering. Acta Mater. 2015;84:472-483.

[131] I. W. Chen, and X. H. Wang. Sintering dense nanocrystalline ceramics without final-stage grain growth. Nature. 2000;404:168-171.

[132] S. Timoshenko, and S. Woinowsky-Krieger. Theory of plates and shells. 2 ed. New York: Mcgraw-Hill Book Company; 1959.

[133] W. Li, E. A. Olevsky, O. L. Khasanov, C. A. Back, O. Izhvanov, J. Opperman, and H. E. Khalifa. Spark plasma sintering of agglomerated vanadium carbide powder. Ceram. Int. 2015;41:3748-3759.

[134] M. Y. Balshin. Relation of mechanical properties of powder metals and their porosity and the ultimate properties of porous-metal ceramic materials. Dokl. Akad. Nauk SSSR+. 1949;67:831-834.

[135] C. Musa, R. Licheri, R. Orrù, G. Cao, D. Sciti, L. Silvestroni, L. Zoli, A. Balbo, L. Mercatelli, M. Meucci, and E. Sani. Processing, mechanical and optical properties of additive-free ZrC ceramics prepared by spark plasma sintering. Materials. 2016;9:489.

[136] S. Libardi, M. Zadra, F. Casari, and A. Molinari. Mechanical properties of nanostructured and ultrafine-grained iron alloys produced by spark plasma sintering of ball milled powders. Mater. Sci. Eng. A. 2008;478:243-250.

[137] J. Luo, and R. Stevens. Porosity-dependence of elastic moduli and hardness of 3Y-TZP ceramics. Ceram. Int. 1999;25:281-286.

[138] Y. V. Milman, S. I. Chugunova, I. V. Goncharova, T. Chudoba, W. Lojkowski, and W. Gooch. Temperature dependence of hardness in silicon-carbide ceramics with different porosity. Int. J. Refract. Met. Hard Mater. 1999;17:361-368.

[139] W. J. Parker, R. J. Jenkins, C. P. Butler, and G. L. Abbott. Flash method of determining thermal diffusivity, heat capacity, and thermal conductivity. J. Appl. Phys. 1961;32:1679-1684.

[140] E. K. Storms. The refractory carbides. New York: Academic Press; 1967.

[141] A. G. Turchanin, E. A. Guseva, and V. V. Fesenko. Thermodynamic properties of refractory carbides in the temperature range 0–3000 °K. Sov. Powder Metall. Met. Ceram. 1973;12:215-217.

[142] R. E. Taylor. Thermal conductivity of zirconium carbide at high temperatures. J. Am. Ceram. Soc. 1962;45:353-354.

[143] K. R. Anderson, J. R. Groza, M. Fendorf, and C. J. Echer. Surface oxide debonding in field assisted powder sintering. Mater. Sci. Eng. A. 1999;270:278-282.

[144] Mukherje.Ak, J. E. Bird, and J. E. Dorn. Experimental correlations for high-temperature creep. ASM Trans. Q. 1969;62:155-179.

[145] F. R. N. Nabarro. Do we have an acceptable model of power-law creep? Mater. Sci. Eng. A. 2004;387-389:659-664.

[146] R. C. Gifkins. Grain-boundary sliding and its accommodation during creep and superplasticity. Metall. Trans. A. 1976;7:1225-1232.

[147] J. Weertman. Steady-state creep of crystals. J. Appl. Phys. 1957;28:1185-1189.

[148] J. Weertman. Theory of steady-state creep based on dislocation climb. J. Appl. Phys. 1955;26:1213-1217.

[149] J. Weertman. Steady-state creep through dislocation climb. J. Appl. Phys. 1957;28:362-364.

[150] V. Skorohod. Rheological basis of the theory of sintering. Kiev: Naukova Dumka; 1972.

[151] E. A. Olevsky, C. Garcia-Cardona, W. L. Bradbury, C. D. Haines, D. G. Martin, D. Kapoor, and S. J. Kang. Fundamental aspects of spark plasma sintering: Ii. Finite element analysis of scalability. J. Am. Ceram. Soc. 2012;95:2414-2422.

[152] E. Olevsky, and R. Rein. Kinetics of sintering for powder systems with bimodal pore-size distribution. High Temp-high. Press. 1995;27/28:81-90.

[153] X. Wei, C. Back, O. Izhvanov, C. Haines, and E. Olevsky. Zirconium carbide produced by spark plasma sintering and hot pressing: Densification kinetics, grain growth, and thermal properties. Materials. 2016;9:577.

[154] E. A. Olevsky, W. L. Bradbury, C. D. Haines, D. G. Martin, D. Kapoor, and S. J. Kang. Fundamental aspects of spark plasma sintering: I. Experimental analysis of scalability. J. Am. Ceram. Soc. 2012;95:2406-2413.

[155] A. Zavaliangos, J. Zhang, M. Krammer, and J. R. Groza. Temperature evolution during field activated sintering. Mater. Sci. Eng. A. 2004;379:218-228.

[156] C. Wang, L. F. Cheng, and Z. Zhao. Fem analysis of the temperature and stress distribution in spark plasma sintering: Modelling and experimental validation. Comp. Mater. Sci. 2010;49:351-362.

[157] U. Anselmi-Tamburini, S. Gennari, J. E. Garay, and Z. A. Munir. Fundamental investigations on the spark plasma sintering/synthesis process. Mater. Sci. Eng. A. 2005;394:139-148.

[158] G. Maizza, S. Grasso, Y. Sakka, T. Noda, and O. Ohashi. Relation between microstructure, properties and spark plasma sintering (SPS) parameters of pure ultrafine wc powder. Sci.Technol. Adv. Mat. 2007;8:644-654.

[159] G. Maizza, S. Grasso, and Y. Sakka. Moving finite-element mesh model for aiding spark plasma sintering in current control mode of pure ultrafine wc powder. J. Mater. Sci. 2009;44:1219-1236.

[160] S. Grasso, Y. Sakka, G. Maizza, and C. F. Hu. Pressure effect on the homogeneity of spark plasma-sintered tungsten carbide powder. J. Am. Ceram. Soc. 2009;92:2418-2421.

[161] S. Grasso, Y. Sakka, and G. Maizza. Pressure effects on temperature distribution during spark plasma sintering with graphite sample. Mater. Trans. 2009;50:2111-2114.

[162] S. Grasso, Y. Sakka, and G. Maizza. Effects of initial punch-die clearance in spark plasma sintering process. Mater. Trans. 2008;49:2899-2906.

[163] K. Vanmeensel, A. Laptev, J. Hennicke, J. Vleugels, and O. Van der Biest. Modelling of the temperature distribution during field assisted sintering. Acta Mater. 2005;53:4379-4388.

[164] A. Cincotti, A. M. Locci, R. Orrù, and G. Cao. Modeling of SPS apparatus: Temperature, current and strain distribution with no powders. Aiche J. 2007;53:703-719.

[165] D. Liu, Y. Xiong, Y. Li, T. Topping, Y. Zhou, C. Haines, J. Paras, D. Martin, D. Kapoor, J. Schoenung, and E. Lavernia. Spark plasma sintering of nanostructured aluminum: Influence of tooling material on microstructure. Metall. Mater. Trans. A. 2013;44:1908-1916.

[166] O. M. Akselsen. Diffusion bonding of ceramics. J. Mater. Sci. 1992;27:569-579.

[167] B. T. Kelly, and P. L. Walker Jr. Theory of thermal expansion of a graphite crystal in the semi-continuum model. Carbon. 1970;8:211-226.

[168] M. M. Yovanovich. Four decades of research on thermal contact, gap, and joint resistance in microelectronics. IEEE. T. Compon. Pack. Technol. 2005;28:182-206.

[169] D. Giuntini, J. Raethel, M. Herrmann, A. Michaelis, and E. A. Olevsky. Advancement of tooling for spark plasma sintering. J. Am. Ceram. Soc. 2015;98:3529-3537.

[170] H. Djohari, J. I. Martínez-Herrera, and J. J. Derby. Transport mechanisms and densification during sintering: I. Viscous flow versus vacancy diffusion. Chem. Eng. Sci. 2009;64:3799-3809.

[171] R. A. Andrievskii, Y. F. Khromov, and I. S. Alekseeva. Self-diffusion of carbon and metal atoms in zirconium and niobium carbides. Fiz. Metal. Metalloved. 1971;32:664-667.

[172] S. Sarian, and J. M. Criscione. Diffusion of carbon through zirconium monocarbide. J. Appl. Phys. 1967;38:1794-1798.

[173] J. G. Noudem, D. Kenfaui, D. Chateigner, and M. Gomina. Toward the enhancement of thermoelectric properties of lamellar $Ca_3Co_4O_9$ by edge-free spark plasma texturing. Scr. Mater. 2012;66:258-260.

[174] S. D. Bhame, D. Pravarthana, W. Prellier, and J. G. Noudem. Enhanced thermoelectric performance in spark plasma textured bulk n-type $BiTe_{2.7}Se_{0.3}$ and p-type $Bi_{0.5}Sb_{1.5}Te_3$. Appl. Phys. Lett. 2013;102:211901.

[175] Q. Lognone, F. Gascoin, O. I. Lebedev, L. Lutterotti, S. Gascoin, and D. Chateigner. Quantitative texture analysis of spark plasma textured n-Bi_2Te_3. J. Am. Ceram. Soc. 2014;97:2038-2045.

[176] E. V. Aleksandrova, A. M. Ilyina, E. G. Grigoryev, and E. A. Olevsky. Contribution of electric current into densification kinetics during spark plasma sintering of conductive powder. J. Am. Ceram. Soc. 2015;98:3509-3517.

[177] J. B. Allen, and C. Walter. Numerical simulation of the temperature and stress field evolution applied to the field assisted sintering technique. ISRN Mater. Sci. 2012;2012:9.

[178] J. H. Lee, J. Y. Ju, C. H. Kim, J. H. Park, H. S. Lee, and Y. D. Shin. The development of an electroconductive SiC-ZrB_2 composite through spark plasma sintering under argon atmosphere. J. Electr. Eng. Technol. 2010;5:342-351.

[179] M. W. Bird, R. P. Aune, A. F. Thomas, P. F. Becher, and K. W. White. Temperature-dependent mechanical and long crack behavior of zirconium diboride-silicon carbide composite. J. Eur. Ceram. Soc. 2012;32:3453-3462.

[180] J. W. Zimmermann, G. E. Hilmas, W. G. Fahrenholtz, R. B. Dinwiddie, W. D. Porter, and H. Wang. Thermophysical properties of ZrB_2 and ZrB_2-SiC ceramics. J. Am. Ceram. Soc. 2008;91:1405-1411.

[181] E. A. Olevsky, S. M. Rolfing, and A. L. Maximenko. Flash (ultra-rapid) spark-plasma sintering of silicon carbide. Sci. Rep. 2016;6:33408.

[182] C. P. Kempter, and R. J. Fries. Crystallographic data. 189. Zirconium carbide. Anal. Chem. 1960;32:570-570.

[183] B. R. T. Frost. The carbides of uranium. J. Nucl. Mater. 1963;10:265-300.

[184] D. R. Olander. Fundamental aspects of nuclear reactor fuel elements: Technical Information Center, Office of Public Affairs, Energy Research and Development Administration; 1976.

[185] L. C. Bernard, and E. Bonnaud. Finite volume method for fission gas release modeling. J. Nucl. Mater. 1997;244:75-84.

[186] L. Grande, B. Villamere, L. Allison, S. Mikhael, A. Rodriguez-Prado, and I. Pioro. Thermal aspects of uranium carbide and uranium dicarbide fuels in supercritical water-cooled nuclear reactors. J. Eng. Gas. Turb. Power. 2011;133.

[187] Q. M. Wang, Y. Cui, Y. Z. Huo, and S. R. Ding. Simulation of the coupling behaviors of particle and matrix irradiation swelling and cladding irradiation growth of plate-type dispersion nuclear fuel elements. Mech. Mater. 2011;43:222-241.

[188] W. E. Lee, M. Gilbert, S. T. Murphy, and R. W. Grimes. Opportunities for advanced ceramics and composites in the nuclear sector. J. Am. Ceram. Soc. 2013;96:2005-2030.

[189] W. N. Findley, J. S. Lai, and K. Onaran. Creep and relaxation of nonlinear viscoelastic materials: With an introduction to linear viscoelasticity: Courier Dover Publications; 1976.

[190] E. Olevsky, V. Skorohod, and G. Petzow. Densification by sintering incorporating phase transformations. Scr. Mater. 1997;37:635-643.

[191] G. Cui, X. Wei, E. A. Olevsky, R. M. German, and J. Chen. Preparation of high performance bulk Fe–N alloy by spark plasma sintering. Mater. Design. 2016;90:115-121.

[192] M. Suzuki, H. Uetsuka, and H. Saitou. Analysis of mechanical load on cladding induced by fuel swelling during power ramp in high burn-up rod by fuel performance code FEMAXI-6. Nucl. Eng. Des. 2004;229:1-14.

[193] D. R. Olander. Nuclear fuels - present and future. J. Nucl. Mater. 2009;389:1-22.

[194] D. L. Y. Louie. Characterization of fuel swelling in helium-bonded carbide fuel pins. Albuquerque, New Mexico: University of New Mexico; 1987.

[195] J. W. Harrison. The irradiation-induced swelling of uranium carbide. J. Nucl. Mater. 1969;30:319-323.

[196] J. O. Bloeneke, and M. F. Todd. Uranium-235 fission-product production as a function of thermal neutron flux, irradiation time, and decay time. [part] I., Atomic concentrations and gross totals. Oak Ridge, TN: Oak Ridge National Laboratory; 1957.

[197] P. Prajoto, A. R. Wazzan, and D. Okrent. Computer modeling of steady-state fission-gas behavior in carbide fuels. Nucl. Eng. Des. 1978;48:461-495.

[198] R. S. Nelson. The stability of gas bubbles in an irradiation environment. J. Nucl. Mater. 1969;31:153-161.

[199] J. R. Matthews, and M. H. Wood. Efficient method for calculating diffusive flow to a spherical boundary. Nucl. Eng. Des. 1980;56:439-443.

[200] R. L. Ritzman, A. J. Markworth, W. Oldfield, and W. Chubb. Interpretations of fission gas behavior in refractory fuels. Nucl. Appl. Tech. 1970;9:167-187.

[201] A. R. Wazzan, J. Tatsumi, and D. Okrent. Effect of non-equilibrium fission-gas and fuel creep on swelling and release in irradiated carbide fuels. Nucl. Eng. Des. 1985;88:93-101.

[202] A. Padel, and C. De Novion. Constantes elastiques des carbures, nitrures et oxydes d'uranium et de plutonium. J. Nucl. Mater. 1969;33:40-51.

[203] A. R. Hall. Elastic moduli and internal friction of some uranium ceramics. J. Nucl. Mater. 1970;37:314-323.

[204] R. J. White, and M. O. Tucker. A new fission-gas release model. J. Nucl. Mater. 1983;118:1-38.

[205] H. D. Lewis, and J. F. Kerrisk. Electrical and thermal transport properties of uranium and plutonium carbides: A review of literature. Los Alamos, NM: Los Alamos Scientific Laboratory; 1975.

[206] R. C. Progelhof, J. L. Throne, and R. R. Ruetsch. Methods for predicting the thermal conductivity of composite systems: A review. Polym. Eng. Sci. 1976;16:615-625.